Title

Recording Coastal Changes observed in Beach Ridges and Prograded Beach Stratigraphy using Ground-Penetrating Radar

Author

Zurbuchen, Julie Marie

Publication Date

2019

UNIVERSITY OF CALIFORNIA

Santa Barbara

Recording Coastal Changes observed in Beach Ridges and Prograded Beach Stratigraphy using Ground-Penetrating Radar

A dissertation submitted in partial satisfaction of the
requirements for the degree Doctor of Philosophy
in Earth Science

by

Julie Marie Zurbuchen

Committee in charge:

Professor Alexander R. Simms, Chair

Professor Lorraine Lisiecki

Professor Vamsi Ganti

September 2019

The dissertation of Julie Marie Zurbuchen is approved.

Lorraine Lisiecki

Vamsi Ganti

Alexander R. Simms, Committee Chair

August 2019

ACKNOWLEDGEMENTS

While the following chapters contain my scientific contributions to the field of sedimentary geology, they cannot begin to describe all the valuable knowledge I have gained while in graduate school. I have to begin by thanking my advisor, Dr. Alexander Simms, for the countless hours he has spent teaching, discussing, and reviewing my papers; all helping me to become a better researcher and scientist. Without his guidance and his reviews, these chapters would not have come together.

I would also like to thank Lorraine Lisiecki and Vamsi Ganti for serving as members on my committee. I appreciate the discussions on statistics and research directions, and continue to think about the statistical significance of results in research and how they can be interpreted (and misinterpreted).

I am incredibly thankful for my lab mates, Laura Reynolds, Elisabeth Steel, Zack Nelson, and Michael Benz for their help with data collection along the beaches in California, Washington, and especially Antarctica. I would also like to thank my fellow graduate students and friends whose support and advice have helped me grow as a scientist and person. I am grateful for the casual office discussions, roof lunches, and mesa days.

Lastly, I would like to thank my family for all the emotional support they have provided me. To my parents, Bruce and Jeri, and my sisters, Kendall and Mary, thank you for listening to me on the phone, and building me up when I needed it most, in grad school and in life. You have helped prepare me for the career I am excited to embark on. To Julian, thank you for being by my side for the past four years of graduate school, and listening to the same presentation 10x over. To all the above, thank you for your constant support and encouragement, I truly could not have done this without you.

VITA OF JULIE MARIE ZURBUCHEN

September 2019

EDUCATION

Bachelor of Science in Geophysics (high honors), University of Texas at Austin, May 2014
Doctor of Philosophy in Earth Science, University of California, Santa Barbara, September 2019 (expected)

PROFESSIONAL EMPLOYMENT

2011-2012: Basin Modeling and Geochemistry Intern, ConocoPhillips, Houston, TX
2012-2014: Undergraduate Researcher, University of Texas Institute for Geophysics, Austin, TX
2014: Geophysical Intern, EOG Resources, Fort Worth, TX
2017: Teaching Assistant, Department of Earth Science, University of California, Santa Barbara
2018: Earth Science Intern: Chevron, Covington, LA

PUBLICATIONS

Zurbuchen, J. M., Gulick, S. P., Walton, M. A., and Goff, J. A., 2015, Imaging evidence for Hubbard Glacier advances and retreats since the last glacial maximum in Yakutat and Disenchantment Bays, Alaska: *Geochemistry, Geophysics, Geosystems*, v. 16, no. 6, p. 1962-1974.

Simms, A. R., DeWitt, R., **Zurbuchen, J**., and Vaughan, P., 2017, Coastal erosion and recovery from a Cascadia subduction zone earthquake and tsunami: *Marine Geology*, v. 392, p. 30-40.

Zurbuchen, J., Simms, A.R., Warrick, J.A., Miller, I.M., Ritchie, A., *in review*, A model for growth and development of small mountainous river wave-dominated deltas: Insights from the Elwha River delta, Washington.

Zurbuchen, J., Simms A.R., *in review*, Late Holocene ice mass changes recorded in a relative sea-level record from Joinville Island, Antarctica.

Zurbuchen, J., Simms A.R., Huot, S., *submitted*, Episodic Progradation of the coastal Oxnard Plain, southern California

AWARDS

National Science Foundation Graduate Research Fellowship (2016-2019)
Alumni Graduate Award for Research Excellence (2018)
PSAAPG Outstanding Student Award (2017)
AAPG Grants-in-Aid Marta S. Weeks Named Grant (2016)
GSA Graduate Student Research Grant (2016)
UC Regents Fellowship (2015-2016)

FIELDS OF STUDY

Major field: Sedimentology and Stratigraphy

Study of coastal morphology and delta growth with Professor Alexander Simms, Jon Warrick of the USGS, and Ian Miller of the Washington SeaGrant

Study of Holocene sea-level changes as derived from beach ridges with Professor Alexander Simms

ABSTRACT

Recording Coastal Changes observed in Beach Ridges and Prograded Beach Stratigraphy using Ground-Penetrating Radar

by

Julie Marie Zurbuchen

Beach ridges and other prograding beach deposits are important sedimentary archives of past floods, storms, and relative sea-level changes. Accurate interpretations of beach ridges requires an understanding of their formation and preservation through time. In the following studies, I use ground-penetrating radar to observe the stratigraphy of beach ridges and prograded beach deposits. Additionally, I employ the use of elevation surveys, aerial photographs, radiocarbon dating, and optically stimulated luminescence dating to understand the timing of events preserved in the sedimentary record.

In Chapter 2, I explore the formation of swash bars on the Elwha River delta after the removal of two dams on the fluvial system simulated a large sediment pulse to the system, similar to a flood or landslide. I find that mouth bars form most often after higher than average discharge events in the fluvial system, and swash bars form soon after due to wave reworking of the mouth-bar sediments. However, only 10 of 37 swash bars that formed were preserved at the time of my GPR survey, five years after dam removal. Additionally, the swash bars that did survive amalgamated with one another, forming a large barrier at the

delta front, indicating that in small mountainous river settings, beach ridges may be more indicative a large sediment pulse to the system, rather than a single flood.

In Chapter 3, I examine the ~600-year sedimentary record of the coastal Oxnard Plain. Progradation on the Oxnard Plain has been relatively constant on centennial (150- to 200-year) timescales, prograding at rates of 0.3 to 1.4 m a^{-1}. However, on shorter timescales, progradation is episodic, with greater progradation occurring after high discharge events along the Santa Clara River. Extended droughts remove up to 90 m of the beach, equivalent to ~5 to ~120 years of the sedimentary record. Additionally, I image beach cusps in shore parallel GPR profiles, which previously had not been recognized in GPR profiles.

Lastly, in Chapter 4 I use gravel beach ridges to reconstruct the relative sea-level (RSL) record on Joinville Island, Antarctica. I find that RSL has fallen ~5 m over the last ~3000 years, at variable rates throughout the late Holocene. I interpret that ice mass loss, similar to the scale of ice mass loss after the 2002 Larsen B Ice shelf collapse, and ice mass growth caused by glacial advance, both occurred in the Late Holocene and were recorded in my RSL reconstruction. Therefore, global- and continental-scale global isostatic adjustment models, which currently only account for ice changes on thousand-year timescales, are missing crucial centennial-timescales ice mass changes.

TABLE OF CONTENTS

LIST OF FIGURES

CHAPTER 1

1. Introduction

Beaches are not only a place for recreation, but also an important archive of the geologic past. Sediments stored within prograding and accreting coastal systems, such as beaches and marshes, provide valuable information on paleo-environments that help us interpret how past events, such as storms, floods, and earthquakes have affected the coast. In addition, modern coastal systems allow us to understand how the events are recorded and preserved in the sedimentary record. This understanding is important for modeling and predicting future changes to the coast as climate changes. Beach ridges, defined as relict, semi-parallel ridges that form most often on prograding coasts, are one important archive for studying past environmental conditions (Otvos, 2000).

The stratigraphy and morphology of beach ridges and prograded beach deposits are controlled by climate, tectonic, and sea-level changes as well as internal mechanisms. Studies have utilized ground-penetrating radar (GPR) to image the stratigraphy recorded in these deposits to understand beach progradation (Bristow and Pucillo, 2006; Buynevich and FitzGerald, 2001; Van Heteren et al., 1998), storm erosion histories (Bristow et al., 2000; Buynevich et al., 2007; Neal et al., 2002), tsunami erosion caused by large earthquakes (Simms et al., 2017), and reconstruct past relative sea levels (Costas et al., 2016; Rodriguez and Meyer, 2006; van Heteren et al., 2000; Watcham et al., 2011). Given the importance of beaches and beach ridges as sedimentary archives, it is pivotal that we understand the factors influencing their formation, stratigraphy, and preservation to accurately interpret the geologic record.

Beach ridges form via three main mechanisms: 1) the progradation of sandy beaches and building of berms by fair weather waves, 2) the build-up of gravels by storm waves, and 3) the welding of longshore bars (Tamura, 2012). The welding of longshore bars to form beach ridges is considered rare (Carter, 1986), but is nonetheless an important mechanism to explore. Offshore bars that weld to the shoreline and eventually become beach ridges, are often thought to form after single storm or flood events (Hine, 1979; Lindhorst et al., 2008; Rodriguez et al., 2000). However, in systems like river deltas where sediment can be added in pulses, such as after a landslide or flood following extended drought or fire, does each swash bar still represent a single flooding event in the fluvial system? In Chapter 2, I explore the formation and preservation of mouth and swash bars formed after more than ~8.2 million tonnes of sediment was released into the Elwha River fluvial system following the removal of two dams (Magirl et al., 2015).

As beaches prograde, they preserve both the accretion of sedimentary deposits, as well as erosional surfaces that form during periods of reduced sediment supply or high-energy wave events (Tamura, 2012). On coasts with a continuous sediment supply, this pattern of beach progradation is thought to record constant periods of beach progradation, with short periods of erosion that remove parts of the sedimentary record (Buynevich and FitzGerald, 2001). However, few studies of the patterns of beach progradation have looked at coasts subject to variable sediment supply caused by decadal climate cycles, such as the El Niño Southern Oscillation. In Chapter 3, I examine the sediments and stratigraphy recorded in the coastal Oxnard Plain to better understand how climate cycles affect sediment deposition and preservation.

Gravel beach ridges that form on isostatically uplifting coasts are commonly used to reconstruct relative sea-level (RSL) histories (Fretwell et al., 2010; Pedersen et al., 2011;

Simkins et al., 2013; Simms et al., 2012; Watcham et al., 2011). These beach ridges can be used to estimate changes in RSL because the changes in RSL are often larger than the variability in elevation of the beach ridges (Tamura, 2012). RSL curves are a key input for ice-sheet reconstructions used for glacial isostatic adjustment (GIA) models describing the solid earth response to the growth and decay of ice-sheets. Most continental-scale GIA models currently do not account for ice-mass changes that occur on 100-year timescales (Peltier et al., 2015). However, recent GPS studies have captured decadal-scale changes in uplift rates on the Antarctic Peninsula following the collapse of the Larsen B ice shelf (Nield et al., 2014; Thomas et al., 2011). Are these short timescale uplift events common to the Antarctic Peninsula throughout the late Pleistocene and Holocene, or only a product of ice-mass loss caused by recent warming? In Chapter 4, I reconstruct the past ~3000 years of RSL history in the northeastern Antarctic Peninsula using gravel beach ridges on Joinville Island. I explore if the changes in the rate of RSL fall can be explained by similar episodes of ice-mass balance changes as occurred after the Larsen B ice-shelf collapse in 2002, and what the implications are for future GIA models and ice sheet reconstructions.

The following chapters all explore how beach ridges and prograding beach deposits can be used to understand earth’s history. By better understanding the past, we can better prepare for the future.

CHAPTER 2

2. A model for the growth and development of small mountainous river wave-dominated deltas: Insights from the Elwha River delta, Washington

2.1 Introduction

Understanding modern delta morphology and stratigraphic architecture is important for accurately interpreting the sedimentary record, and enhancing scientific understanding of past depositional environments, facies heterogeneities, and reservoir quality (Bhattacharya and Giosan, 2003; Ainsworth et al., 2011). Wave-dominated deltas in particular are important reservoirs for hydrocarbons, with typically thick accumulations of well-sorted sand deposited as deltas prograde. One important aspect of their morphology and stratigraphy is the amalgamation of swash bars or spits onto their delta plain (Rodriguez et al., 2000; Giosan, 2007; Anthony, 2015; Preoteasa et al., 2016; Vespremeanu-Stroe et al., 2016). This amalgamation is one process by which their subaerial plains prograde and is a key diagnostic feature in distinguishing wave-dominated deltas from fluvial- and tidal-dominated deltas (Rodriguez et al., 2000; Bhattacharya and Giosan, 2003). Once amalgamated to the shoreline, these swash bars often form beach ridges and provide an intriguing potential for reconstructing past sediment pulses, such as large flooding events, within the evolution of the wave-dominated delta (Rodriguez et al., 2000; Fraticelli, 2006).

Both mouth bars and swash bars are important distinguishing components of the delta plain of wave-dominated deltas (Reading, 2009). While the formation and morphology of subaerial swash bars on modern wave-dominated deltas is well-documented in other studies (Rodriguez et al., 2000; Bhattacharya and Giosan, 2003; Fraticelli, 2006; Preoteasa et al., 2016; Vespremeanu-Stroe et al., 2016; Nooren et al., 2017); important questions remain as to their use as sedimentary archives, including their preservation potential in the rock record. Current models are skewed toward large, near-continental scale river systems such as the Danube (Preoteasa et al., 2016; Vespremeanu-Stroe et al., 2016), Brazos (Rodriguez et al., 2000), and São Francisco (Dominguez, 1996) with bars and beach ridges that stretch alongshore at the km scale. However, many active margins are riddled with small mountainous rivers (SMR) that develop wave-dominated deltas whose morphology and development may be occurring at much different temporal scales.

Wave-dominated deltas are composed of a prodelta, delta front, and delta plain (Reading, 2009). Depending on the depth of the receiving basin, the delta front and prodelta are the site of the most voluminous sediment deposition, with the Elwha River delta in NW Washington being no exception (Gelfenbaum et al., 2015; Ritchie et al., 2018). However, the delta plain provides the subaerial portion of the delta and some of the most diagnostic features for distinguishing wave-dominated deltas from fluvial- and tidal-dominated deltas (Bhattacharya and Giosan, 2003).

Mouth bars form on wave-dominated deltas as fluvial outflows undergo rapid deceleration and deposit sediments (Wright, 1977). These mouth bars are the site of the majority of the bedload deposition from the river mouth and have a large impact on the development of the tributary network within deltas (Edmonds and Slingerland, 2007). Mouth bars often form after high-magnitude river discharge events and are subsequently reworked by wave action (Rodriguez et al., 2000; Fielding et al., 2005; Barnard and Warrick, 2010; Anthony, 2015). In rivers with a single point source, crescentic mouth bars are formed (Fig. 1A; Wright, 1977). When preserved in the rock record, mouth bars tend to have basin-ward dipping strata, comprised of coarsening upward sands (Fielding et al., 2005; Ainsworth et al., 2016).

Another important component of the delta plains of wave-dominated deltas are swash bars. The shore parallel, elongate sand bodies are formed by wave uprush and isolate small lagoons on their landward side (Hine, 1979; Jackson, 1997). Within the common wave-dominated delta model proposed by Wright (1977), swash bars are largely found on top of the mouth bar (Fig. 1B). Several studies have explored the formation of swash bars in other prograding coastal settings, including spits, and clastic shorelines (Hayes and Boothroyd, 1969; Hine, 1979; Bristow et al., 2000; Lindhorst et al., 2008). In these settings, storms erode sediment from the shoreface and transport it to the nearshore, where fair weather waves rework the sediment into elongate swash bars (Hayes and Boothroyd, 1969; Lindhorst et al., 2008). The resulting internal geometry of the swash bars is shallowly landward-dipping strata caused by overwash processes and slipface migration (Hine, 1979; Lindhorst et al., 2008). Understanding of swash-bar development on wave-dominated deltas, with both fluvial and littoral processes playing an integral role in sediment delivery and distribution, remains limited.

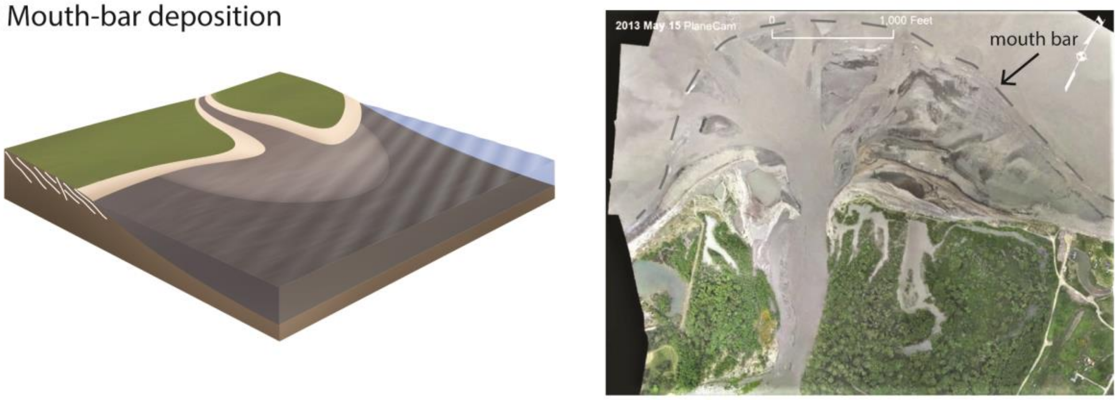

A) Mouth-bar deposition

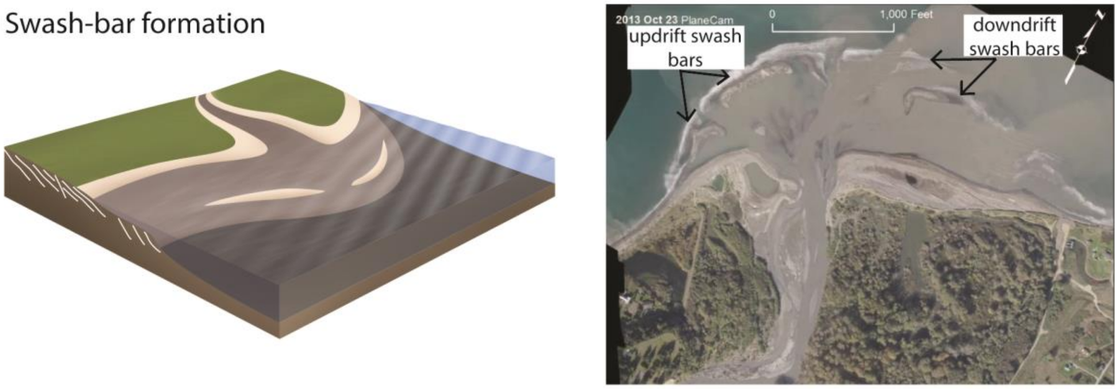

B) Swash-bar formation

Figure 1. A) Schematic of mouth-bar deposition, and aerial image showing how the authors distinguished a mouth-bar. B) Swash-bar schematic and aerial image showing how authors distinguished swash-bars. (Schematic drawing by Scott Condon, and photos by A. Ritchie)

The removal of two dams beginning in September 2011 along the Elwha River in NW Washington introduced ~8.2 million tonnes of sediment into the Elwha River over a two-year period (Warrick et al., 2015). This removal simulated a high-magnitude river discharge event and the large increase in sediment discharge resulted in a historically unprecedented progradation of the Elwha River's wave-dominated delta (Gelfenbaum et al., 2015; Magirl et al., 2015; Ritchie et al., 2018). This progradation provides a natural laboratory for recording the evolution and resulting stratigraphy of swash bars within a small asymmetric wave-dominated delta. The progradation of the Elwha River delta during dam removal is used to address four fundamental questions regarding the evolution of bars on wave-dominated deltas. 1) How is mouth-bar deposition related to river discharge in SMR settings? 2) What is the relationship between mouth-bar deposition and swash-bar formation? 3) What is the preservation potential of swash bars in these systems? And 4) What is the stratigraphic record of swash-bar amalgamation on a wave-dominated delta?

In order to answer these questions, a ground-penetrating radar (GPR) survey was conducted in July 2016 to capture the stratigraphy of sediment deposited after dam removal across the modern Elwha River delta. Additionally, elevation surveys collected monthly and repeated aerial photographs since 2011 captured the changing morphology of the delta and the welding of swash bars onto the delta plain.

2.2 Background and Regional Setting

2.2.1 Elwha River delta

The Elwha River flows north from the Olympic Mountains into the Strait of Juan de Fuca, west of Port Angeles, Washington (Fig. 2). The Olympic Mountains are an accretionary wedge formed by the convergence of the Juan de Fuca plate with the North American plate and includes assemblages of metasedimentary, sedimentary, and volcanic rocks. Glacial processes shaped the landscape and deposited till and outwash that reach tens of meters thick (Downing, 1983; Warrick et al., 2009). The Elwha River delta formed during a local highstand in sea level ~12,500 years ago, caused by the retreat of the Late Wisconsin glaciers across northern Washington State, leaving behind a depressed crust (Webster, 2014). Isostatic rebound of the glacially depressed crust caused a rapid fall in sea-level during which the delta prograded into the Strait of Juan de Fuca and subsequently was flooded as sea level in the region rose ~50 m from ~10,000 to 6,000 years before present (Downing, 1983; Mosher and Hewitt, 2004). The relict, subaqueous lowstand delta extends 2-5 km into the Strait and dips ~1° towards the slope break (Eidam et al., 2016).

The headwaters of the Elwha River reach an elevation of ~1400 m and the river drops to the ocean in ~70 km. Steep slopes in the watershed contribute to landslides, rockfalls, and debris flows, supplying sediment to the river (Montgomery and Brandon, 2002). The Elwha River watershed drains an area of 831 km^2 and has an average sediment yield of ~340,000 tonnes a^{-1} (Magirl et al., 2015). The mean annual discharge of the river is 42 m^3s^{-1} and the two-year recurrence interval flood is 400 $m^3\ s^{-1}$, with higher flow occurring during the fall-winter storms and the spring freshets (Duda et al., 2011; Eidam et al., 2016). Average significant wave heights at the Elwha River delta are ~0.4 m (Warrick et al., 2009). Waves are dominated by northwesterly swell originating in the Pacific Ocean, and winds drive waves from the west and northwest (Warrick et al., 2009). Tides near Port Angeles are mesotidal with a great diurnal tide range of 2.15 m (Warrick and Stevens, 2011).

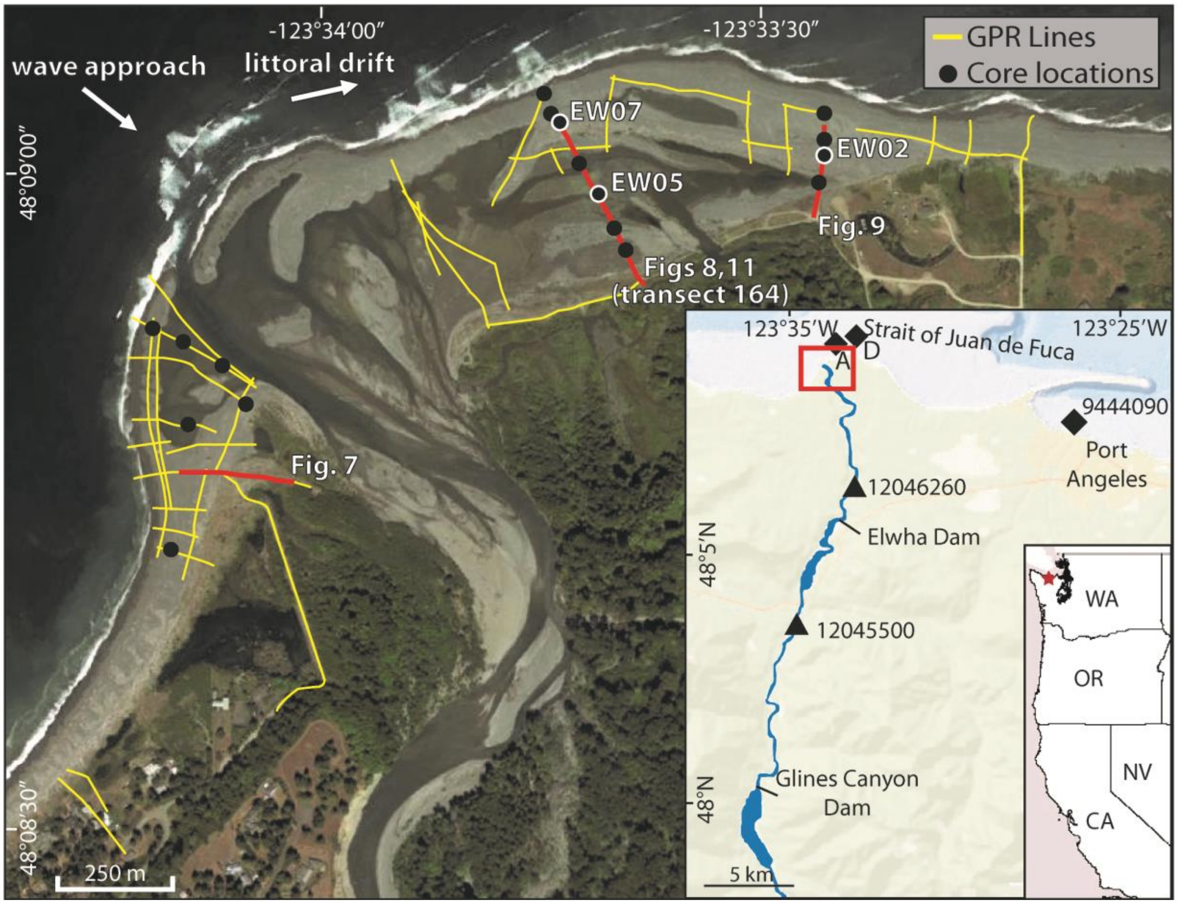

Figure 2. Satellite photograph of the Elwha River delta from July 2016 displaying locations of GPR transects as yellow lines and vibracore locations as black circles. Red GPR lines and white-outlined vibracores are discussed in the text. Image modified from Google Earth™. Inset map displays triangles at locations of USGS river gauges, diamonds at NOAA's National Data Buoy Center station PTAW1 and benthic tripods A and D, and locations of removed dams. The red box refers to the location of the study area in the main image.

2.2.2 Dam Removal

The Elwha Dam, completed in 1913 at river kilometer 8, and the Glines Canyon Dam, completed in 1927 at river kilometer 22, were built on the Elwha River to supply hydroelectric power to Port Angeles, WA. The dams captured the upper watershed supply of sands and gravels, and reduced bedload to the lower reaches of the Elwha River by ~90% starving the delta of sediment (Warrick et al., 2009). By 2010, the two dams had trapped ~21 million m^3 of sediment; about half of the sediment was clay and silt and the other half was sand, cobbles, and boulders (Randle et al., 2015). In 1992, the U.S. Congress passed a resolution to restore the Elwha River ecosystem and fisheries and the two dams were slated for removal as part of the largest dam decommissioning in the U.S. to date (Duda et al., 2011; Gelfenbaum et al., 2015). The phased removal process began on September 17th, 2011, with the Elwha Dam taking just over seven months to remove and the Glines Canyon Dam taking about three years. A full description of the dam removal process is found in Randle et al. (2015).

In the two years following the initiation of dam removal, ~8.2 million tonnes of sediment, or 5.9 million m^3, assuming an average bulk density of 1.4 tonnes m^{-3}, was released from the reservoirs behind the dams (Gelfenbaum et al., 2015; Magirl et al., 2015). An estimated ~6.3 million tonnes of this was suspended sediment load consisting of clay, silt, and sand (Magirl et al., 2015). Though most of the fine-grained sediment escaped into the Strait of Juan de Fuca, the majority of coarse-grained sediment (sand and gravel) was captured at the delta mouth and extended the active delta by nearly 200 m to the north (Gelfenbaum et al., 2015; Warrick et al., 2015).

2.3 Methodology

2.3.1 Ground-penetrating radar

Over 10 km (ninety-one lines) of ground-penetrating radar (GPR) profiles were collected on the Elwha River delta on 17-20 July 2016 (Fig. 2). GPR provides a useful tool for imaging sediment layers and storm deposits in coastal areas (Van Heteren et al., 1998; Buynevich et al., 2004; Wang and Horwitz, 2007; Tamura, 2012; Hein et al., 2014; Lindhorst and Schutter, 2014). The GPR data were collected using a hand-towed Sensors & Software pulseEKKO PRO GPR system (Sensors & Software Inc., Mississauga, Canada). Common-offset surveys were collected using 100 MHz, 200 MHz, and 500 MHz transducers. The frequencies obtain resolutions of 0.15 m, 0.10 m, and 0.03 m and penetrated to depths of up to 7 m, 5 m, and 2 m, respectively. The ground-water table at the Elwha River delta is located about 1.8 m below mean sea level and penetration of the GPR signal in some areas is limited by the presence of salt or brackish water, whose high dielectric constants spread the signal. GPR lines were collected primarily shore normal to image maximum dip angles, with twenty-one shore parallel lines for correlation.

Common-midpoint (CMP) surveys were conducted at both the western and eastern portions of the Elwha River delta to determine local radar velocities of the sediments. A radar velocity of ~0.107 m/ns was obtained for both sides, within the range reported for previous studies of sandy coastal areas (Switzer et al., 2006; Wang and Horwitz, 2007).

GPR data were processed using Sensors & Software EkkoView Deluxe by applying dewow, automatic gain control (AGC), bandpass filter, and a synthetic aperture image reconstruction migration to focus scattered signals. Elevation data were collected simultaneously using a HiPer Lite Plus RTK-GPS system (Topcon Positioning Systems Inc., Livermore, California, USA). After processing, GPR data were topographically corrected using a simple vertical shift of traces to correct for terrain using elevations obtained from the GPS survey and the average velocity of sediments obtained from the CMP surveys. GPR profiles were interpreted in IHS's Kingdom software using techniques discussed in Neal (2004) and Buynevich and Fitzgerald (2001). GPR data presented in this paper are from the 500 MHz transducers which provided the highest resolution images of the delta stratigraphy.

2.3.2 Sediment Cores

Seventeen vibracores, penetrating to depths of 0.5 m to 2.4 m, were taken along the same transects as GPR profiles to ground-truth GPR interpretations (Fig. 2). Cores were split, photographed and described, noting grain size, bedding surfaces, and any sedimentary structures. Grain-size analysis was conducted on samples from cores EW02, EW05, and EW07 (Figs 2 and 3) at 10 cm intervals using sieves at six grain-size intervals, ranging from -1.25 to 4 φ (2.38 mm to 62.5 µm). Mean grain size was determined from cumulative weight percent graphs (Folk and Ward, 1957). Cores were correlated to two-way travel time GPR profiles in Kingdom using velocities from the CMP surveys to obtain the correct time/depth relationships. When GPR profiles were converted to depth, geophysically imaged stratigraphic boundaries appeared to correlate with sedimentary contacts in cores, indicating a reasonable velocity was obtained from the CMP surveys.

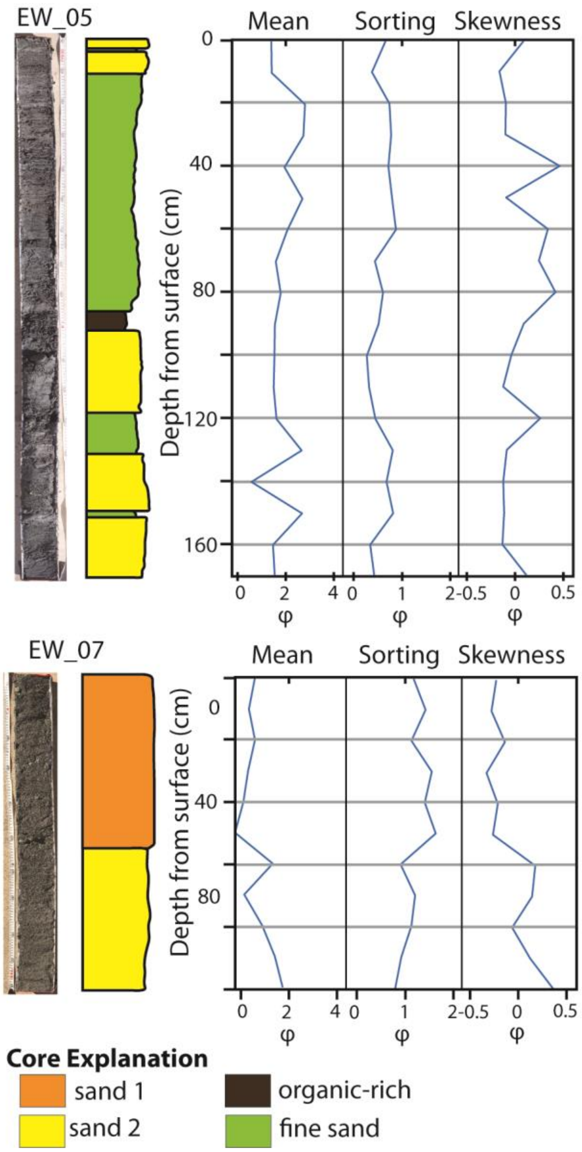

Figure 3. Vibracores EW_05 and EW_07 showing corresponding mean grain size, sorting, and skewness in phi. Grain size statistics were calculated according to Folk and Ward (1957).

2.3.4 Topographic Data and Maps

The USGS collected bathymetric and topographic surveys of the Elwha River delta before, during and after dam removal (Gelfenbaum et al., 2015). During the project, these data were collected biannually to capture seasonal aspects of the coastal morphodynamics as the delta grew from new sediment inputs. Methods included bathymetric measurements from single-beam sonar systems mounted to personal watercraft with differential Global Navigation Satellite Systems (GNSS) in real-time kinematic (RTK) mode and topographic measurements from RTK GNSS systems mounted on backpacks. Further details of data collection and processing are provided in Gelfenbaum et al. (2015) and data are provided in USGS ScienceBase (Stevens et al., 2016). Additional monthly topographic surveys were collected along a single transect (164 in the USGS surveys; Fig. 2) using a pole-mounted RTK-Differential Global Positioning System (DGPS). Topographic survey data from July 2016 were used to calculate the modern slopes of the delta landforms.

Aerial orthomosaics of the Elwha River mouth were derived from National Park Service (NPS) photographic surveys conducted about every two to four weeks during the dam removal project (Ritchie, 2014; East et al., 2015; Randle et al., 2015; Warrick et al., 2015). The orthophotos were developed from Structure-from-Motion analyses of thousands of aerial photographs per survey using Agisoft Photoscan Pro georeferenced with more than 100 ground control points around the lower 30 km of the river and 10 km of the shoreline. The orthophotos taken in the study area (Fig. 2; red box) were used in combination with the topographic survey data to estimate the timing of mouth-bar deposition and swash-bar formation by the first appearance of bars.

2.3.5 River and Ocean Conditions

River discharge and turbidity data were examined to determine the influence of river discharge and sediment load on mouth-bar deposition. River discharge data were acquired from USGS gauge 12045500, located between the two removed dams (waterdata.usgs.gov last accessed on January 29, 2017) (Figs 2 and 4A). Turbidity data from USGS gauge 12046260, located below both dam sites, were used as a proxy for sediment load (waterdata.usgs.gov last accessed March 24, 2017) (Figs 2 and 4A). Average turbidity for the Elwha River throughout the study period was ~250 formazin nephelometric units (FNU) and ranged from 0 to 2850 FNU.

In addition, significant wave heights and wave direction were examined to determine the effect of waves on both mouth- and swash-bar formation, migration, and welding. Oceanographic information was collected by two benthic tripods located east of the Elwha River mouth from December 2010 to November 2017 (Ferreira and Warrick, 2017; Glover, 2018) (Figs 2 and 4B). A 1200 kHz RDI acoustic Doppler current profiler (ADCO) mounted to the top of the tripod recoded current and wave conditions (Foley and Warrick, 2017). Tripod A was placed about 1 km east of the Elwha River mouth, but due to exceptional sedimentation at its site in the winter of 2013, it was relocated further east and renamed Tripod D (Ferreira and Warrick, 2017) (Fig. 2). Data from both tripods has been compiled into one time series. In order to capture the full study period and storm surge, tidal data from NOAA CO-OPS Station 9444090 offshore of Port Angeles, WA were examined (tidesandcurrents.noaa.gov last accessed January 31, 2017) (Figs 2 and 4C-D). Water level data were filtered to display only the maximum water level per 24-hour period. Additionally, the predicted tide was subtracted from the observed tide to show periods of storm surge and its effect on swash-bar migration and erosion. Storm surge is defined as occurring when the observed tide is greater than the predicted tide. For the purposes of this study, significant storm surge is defined as a period where the difference is equal to or above +0.5 m.

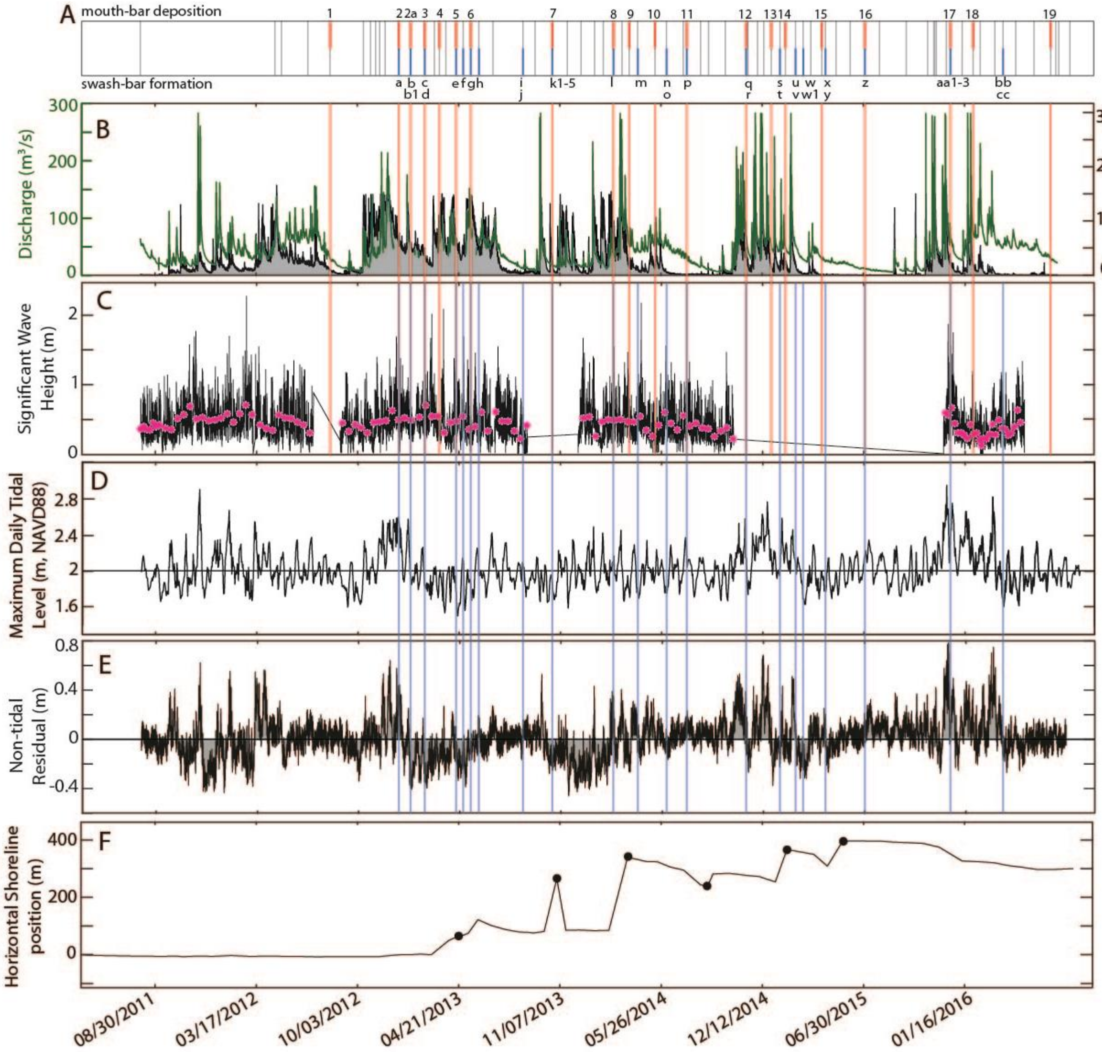

Figure 4. Time series of river and ocean data from August 2011 to August 2016. A) Red lines indicate the date of observed mouth-bar deposition, with numbers indicating the event name. Blue lines indicate the date of observed swash-bar formation, with letters indicating event name. Grey lines show the dates of aerial photographs and elevation surveys that were used to constrain bar formation timing. B) Elwha River discharge from USGS 12045500 and turbidity from USGS 12046260; C) Significant wave heights from benthic tripods A and D located east of the Elwha River delta mouth. Pink asterisks indicate the weekly average; D) Maximum daily water level data from NOAA CO-OPS Station 9444090 offshore Port Angeles, WA.; E) Difference in observed and predicted water levels from NOAA CO-OPS Station 9444090 offshore Port Angeles, WA.; F) Horizontal position of mean high water along the Elwha River delta shoreline at transect 164, with the 11 Feb 2011 shoreline as the zero-horizontal position. Black dots indicate dates that swash bars formed on transect 164.

2.3.6 Mouth-bar deposition and swash-bar formation timing

The timing of mouth-bar deposition and swash-bar formation was estimated using aerial photographs and elevation surveys. Mouth-bar deposition was recognized in aerial photographs by the presence of radial sand bodies at the river mouth, which appeared subaerially in photographs, but may be subaqueous during high tides (Fig. 1A). In elevation surveys, mouth bars were recognized again by a radial shape outward form the river mouth. In addition, the mouth bars gently slope seaward from the river mouth to the leading edge, before steeply sloping into deeper water.

Swash-bar formation was recognized in aerial photography as subaerial elongate features, parallel to and at the leading edge of the delta (Fig. 1B). In elevation surveys, the swash-bars appear similarly, and have higher slopes landward than seaward. Classification of swash bars as downdrift, updrift, and center, were based on the formation location of the swash bar, and the direction in relation to the river mouth in the aerial photographs and elevation surveys (i.e. center formed directly in front of the river mouth). The date of mouth-bar deposition and swash-bar formation is noted as the date it is first seen in either aerial photographs or elevation surveys, and therefore represents the latest possible date of formation (Tables 1 and 2). Mouth bars and swash bars may have formed and eroded in the roughly two-week time frame between each aerial photograph.

Table 1. Comparison of different variables influencing mouth-bar deposition.

Date	Mouth bar name	Discharge peak (m^3/s)	Turbidity peak (FNU)	Average Significant Wave Height (m)	Average maximum daily water level (m)
8/10/2012	1	156	1030	N/A	2.03
12/24/2012	2	213	1420	0.66	2.43
1/16/2013	2a	175	1330	0.51	2.17
2/13/2013	3	N/A	814	0.49	1.97
3/14/2013	4	N/A	1400	0.43	1.89
4/16/2013	5	115	1420	0.39	1.9
5/15/2013	6	152	1420	0.48	1.82
10/23/2013	7	282	2820	N/A	1.89
2/21/2014	8	232	2190	0.48	2.01
3/24/2014	9	278	2850	0.62	1.79
5/14/2014	10	111	790	0.46	2.07
7/16/2014	11	--	--	0.51	2.22
11/10/2014	12	211	1200	0.41	2.11
12/30/2014	13	282	1500	N/A	2.36
1/27/2015	14	167	687	N/A	2.05
4/9/2015	15	88	362	N/A	1.97
7/3/2015	16	--	--	N/A	2.05
12/19/2015	17	278	1490	0.55	2.44
2/2/2016	18	282	1490	0.31	2.32
7/4/2016	19	63	217	N/A	2.03

Table 2. Swash bar formation variables.

Date (formed between)	Swash bar name	Location	Average Significant Wave Height (m)	Average Maximum Daily Water Level (m)	Migration Length (months)	Average Significant Wave Height during migration (m)	Average Maximum Daily Water Level during migration (m)	% of time migration time with significant storm surge	Current Status
11/27-12/24/2012	a	center	0.66	2.43	--	--	--	--	eroded
12/24/2012-1/16/2013	b	updrift	0.51	2.17	3 months	0.55	1.96	0.00	welded to shoreline; later eroded by waves
12/24/2012-1/16/2013	b1	downdrift	0.51	2.17	--	--	--	--	welded to shoreline; later eroded by waves
1/16-2/13/2013	c	center/updrift	0.49	1.97	2-3 months	0.55	1.89	0.00	eroded
1/16-2/5/2013	d	downdrift	0.49	1.97	3-4 months	0.51	1.89	0.00	welded to shoreline
3/27-4/16/2013	e	center	0.39	1.90	1 month	0.43	1.86	0.00	eroded
4/16-4/30/2013	f	center	0.48	1.80	--	--	--	--	eroded
4/30-5/15/2013	g	downdrift	0.48	1.82	4 months	0.45	1.98	0.00	inner most bar on downdrift side
5/15-5/31/2013	h	center	0.41	1.97	--	--	--	--	eroded
6/28-8/26/2013	i	center	0.46	2.00	3 months	0.42 (6/30-9/4)	1.97	0.00	eroded
6/28-8/26/2013	j	downdrift	0.46	2.00	3 months	0.42 (6/30-9/4)	1.97	0.00	eroded
9/19-10/23/2013	k1	updrift	N/A	1.89	1.5 years	N/A	2.03	0.66	welded to shoreline
9/19-10/23/2013	k2	updrift	N/A	1.89	--	--	--	--	eroded
9/19-10/23/2013	k3	downdrift	N/A	1.89	4 months	0.44 (12/12-2/1)	1.97	0.06	middle bar on downdrift side
9/19-	k4	downdrift	N/A	1.89	2 months	N/A	1.94	0.09	eroded

10/23/2013									
9/19-10/23/2013	k5	downdrift	N/A	1.89	2 months	N/A	1.94	0.09	welded to shoreline
2/1-2/21/2014	l	downdrift	0.48	2.01	--	--	--	--	eroded
3/24-4/10/2014	m	downdrift	0.37	2.00	8-9 months	0.41 (3/24-10/16)	2.03	1.03	welded to k3
5/14-6/6/2014	n	center/updrift	0.40	1.98	1-2 months	0.42	1.99	0.00	eroded
5/14-6/6/2014	o	center	0.40	1.98	3-4 months	0.40	1.98	0.00	eroded
7/9-7/16/2014	p	center	0.51	2.22	1 month	0.44	2.01	0.00	eroded
9/30-11/10/2014	q	updrift	0.41 (9/30-10/16)	2.11	--	--	--	--	eroded
9/30-11/10/2014	r	center	0.41 (9/30-10/16)	2.11	--	--	--	--	eroded
12/30/2014-1/16/2015	s	center	N/A	2.05	--	--	--	--	overtaken by sediments from u
12/30/2014-1/16/2015	t	downdrift	N/A	2.05	--	--	--	--	overtaken by sediment from v
1/27-2/16/2015	u	center	N/A	2.17	--	--	--	--	eroded
1/27-2/16/2015	v	downdrift	N/A	2.17	--	--	--	--	welded to k3
2/16-3/3/2015	w	center	N/A	1.92	1 month	N/A	1.88	0.00	eroded
2/16-3/3/2015	w1	downdrift	N/A	1.92	1-2 months	N/A	1.91	0.00	overtaken by sediments from y
4/9/2015-4/16/2015	x	updrift	N/A	1.85	4 months	N/A	2.01	0.00	welds to shoreline
4/9/2015-4/16/2015	y	downdrift	N/A	1.85	5 months	N/A	2.00	0.93	outermost bar on downdrift side
6/4-7/3/2015	z	downdrift	N/A	2.05	4-7 months	N/A	2.02	0.00	eroded
12/11-12/19/2015	aa	center	0.55	2.44	1 month	0.50	2.33	4.44	eroded
3/16-4/1/2016	bb	updrift	0.42	1.89	2-3 months	0.40 (3/16-5/12)	1.91	0.00	outer bar on updrift side
3/16-4/1/2016	cc	downdrift	0.42	1.89	2-3 months	0.40 (3/16-5/12)	1.91	0.00	outer bar of near mouth

2.4 Results

2.4.1 Radar Facies and Depositional elements

GPR profiles contain five distinct radar facies distinguished by reflection configuration and continuity (Fig. 5). Sediment cores contain four sedimentary facies distinguished by grain size and sorting (Figs 3 and 6). Three different depositional elements were identified using radar profiles, sediment cores, elevation surveys and aerial photographs. These include foreshore, swash bar, and swale. Each of the depositional elements produces a distinct radar facies or facies assemblage.

The first radar facies, f1-be, consists of planar, seaward-dipping, parallel, continuous reflections (Fig. 5). Reflections from this facies have minimum seaward dip angles ranging from ~3° to 8° and are commonly found on the seaward side of swash bars as well as proximal to the pre-dam removal shoreline in both pre-and post-dam removal sediments (Figs 7, 8, and 9). Often within this facies, reflections are truncated and then overlain by the same facies, creating a seaward-dipping erosional contact, henceforth referred to as an erosional surface (Figs 7 and 9). Sediment cores sampling this facies contain sedimentary facies sand 1 and sand 2. Sand 1 is a poorly sorted, coarse-skewed sand with grain sizes ranging from -0.3 to 0.7 φ (0.6 to 1.2 mm) (Figs 3 and 6). Sand 2 is a poorly sorted, fine-skewed to near-symmetrical sand with grain sizes ranging from 0.3 to 1.7 φ (0.3 to 0.8 mm) (Figs 3 and 6). Cores also show possible imbricated clasts within sand 1, as well as shallowly dipping laminations within sand 2. Similar to other interpretations from coastal settings, facies f1-be is interpreted to be foreshore deposits, representing beach progradation (Van Heteren et al., 1998; Bristow et al., 2000; Buynevich and FitzGerald, 2001; Bristow and Pucillo, 2006; Switzer et al., 2006). This interpretation is further supported by the similarity of the reflection dip angles to the current foreshore dip angles at ~4° to 8°, calculated from the July 2016 topographic survey. Aerial photographs suggest the progradation is facilitated by longshore drift of swash-bar sediments initially deposited close to the river mouth. The erosional surfaces are interpreted to be caused by wave erosion during large storms (Buynevich and FitzGerald, 2001).

The second identified radar facies, f2-ch, is characterized by highly discontinuous chaotic reflections (Fig. 5). Aerial photographs show that this facies is found in areas that are currently, or were, in swales formed behind subaerial swash bars as the Elwha River delta prograded into the Strait of Juan de Fuca (Figs 8 and 9). Sediment cores sampling this radar facies contain a fine sand facies composed of moderately well sorted fine sands with a mean grain size of ~2.2 φ (200 μm), and an organic rich sedimentary facies containing large amounts of woody debris (Figs 3 and 6). Based on both aerial photographs and sediment cores, radar facies f2-ch is interpreted to represent swale deposits.

Two additional radar facies appear on the modern swash bars within the eastern side of the delta, and interbedded within the progradational beach deposits, facies f1-be, on the western side of the delta. The first of these is radar facies f3-ow which contains planar, steeply landward-dipping, parallel, continuous reflections (Fig. 5). The reflections of this facies have dip angles of ~27° and appear on the landward side of swash bars as well as within packages of GPR facies f1-be, progradational beach deposits (Figs 7, 8, and 9). The second radar facies that appears on swash bars, f3a-dl, consists of shallowly landward-dipping, divergent reflections, with dip angles ranging from 3° to 5° (Fig. 5). This radar facies is often found on the seaward side of preserved swash bars onlapping onto a bounding surface, as well as within the central portion of modern swash bars (Figs 7 and 9). Sediments corresponding to this radar facies consist of sedimentary facies sand 1 and sand 2, composed of moderately to poorly sorted sands that generally coarsen upwards within the swash bar from sand 2 to sand 1 (Fig. 6). Aerial photographs in locations where these facies are found display evidence of overwash processes (Fig. 10) as well as landward migration of swash bars (Fig. 11). Both radar facies are interpreted to be caused by a combination of overwash processes and slip-face migration on swash bars (Psuty, 1965; Hine, 1979; Bristow et al., 2000; Lindhorst et al., 2008).

Several profiles contain reflection free areas that occur near the surface. These occur most often within GPR transects close to the active shoreline (Figs 7 and 8). Reflection free areas close to the surface are defined as radar facies, f4-hsc (Fig. 5). This facies is interpreted to indicate locations with high salt- or brackish water concentrations. Salt has high conductivity, which increases the attenuation of electromagnetic waves (Neal, 2004).

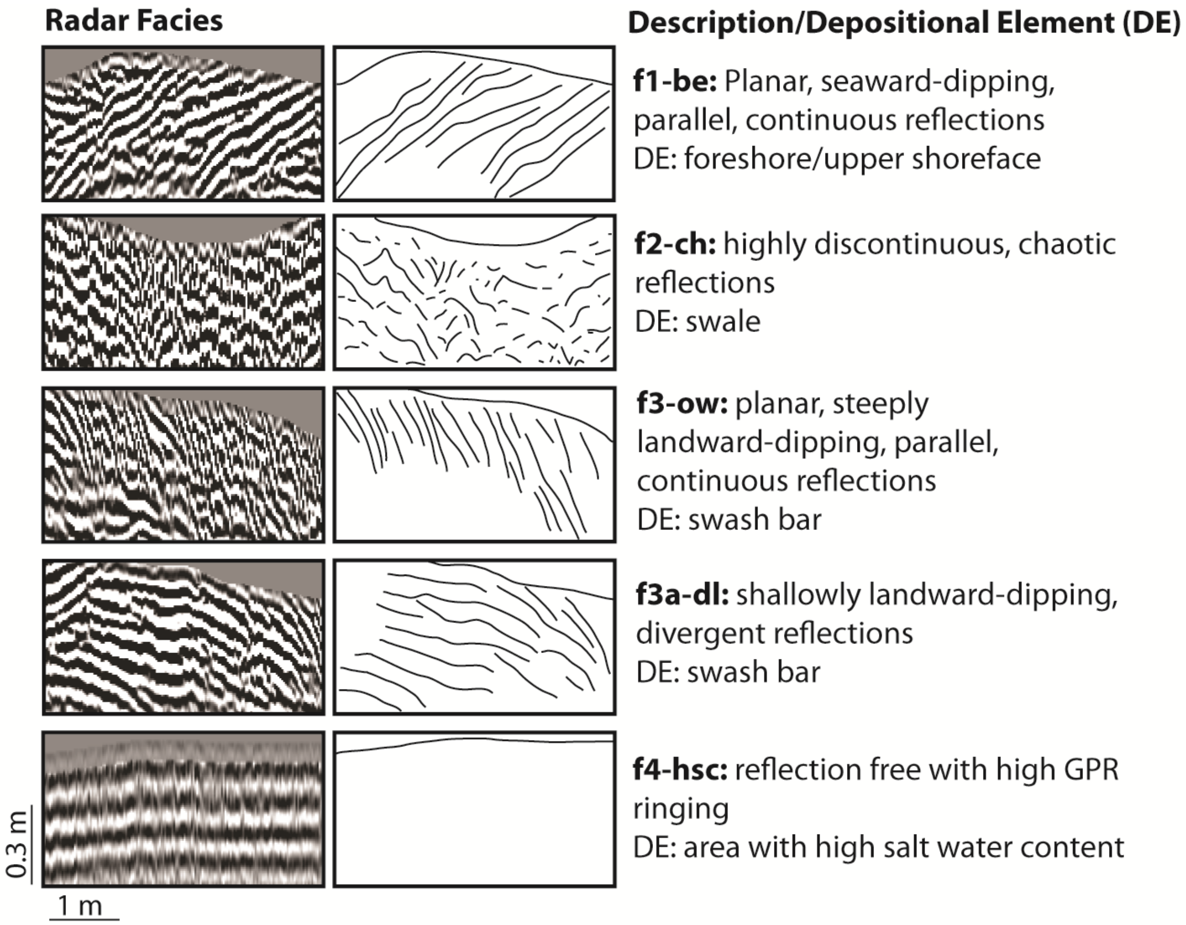

f1-be: Planar, seaward-dipping, parallel, continuous reflections
DE: foreshore/upper shoreface

f2-ch: highly discontinuous, chaotic reflections
DE: swale

f3-ow: planar, steeply landward-dipping, parallel, continuous reflections
DE: swash bar

f3a-dl: shallowly landward-dipping, divergent reflections
DE: swash bar

f4-hsc: reflection free with high GPR ringing
DE: area with high salt water content

Figure 5. Radar facies identified within GPR profiles and their interpreted depositional element. All figures have vertical exaggeration of 6.5X.

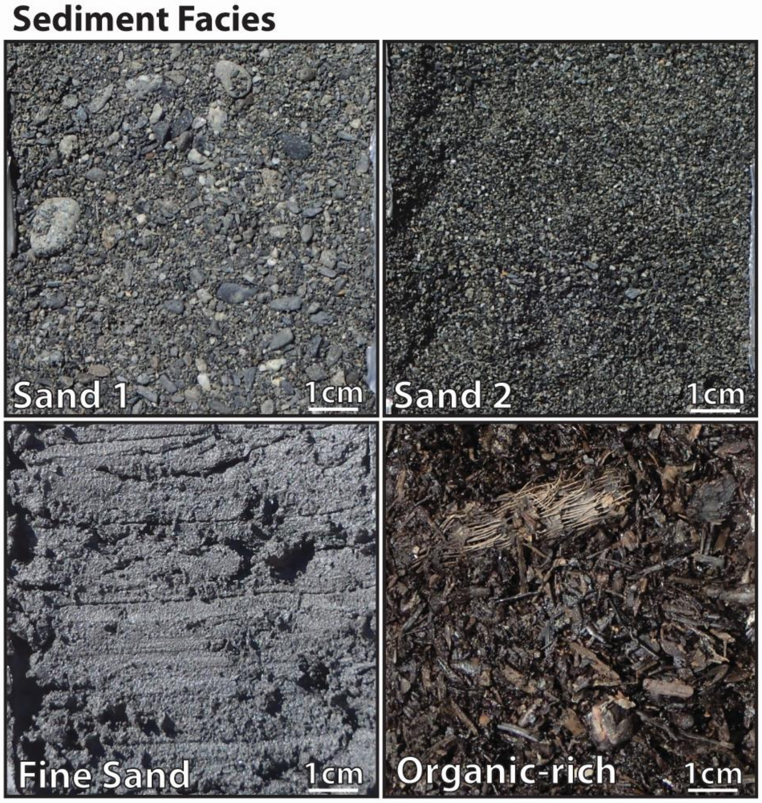

Sand 1: Poorly sorted sand, coarse skewed, with mean grain sizes ranging from -0.3 to 0.7 φ (0.6 to 1.2 mm), and clasts as large as -4.5 φ (2 cm); *Depositional element: foreshore, swash bars*

Sand 2: Moderately to poorly sorted sand, fine skewed to near symmetrical, with mean grain sizes ranging from 0.3 to 1.7 φ (0.3 to 0.8 mm); *Depositional element: foreshore, swash bars*

Fine sand: Moderately well sorter fine sands, near symmetrical, with mean grain size of 2.2 φ (200µm); *Depositional element: swale*

Organic-rich: woody debris; *Depositional element: swale*

Figure 6. Sedimentary facies identified within vibracores.

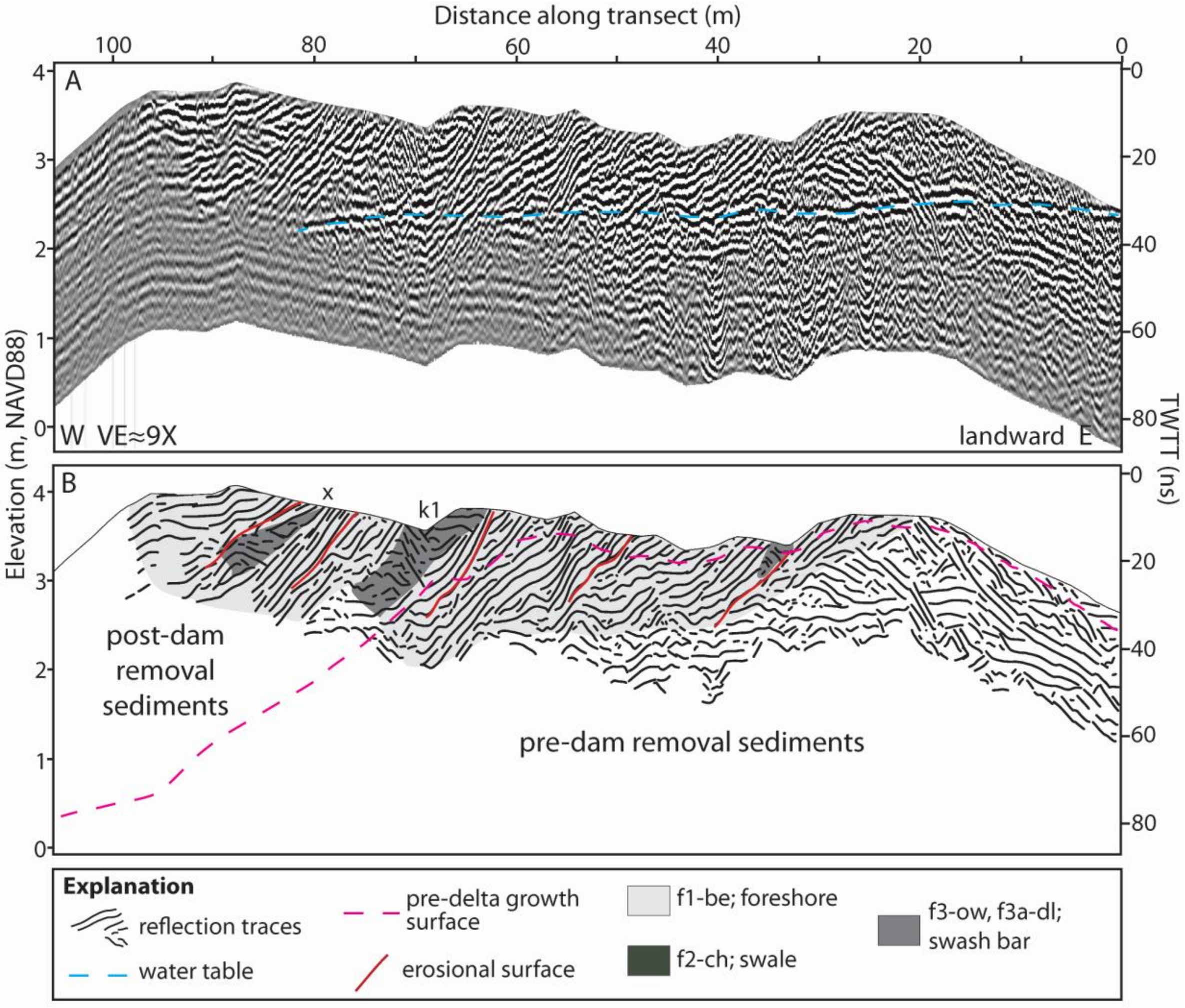

Figure 7. GPR profile from updrift side of Elwha River delta (see Fig. 2 for location) with interpretation of same line below. A) GPR profile with water table marked by dashed blue line. B) Interpreted GPR profile with depositional elements overlain, sediments deposited before dam removal are shown landward of the dashed pink line and sediments deposits after dam removal are seaward of the dashed pink line.

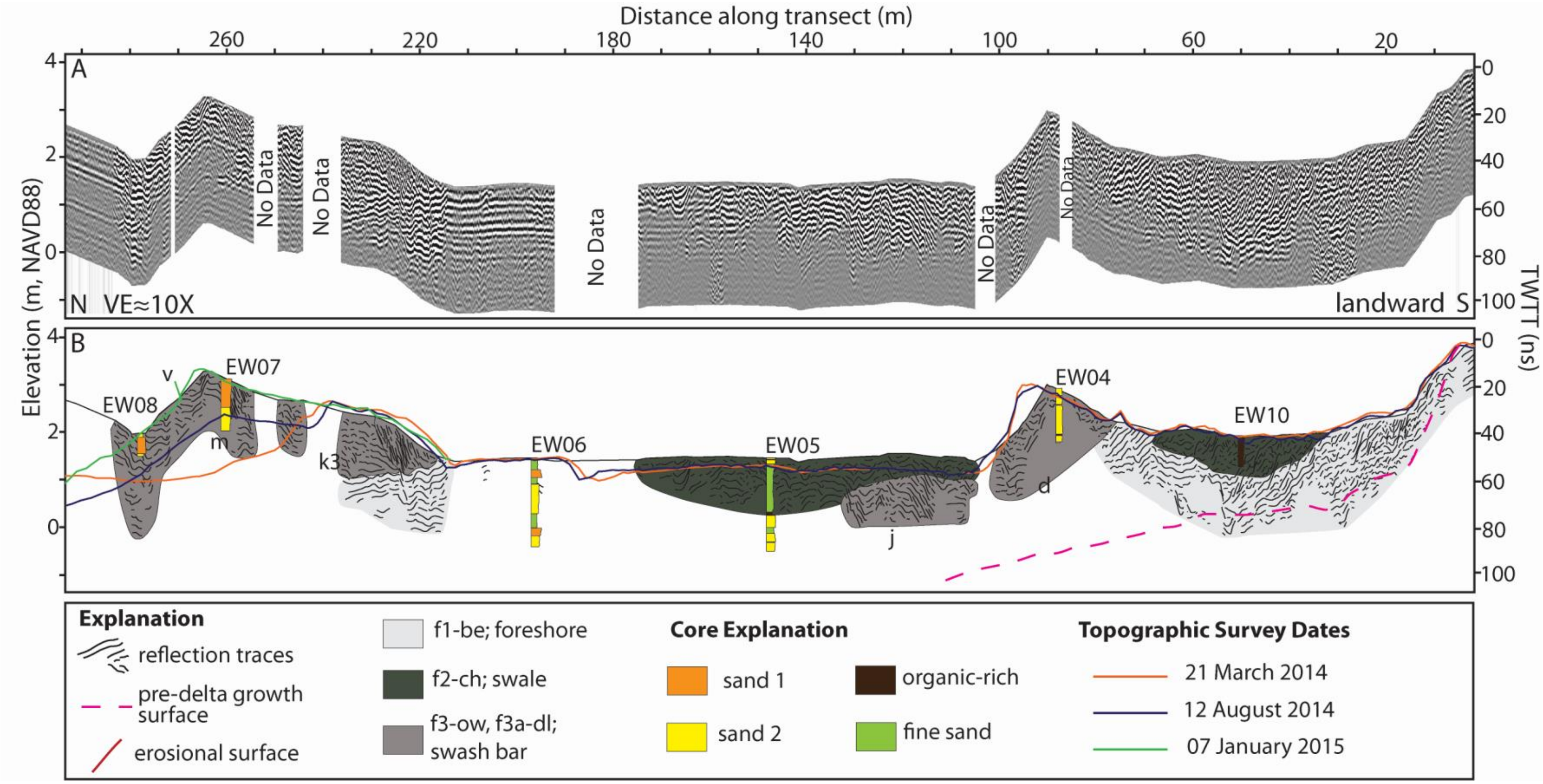

Figure 8. GPR profile from downdrift side of Elwha River delta (see Fig. 2 for location) with interpretation of same line below. A) Uninterpreted GPR profile. B) Interpreted GPR profile with depositional elements overlain. Cores are shown with their corresponding sedimentary facies. Topographic profiles are overlain showing the amalgamation of three different mouth bars as interpreted from aerial photographs, topographic profiles, and radar facies f3-ow and f3a-dl. Each bar is numbered with its corresponding number from Table 2.

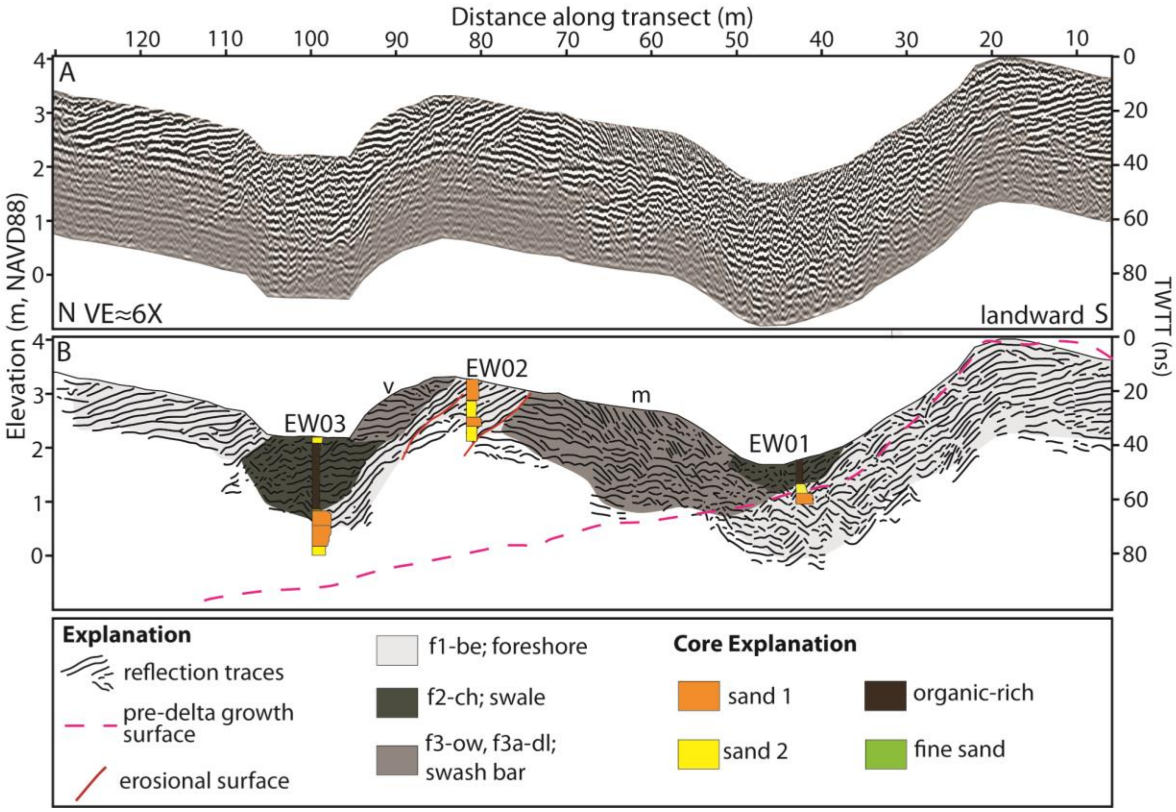

Figure 9. GPR profile from downdrift side of Elwha River delta (see Fig. 2 for location) with interpretation of same line below. A) Uninterpreted GPR profile. B) Interpreted GPR profile with depositional elements overlain. Cores are shown with their corresponding sedimentary facies.

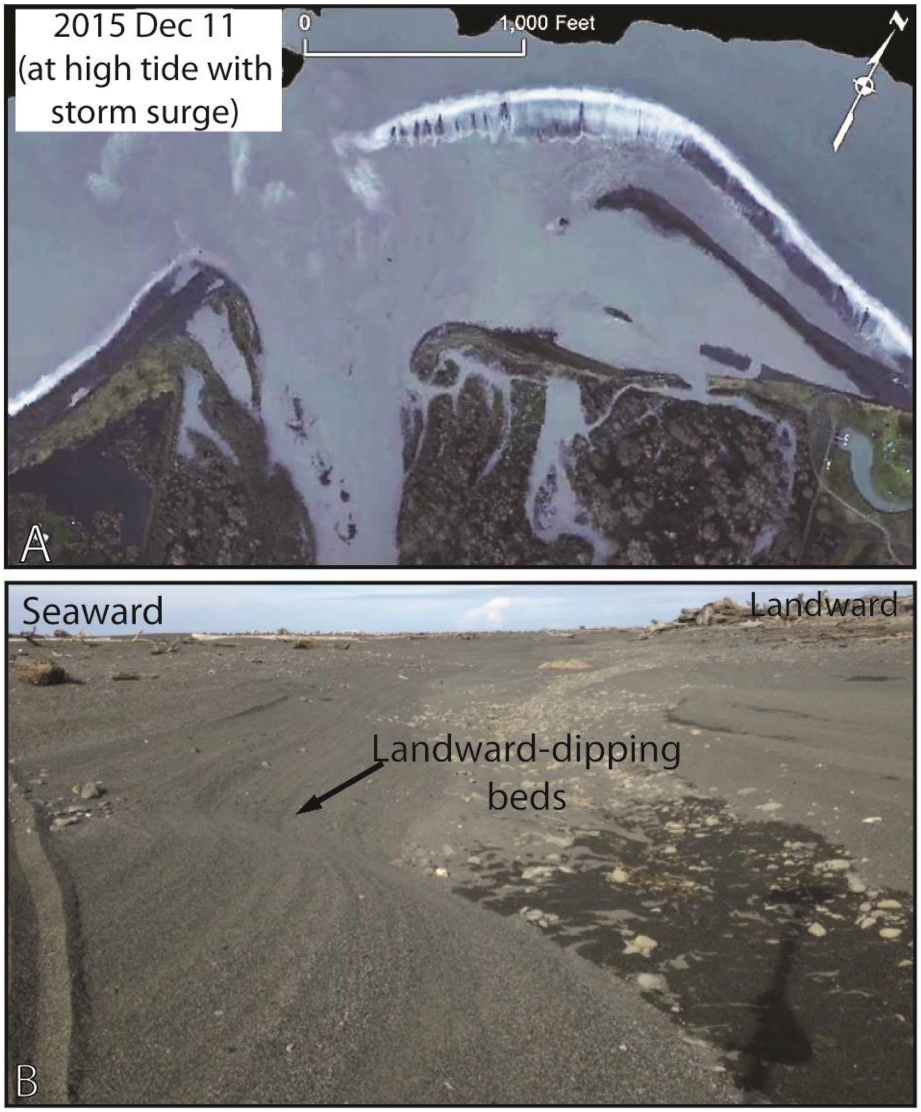

Figure 10. A) Aerial photograph showing overwash from storm waves occurring on the Elwha Delta in December 2015. B) Photo from July 2016 showing landward dipping beds on the landward side of a mouth bar. (Photos by A. Ritchie and A. Simms).

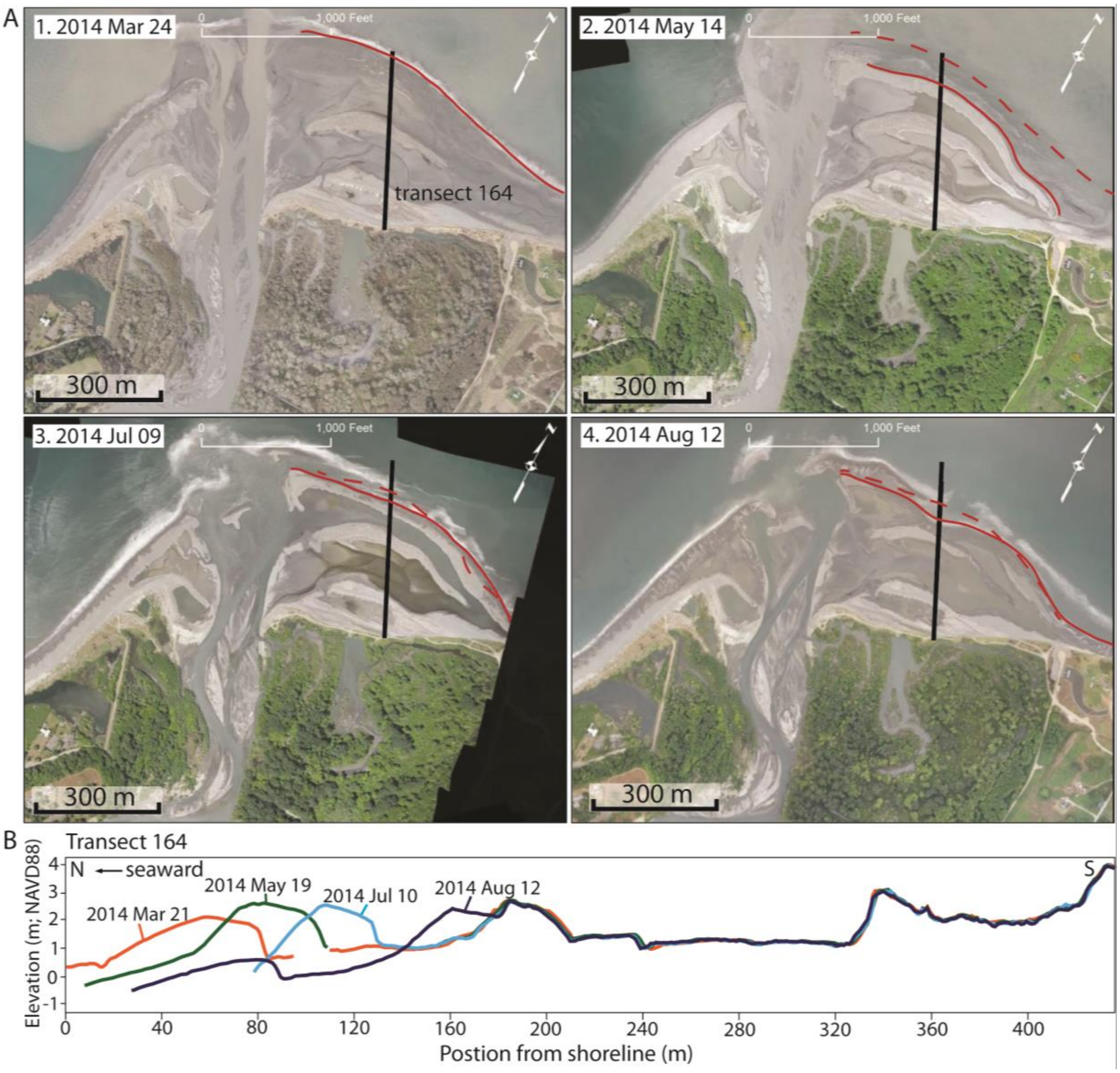

Figure 11. A) Aerial photographs showing the formation and landward migration of elongate swash bars on the Elwha River delta from March 2014 to August 2014. Solid red lines show the location of the swash bar in the current frame, red dashed lines show the swash bar locations from the previous frame. Black line shows the location of transect 164. B) Topographic profiles along transect 164 showing the landward migration of the same swash bar from March 2014 to August 2014. (Photos by A. Ritchie).

2.4.2 Mouth-bar morphology and formation

After dam removal, the Elwha River delta prograded seaward, facilitated by nineteen episodes of mouth-bar deposition at the delta front during the study period. These bars radiated laterally out from the river mouth in a crescentic shape. The river mouth continued to migrate through the newly formed delta plain, and often formed lozenge shaped mouth bars, as well as triangular plan-form mouth bars, known to form from sediment pulses and wave action (Fielding et al., 2005). While the exact timing of mouth-bar deposition was not captured, aerial photographs and topographic surveys were used to bracket their timing. Therefore, discharge and turbidity (a proxy for sediment load) were explored within the time frame of possible deposition. Preceding deposition of seventeen of the nineteen mouth bars between August 2011 to August 2016, discharge and/or turbidity, as measured from river gauges, increased to levels above average with discharge ranging from ~60 to ~280 $m^3 s^{-1}$ and turbidity from ~200 to ~2850 FNU, for one to five days (Fig. 4; Table 1).

2.4.3 Swash-bar formation and migration

A total of thirty-seven swash bars formed on the Elwha River delta between August 2011 and August 2016 (Table 2). The formation of swash bars was either concurrent with or within two months mouth-bar deposition. All but three episodes of mouth-bar deposition and growth resulted in the formation of one to five swash bars. Wave action reworked the deposits creating a wave-dominated delta morphology on the delta plain (Gelfenbaum et al., 2015). Elevations of the swash bars ranged from ~3 to 3.75 meters (relative to NAVD88, NOAA CO-OPS Station 9444090, co-ops.nos.noaa.gov; 1.8 to 2.55 m above mean sea level based on the datum measured at NOAA CO-OPS station 9444090; Fig. 2). Fourteen swash bars formed near the center of the delta and all were subsequently eroded or reworked into other deposits. Fifteen swash bars formed on the downdrift side of the delta. Eight of the fifteen swash bars were either eroded or reworked, and seven remained preserved either in the GPR stratigraphy or morphologically as of July 2016. Of the additional eight swash bars that formed on the updrift side of the delta, five were eroded and three remained preserved either in GPR stratigraphy or morphologically.

Of the thirty-seven swash bars formed during the study period, twenty-three formed when wave data was available. Wave direction during the study period was predominately from the NW with a median significant wave height of 0.4 m (Fig. 12). The average significant wave heights during possible swash-bar formation periods ranged from 0.66 m to 0.39 m (Fig. 4). Twelve of the twenty-three swash bars formed when significant wave heights were above the median for the study period. The average maximum daily water level in each potential formation period, derived from tidal data, also ranged from 2.44 m to 1.82 m with twenty-three of thirty-seven swash bars formed when the maximum daily water level was lower than average.

After formation, the swash bars either remained stationary, migrated landward, or were subsequently eroded by channel migration. Only two of the swash bars in the study were completely eroded by wave action, one on the updrift side of the delta and one on the far downdrift side. Twenty-six of the thirty-seven swash bars migrated, moving landward towards the shoreline, with additional lateral growth to the east in the direction of littoral drift, often slightly narrowing the swash bar (Fig. 11). Migration lasted on average three months but ranged from just under one month to over a year and stopped when the swash bar amalgamated to the shoreline or when another bar formed seaward of the initial bar. As the bars migrated, they left behind a large subaqueous platform on top of the mouth bars.

Sparse wave data captured all or part of sixteen swash bars' migration period (Fig. 4). Nine of those swash bars migrated over a period where average significant wave heights were greater than average for the study period. Tidal data was available for the entire study period and captured all twenty-six migration periods. The average maximum daily water levels during migration periods ranged from 1.86 to 2.33 m and was lower than the study period average in eighteen of the twenty-six periods. Significant storm surge occurred during ten migration periods and ranged from occurring 0.06% to 5% of the total time. Migration of swash bars occurred throughout most of the study period, with notable exceptions from January to March 2014, October to February 2015, and January to March 2016.

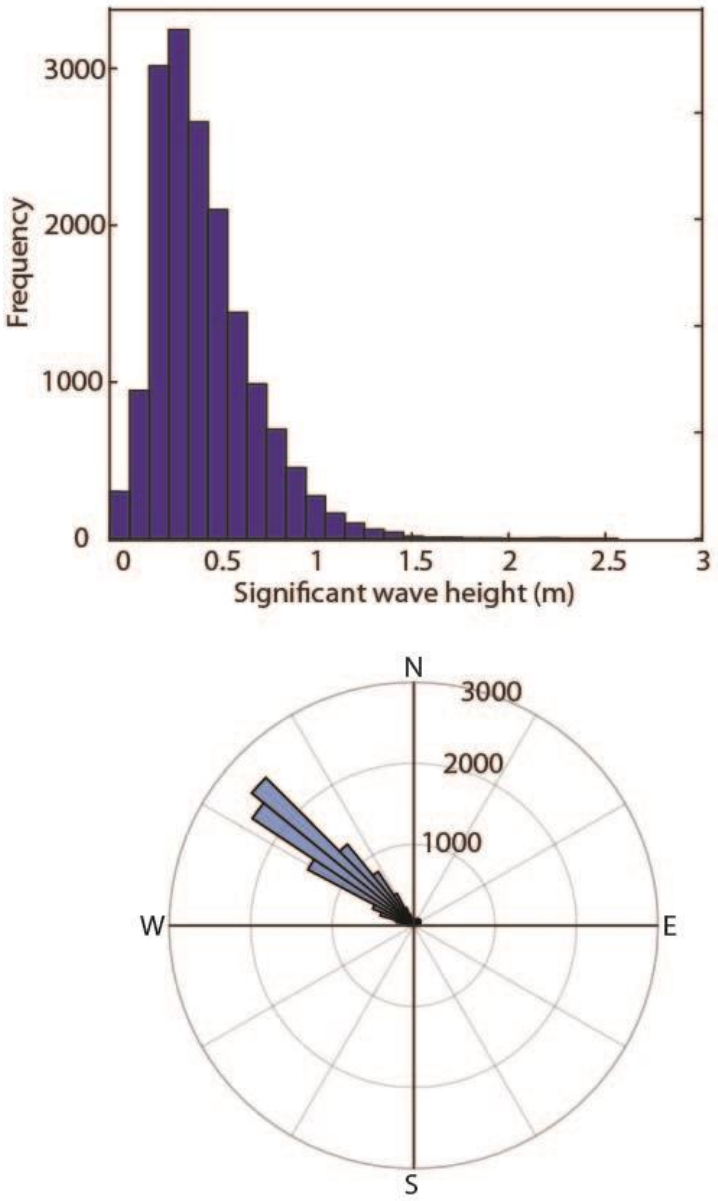

Figure 12. A) Histogram of significant wave heights from benthic tripods A and D from August 2011 to October 2014; B) Rose diagram showing dominate wave direction at benthic tripods A and D.

2.4.5 Downdrift vs. Updrift Stratigraphy

The updrift and downdrift sides of the Elwha River delta contain similar radar and sediment facies, yet, the morphology and GPR stratigraphy of the two sides differ. At the time of the GPR survey in July 2016 the GPR stratigraphy of the updrift side of the delta was dominated by facies f1-be, or seaward-dipping foreshore and upper shoreface deposits. Small packages of swash-bar facies could be distinguished within GPR profiles, as well as erosional surfaces. The topography shows one swash bar offshore of a steeply sloping beach (~10°). The downdrift side of the delta contained a mix of foreshore, swash bar, and swale GPR facies, which are absent from the updrift side. Additionally, fine-grained sands and organic material are absent from the updrift side but are found in the swales and as thin beds within the swash bars of the downdrift side. The downdrift side of the delta also has a more defined ridge and swale topography, with three swash bars captured in the elevation surveys (Figs 8, 9, and 11).

2.5 Discussion

2.5.1 Mouth-bar deposition

Mouth bars often form on wave-dominated deltas after high-magnitude river discharge events, such as large floods (Fielding et al., 2005; Barnard and Warrick, 2010; Anthony, 2015). At the Elwha River delta, seventeen of nineteen mouth bars were deposited after short-term increases in river discharge. However, these increases in river discharge were still lower than the two-year recurrence flood interval of 400 $m^3 s^{-1}$ and river discharge shows no significant changes before and after dam removal, so another factor likely contributed to the formation of mouth bars. From September 2011 to July 2013 and likely beyond, the Elwha

River experienced an increase in sediment supply (Magirl et al., 2015). The excess sediment supplied to the Elwha River from the dam removal is comparable to the large sediment load delivered after wildfires, landslides, volcanic eruptions, and typhoons (Foley et al., 2015). This 2+ years of sustained sediment supply from eroded sediment trapped behind the dams in the Elwha River system was enough to form mouth bars during lower discharge than normally required in other systems or prior to dam removal. This contrasts with the larger systems, such as the Brazos and Danube, which are thought to form barriers only after large river discharge events (Rodriguez et al., 2000; Bhattacharya and Giosan, 2003).

Not all increases in discharge in the Elwha River, however, correlated with mouth-bar deposition, including two peaks to over 200 m^3 s^{-1} at the beginning of the study period in November 2011 and one in February 2015. One possible explanation for the discrepancy at the beginning of the study period is that the river needed time to fill the existing accommodation within the lower reaches of the river valley and on the subaqueous delta created after the dams were built in the early 1900s, before mouth bars could form. Significant wave heights during this time also tend to be higher overall and recent modeling has shown large waves can suppress mouth-bar formation (Jerolmack and Swenson, 2007; Nardin and Fagherazzi, 2012). The second period of high discharge not associated with mouth-bar formation may be a result of greater storm energy, but the lack of wave data precludes test of this hypothesis. Additionally, mouth bars may have been deposited subaqueously and at times in which the bathymetric surveys were unable to capture their deposition.

2.5.2 Swash-bar formation and depositional model

Previous studies of swash bars have focused on prograding shorelines and spits, where swash bars are thought to form after large storms reactivate sediment from the foreshore and dunes, and move it offshore, where it then nucleates into a bar (Hayes and Boothroyd, 1969; Lindhorst et al., 2008). However, the genesis of the swash bars at the Elwha River delta differs in that the sediment source for the swash bars has a direct fluvial origin. All but two swash bars form within a month of mouth-bar deposition, and the two that form later are initially seen at lower tidal levels than their previous aerial photograph, indicating they may have simply been subaqueous following mouth-bar deposition. The clear association of swash bars with mouth-bar deposition suggests that the mouth bars provide the sediment that is immediately reworked by waves to form swash bars. Additionally, while high waves are known to hinder the formation of mouth bars (Nardin and Fagherazzi, 2012), available wave data suggests that wave heights at the Elwha River delta are not large enough to hinder swash-bar formation.

After formation, the swash bars migrate landward due to reworking of their sediments by waves. As the swash bar migrates, it tends to thin in the shore parallel direction as it grows laterally downdrift. Overwash processes and slip-face migration both form the landward-dipping stratification preserved in the sedimentary record (Figs 7, 8, and 9). Swash bars prevent waves from eroding the back-bar area, thereby preserving the bedsets that form as the swash bar migrates landward. Migration of swash bars occurred throughout most of the study periods except over three notable time periods. The migration did not occur during three of the winters (i.e. January to March 2014 and 2016, and October to February 2015), suggesting that stormier weather patterns, often more common during the winter, may inhibit migration. Significant storm surge also accompanied these periods, though, wave data do not indicate higher than average significant wave heights. Migration stops when the swash bar amalgamates to the shoreline or another swash bar, or a swash bar forms seaward of it, protecting it from wave action. Thus, multiple swash bars representing multiple high discharge events are preserved as a single amalgamated swash bar.

Two erosional surfaces were imaged in ground-penetrating radar and formed during the time period between elevation surveys taken in September 2014 and January 2015 (Figs 7 and 9). Erosion surfaces are caused by large storms (Buynevich et al., 2004), but little work has quantified how large waves must be to cause such erosion. During the time when erosion surfaces formed, at least one wave event with wave heights >1.5 m struck the delta, although a break in the wave data time series from October 2014 to December 2015 prevent further analysis. The sedimentary characteristics of deposits formed during a later period of wave activity with wave heights of >1.5 m in late 2015 was not captured in the GPR stratigraphy because of high salt-water conductivity in the area.

A simple model for the formation of swash bars on small wave-dominated deltas is proposed (Fig. 13). After a high discharge event with enough sediment available in the system, a large mouth bar will be deposited on the delta front. Concurrently, wave action reworks the mouth-bar sediments to form swash bars at the leading edge of both the downdrift and updrift sides of the delta. Fairweather wave processes dominate, and lead to the swash bar migrating shoreward, and downdrift. As the swash bar migrates, it leaves behind a platform created by the remaining mouth bar sediments on the delta plain, which continues to expand seaward with subsequent discharge events. The swash bar welds to the shoreline or stops migrating if another bar forms seaward of it following the next discharge event. Swash bars that do not weld to the shoreline on the downdrift side of the delta continue migrating in the direction of longshore drift, with their downdrift end eventually connecting to the shoreline. Local patches of finer sediment may be preserved between the migrating swash bar and subaqueous delta plain, such as the thin bed (~2 cm) of organic material found in core EW04 (Fig. 8). The migration of swash bars downdrift results in beach progradation, as seen by facies f1-be. High waves may erode the shoreface, or seaward side of the swash bars at any time during the welding process.

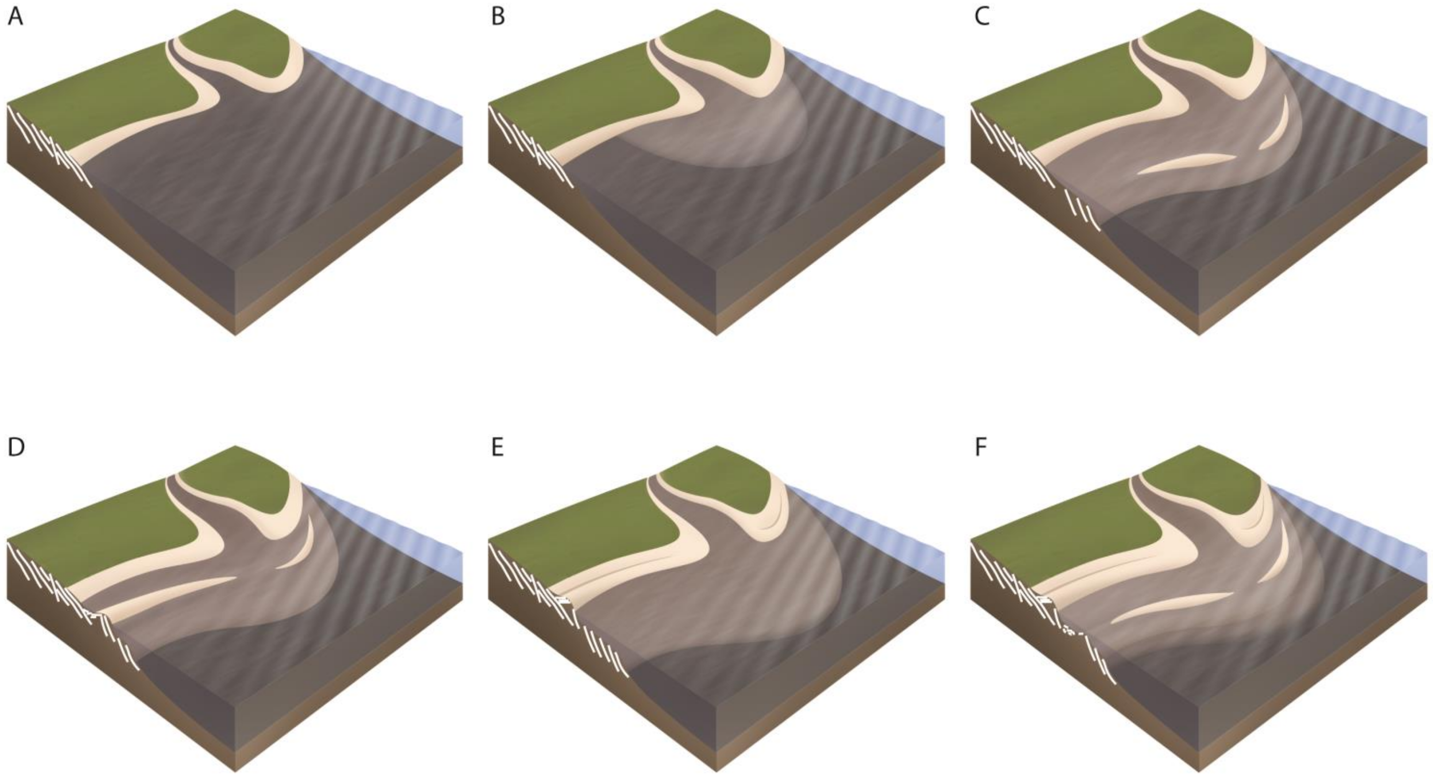

Figure 13. Schematic model for swash-bar welding on a delta. A) The initial delta starved of sediment. B) A mouth bar is deposited at the delta front. C) Wave action on the mouth bar reworks sediments, forming swash bars on both the updrift and downdrift edges of the delta, on top of the mouth bar. D). Wave action continues to rework the sediments of the swash bars, causing migration landward and downdrift in the direction of littoral drift. Swash bars have landward-dipping bedding on their landward side. The platform created by the mouth bar remains intact. E) The swash bars become welded onto the shoreface, with landward-dipping bedding preserved as evidence of their landward migration. F) The cycle continues, with another mouth bar deposited on the delta, and swash bars forming on top. (Schematic model drawn by Scott Condon).

2.5.3 Swash bar preservation potential

The preservation of the landward-dipping stratification provides a stratigraphic signature of swash-bar welding in the sediment and rock record. Elevation surveys overlain onto GPR profiles provide evidence of swash-bar migration and welding to form composite swash bars. The stratigraphic signature of swash-bar welding within GPR can record how many bars have welded onto an existing shoreline or swash bar to produce better records of past wave and discharge activity.

The potential for this signature to form and be preserved is dependent on the location swash-bar formation on the delta. All swash bars formed at the center of the river mouth on the delta were eroded by channel migration. Aerial photographs suggest fifteen swash bars formed on the downdrift side of the delta since dam removal. In July 2016, only three of the swash bars were preserved or recognizable in elevation surveys and aerial photographs (Fig. 2). Aerial photographs show the erosion of swash bar j by channel avulsion; however, swash-bar facies, f3-ow, interpreted to be from this bar are preserved in GPR (Table 2; Fig. 8). Additionally, the GPR profile from transect 164 shows evidence that swash bar k3 is the composite of three different swash bars welded together (Table 2, bars k3, m, and v; Fig. 8). Elevation surveys provide evidence for swash bar y farther offshore on transect 164; however, GPR was unable to image sediments on this swash bar due to saltwater infiltration. Altogether, the GPR profile from transect 164 and elevation surveys recorded seven of fifteen swash bars formed on the downdrift side of the delta. Thus, due to potential erosion by the river channel or waves, the number of preserved swash-bar signatures will be a minimum estimate of the number of swash bars that formed.

In July 2016, aerial photographs and elevation surveys show one subaerial swash bar, bar bb, on the updrift side of the delta (Fig. 2). GPR profiles from the updrift side of the delta contain evidence of two swash-bar welding events that occurred during the study period within the stratigraphy of the shoreface (Table 2, bars k1 and x; Fig. 7). However, aerial photographs and elevation surveys suggest that after the initiation of dam removal, at least eight subaerial swash bars formed on the updrift side of the delta, thus at least five swash bars were not captured in the stratigraphic record.

Two factors favored formation and preservation of swash bars on the downdrift side of the delta. First, littoral drift increases the sediment supplied to the downdrift side of the delta, increasing the likelihood of swash-bar formation. Second, the downdrift side of the delta develops swales that persist over several years and provide accommodation for the deposition of swash bar overwash sediment, enhancing the preservation potential of the bar welding signature. Although swales are formed on the updrift side of the delta behind swash bars, these areas usually disappear after several months. For the signature of swash-bar welding to be preserved, there must be sufficient time and sediment deposition between swash-bar welding and significant shoreface erosion by the prevailing wave- and tidally-driven currents (Warrick et al., 2009; Eidam et al., 2016). Additionally, channel avulsion may erode swash bars and other sediment deposited on the delta (Gelfenbaum et al., 2015). The stratigraphic record does not preserve every swash bar that formed and may only be used to determine a minimum number of bar welding events.

At the Elwha River delta, the sediment load of the river returned to pre-dam removal levels by the end of 2016, and the delta no longer experienced periods of enhanced mouth-bar formation or extension. The swash bars that remained preserved in the delta all were welded swash bars that formed after earlier high discharge events. Satellite imagery reveals as of

2017, that what had initially been six swash bars (Table 2, bars k3, m, v, t, w1, and y) formed by different river discharge events from October 2013 to April 2015, were all amalgamated into one large barrier on the outer edge of the downdrift side of the delta (Fig. 14). This indicates that the sediment that was added to the fluvial system by the removal of the two dams was not remobilized during a single high discharge event, as no multiyear floods occurred during the study period, or even over one season, but over several seasonally high discharge events over at least four years. This contrasts with larger deltaic systems where individual swash bars are often thought to represent large floods and have been linked to climate cycles (Fraticelli, 2006; Tamura, 2012).

The welding of several of the swash bars into a large barrier suggests that in SMR wave-dominated deltas, the presence of several closely spaced swash-bar welding signatures in a larger barrier could be indicative of a large sediment pulse added to the fluvial system as a result of landslides, volcanic eruptions, or other sediment pulses. The new barrier developed as a result of the dam removal has similar dimensions as a vegetated ridge on the older Holocene delta plain, to the east of the current river delta (Fig. 14), suggesting that large sediment pulses may have created similar features in the past.

Figure 14. Satellite image from Google EarthTM showing delta morphology July 30, 2017, displaying the amalgamation of bars k3, m, v, t, w1, and y into the outer barrier on the delta, as well as a relict barrier on the older Holocene delta.

2.6 Conclusion

The sustained sediment supply following dam removal on the Elwha River delta led to the deposition of at least nineteen mouth bars following moderate increases in discharge and turbidity along the river. Within one month of initial mouth-bar deposition between one and five swash bars formed from wave action at the leading edge of sixteen of the nineteen new mouth bars. After formation the swash bars migrated landward and in the direction of littoral drift over a period of two months to over a year, until they welded to the shoreline or another swash bar or were eroded by the river channel. Within ground-penetrating radar profiles, the landward migration of these swash bars produced landward-dipping reflections, which in the case of swash-bar welding onlaps a seaward-dipping boundary surface which separates the landward-dipping reflections from the older seaward-dipping reflections marking normal beach progradation of the older beach or swash bar. Although the preservation potential of the swash-bar welding signature was higher on the downdrift side of the delta due to higher frequency of formation and accommodation created behind younger swash bars, not every swash bar survived or left a record of welding within GPR profiles. Thus, this signature can only be used to infer a minimum number of swash-bar welding events that occurred on the delta.

After the initial increase in sediment load due to dam removal decreased, the continued amalgamation and wave reworking of the surviving swash bars formed a larger barrier at the front of the delta plain. The barrier is similar in scale to older vegetated ridges on the delta plain. Although the creation of individual new swash bars correlates with higher than average discharge, the formation of the large barrier was not triggered by a single flood or storm, but sustained sediment supplied via normal seasonal high discharge over the course of several years. Thus, in SMR deltas the amalgamation of swash bars into a large barrier may be indicative of a large sediment pulse to the river system, rather than flooding on the river.

CHAPTER 3

3. Episodic Coastal Progradation of the coastal Oxnard Plain, southern California

3.1 Introduction

Coastal communities are increasingly threatened by rising sea levels and its impact will likely be exacerbated by droughts that reduce sediment yield to coastal systems (Inman and Jenkins, 1999). Studies have suggested that the intensity of droughts may increase in the future (Cayan et al., 2010; Trenberth et al., 2013). With nearly 80% of Californians living within 30 miles of the coast (Griggs et al., 2005), determining how rising sea-levels and increased intensity of droughts may affect the shoreline is important for preparing for the future. In areas that have exhibited long-term progradation, understanding how past prolonged droughts have affected the coastline may provide a better understanding of future scenarios.

Ground-penetrating radar (GPR) has been used extensively in coastal areas to characterize beach progradation (Bristow and Pucillo, 2006; Buynevich and FitzGerald, 2001; Van Heteren et al., 1998), determine storm and tsunami erosion histories (Buynevich et al., 2004; Buynevich et al., 2007; Oliver et al., 2017; Simms et al., 2017), and ultimately understand the coastal response to changes in climate and sediment supply though time (Tamura, 2012). However, little data is available for coastal areas subject to episodic sedimentation controlled by decadal to multidecadal climate cycles, such as the Pacific coast of the SW US. In part, this is because the Pacific coast of the US is an active margin, and in California 72% of the coast is backed by sea cliffs, rather than prograding beaches (Griggs et al., 2005). However, the coastal Oxnard Plain, with nearly 22 miles of sandy beaches, allows for an opportunity to image past sedimentation on the SW US Pacific Coast and study the effects of decadal climate cycles such as the El Niño Southern Oscillation (ENSO), as well as centennial climatic events, such as the Little Ice Age and Medieval Warm Period, on sedimentation patterns and rates. Specifically, the area downdrift of the Santa Clara River has exhibited progradation since at least 1855, when the first coastal maps of the area were made (Fig. 15) (Grossinger et al., 2011). This study aims to image and characterize the progradation of the coastal Oxnard Plain in order to determine how the preserved strata and progradation rate are influenced by decadal to multidecadal changes in climate.

3.1.1 Study Area

The Oxnard Plain is a 520 km^2 coastal plain that lies within the Ventura Basin of the structurally complex Transverse Ranges province of southern California (Fig. 16). The region has undergone deformation since the mid-Miocene when shear forces along the Pacific and North American plate boundary caused the clockwise rotation of the Western Transverse Block (Luyendyk, 1991). The Ventura Basin began undergoing subsidence around 5 Ma and filled with a thick succession (~12,000 m) of late Cretaceous to Cenozoic strata, including the thickest section of Pleistocene sediments in the world (Winterer and Durham, 1962; Yeats, 1977). Strong north-south contraction has produced east-west striking faults and folds, which bound the Ventura Basin and shape the Santa Clara River drainage (Brownlie and Taylor, 1981). Subsidence of the basin likely ceased ~0.6 Ma (Yeats, 1977), though uplift continues in the Transverse Ranges (Rockwell et al., 1988). Recent work has suggested the potential of large slip along faults in the Transverse Ranges (Hubbard et al., 2014; McAuliffe et al., 2015; Rockwell et al., 2016), and modeling has shown the potential for large tsunamis that may have inundated up to 1 km inland on the coast of the Oxnard Plain (Ryan et al., 2015).

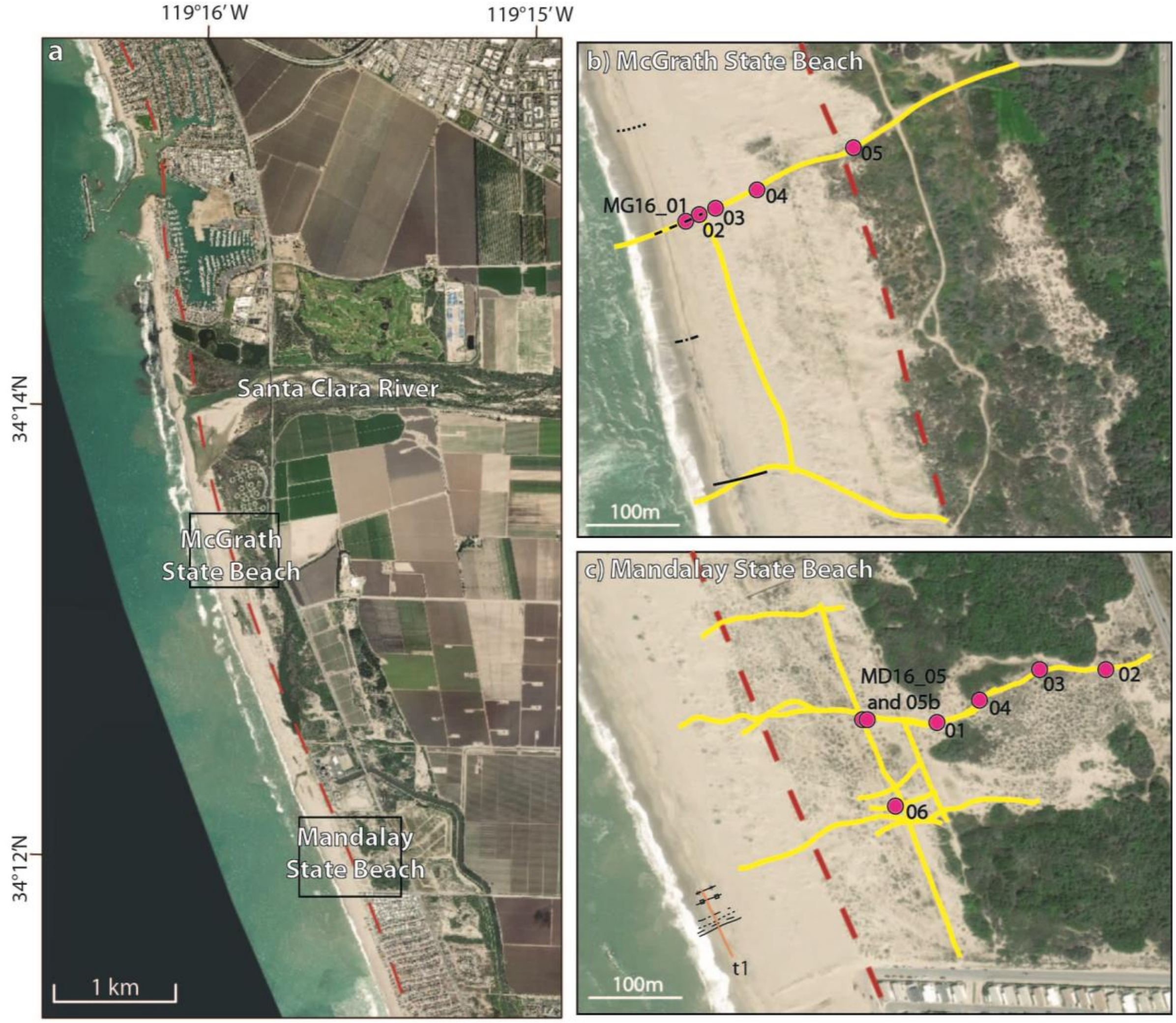

Figure 15. a) Overview of the study area, data collection sites labeled and outlined in black b) McGrath State Beach, and c) Mandalay State Beach. Red dashed line in all panels represents the 1855 shoreline. GPR profiles are shown by the yellow lines in panels b and c. Core locations are shown by pink dots and labeled. GPS profiles of the shoreline are shown by black lines. Transect t1 is shown by the orange line in panel c.

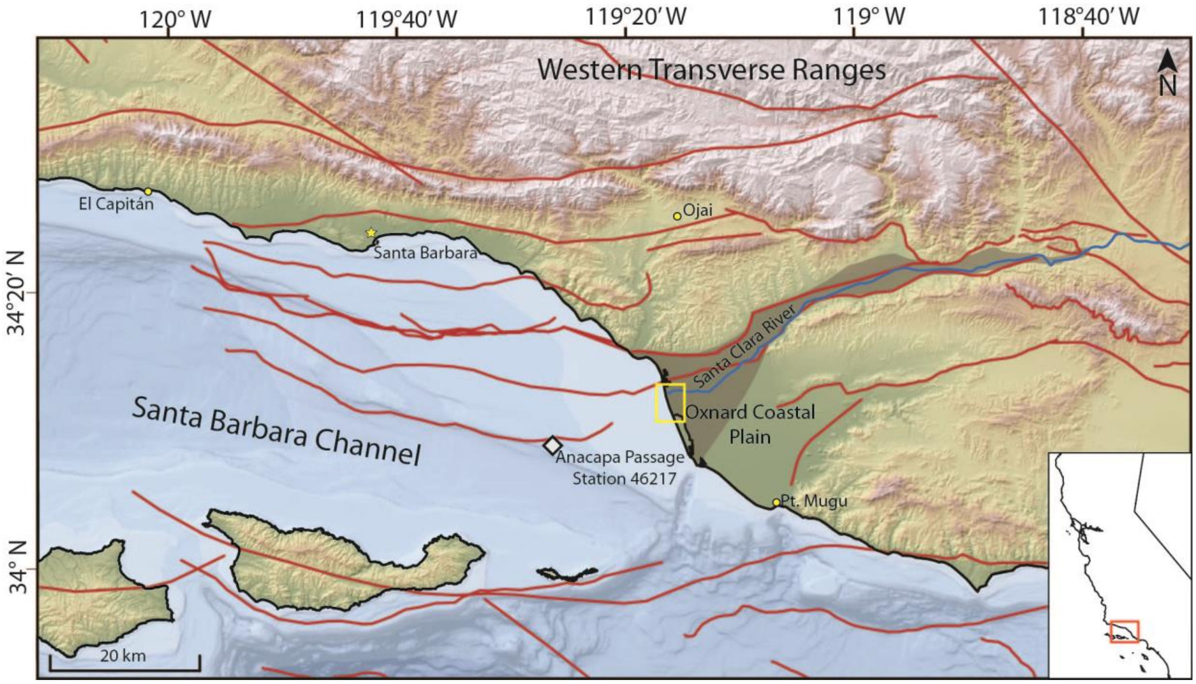

Figure 16. Map showing the area surrounding the Oxnard Plain, and locations mentioned in this study. Red lines show the SCEC Community Fault Model (2017). The Ventura Basin is the shaded region within the Oxnard Coastal Plain. Study area is outlined in yellow.

3.1.1.1 Climate

The Oxnard Plain experiences a Mediterranean climate, with cool, wet winters, and warm dry summers. The majority of the precipitation occurs from November through March but is heavily influenced by ENSO (Andrews et al., 2004). Most significant precipitation episodes in the area occur during El Niño events, which happen every 3-8 years and can last 1-1.5 years (Downs et al., 2013), although atmospheric rivers can also result in unusually high amounts of precipitation at any time during the ENSO cycle (Engstrom, 1996; Reynolds et al., 2018). In addition, the area often experiences 25-30 year periods of alternating wet and dry years influenced by the Pacific Decadal Oscillation (PDO) (Downs et al., 2013; Inman and Jenkins, 1999).

Sediments from the Santa Barbara Basin, as well as records across the western US, indicate the last 600 years were a relatively wet-period within the Holocene, with significant flood layers recorded at 1532 AD, 1761 AD, and 1861 AD (Cook et al., 2004; Du et al., 2018; Hendy et al., 2013; Kirby et al., 2010). However, nearby streamflow reconstructions from Ojai show that intense droughts still occurred, with both a 93- and 23-year cycle between the droughts (Meko et al., 2017). Additionally, many severe storms producing large amounts of precipitation were experienced at the end of the Little Ice Age in the late 19th century (Engstrom, 1994; Reynolds et al., 2018).

Significant wave heights, as measured from the offshore buoy at Anacapa Passage, Station 46217 (ndbc.noaa.gov; last accessed April 29, 2019) (Fig. 15), have a mean of ~1 m. The area experiences semi-diurnal tides, with a great diurnal tide range of 1.645 m (tidesandcurrents.noaa.gov; last accessed March 4, 2019). Beach slopes average 4.6 to 5.7° for the entire Santa Barbara Littoral Cell (Barnard et al., 2009). The beaches from El Capitán to Point Mugu have long term (1855-2006) shoreline change rates of +0.1 ± 0.1 m a^{-1}, and short term rates (1970s-2006) of -0.5 ± 0.4 m a^{-1} (Hapke et al., 2006). South of the Santa Clara River, however, rates of shoreline change from 1987 to 2007 are much higher at +1.7 m a^{-1} (Barnard and Warrick, 2010). The overall progradation of the coastal Oxnard Plain since 1855 is largely controlled by the high sediment yield of the Santa Clara River, which flows through the Oxnard Plain before emptying into the Pacific Ocean.

3.1.1.2 Santa Clara River delta

The largest source of sediment to the Ventura Basin, and the Santa Barbara Littoral Cell, is the Santa Clara River (Warrick and Mertes, 2009). The Santa Clara River drains an area of ~4220 km^2 and has the highest sediment yield of any southern California river, owing to active tectonics, weak sedimentary lithology, and a steep drainage basin, with a headwater elevation at 2900 m (Barnard and Warrick, 2010; Inman and Jenkins, 1999; Warrick and Mertes, 2009). Although 37% of the Santa Clara River is dammed, the dams reduced annual sediment supply by only ~20% (Warrick, 2002). The annual mean sediment yield for the Santa Clara River is ~7 million t a^{-1}; however, discharge on the river is highly episodic, with nearly 75% of the sediment discharged over just 30 days in a 50-year record (Warrick and Milliman, 2003). Discharge is highly influenced by ENSO, with most high discharge events occurring during El Niño years (Downs et al., 2013). The mouth of the Santa Clara River is typically closed, but often breaches during high discharge events (O'Hirok, 1985).

3.2 Methods

Data for this study were collected at McGrath State Beach, 0.5 km south of the mouth of the Santa Clara River, and at Mandalay State Beach ~2 km south of the river mouth, both along the coastal Oxnard Plain (Fig. 15). Several methods were used to document and analyze the beaches and shoreline changes of the coastal Oxnard Plain through time. These include modern beach surveys, subsurface characterization through interpretation of GPR data and sediment cores, and the analysis of aerial photography, satellite imagery, and T-sheets, which are 19th century coastal maps created by the United States Coastal Survey (Grossinger et al., 2011).

3.2.1 GPS Surveys

GPS surveys of the modern beaches were conducted at McGrath State Beach on March 19, 2019 and at Mandalay State Beach on April 20, 2019. GPS data were collected in single-point mode using a TopCon HiPer Lite Plus RTK-GPS system (Fig. 15). GPS data have vertical and horizontal accuracy of ± 3 cm. Elevation data for GPR profiles were collected simultaneously with GPR data.

3.2.2 Ground-penetrating radar

Ground-penetrating radar (GPR) is a geophysical method that uses electromagnetic waves to image different layers in the subsurface. More than 4 km of GPR data were collected at both McGrath and Mandalay State Beaches between 2014 and 2017 (Fig. 15). GPR data were collected in common-offset mode using a hand-towed Sensors & Software pulseEKKO PRO GPR system. Both 200 MHz and 500 MHz transducers were used to penetrate depths of ~1.5 m and obtain vertical resolutions of ~0.03 m and ~0.1 m, respectively. Depth penetration was limited, especially closer to the foreshore, by the presence of saltwater, which has a high dielectric constant that spreads the GPR signal. A common-midpoint survey was collected at McGrath State Beach to obtain a sediment velocity of ~0.174 m/ns, while sediments at Mandalay State Beach have a velocity ~0.10 m/ns based on correlations with cores. Data were processed in Sensors & Software EkkoView Deluxe by applying dewow, automatic gain control (AGC), and bandpass filter. Elevation data were used to topographically correct the GPR data employing a vertical shift of traces in EkkoView Deluxe. GPR profiles, facies and surfaces were interpreted in IHS's Kingdom software using techniques discussed in Neal (2004).

3.2.3 Sediment Cores

Twelve vibracores, ranging from 0.7 m to 1.62 m in length, were collected at both McGrath and Mandalay State Beaches to document environmental changes in the sedimentary record (Fig. 15; Appendix A, Figure 1). The bottom ~30 cm of six cores collected at Mandalay State Beach were cut off, and two cores, MD16_02 and MD16_05b, were dated using optically stimulated luminescence. The remaining part of all cores were split, photographed, and described, noting grain characteristics, sedimentary structures, organic content, and color. Grain-size distributions of modern beach and dune samples from Mandalay State Beach were determined using a CILAS 1190 laser diffraction system and analyzed following the methods of Folk (1957) and Sperazza et al. (2004).

3.2.3.1 Radiocarbon dating

Charcoal, shell fragments, and plant fragments found within the vibracores were radiocarbon dated at DirectAMS and the UC Irvine Keck-CCAMS facility (Table 3). Radiocarbon ages were calibrated in CALIB, using the MARINE13 curve to calibrate shells, and the IntCal13 curve for charcoal and plant fragments (Reimer et al., 2013; Stuiver et al., 2018). Shell fragments were corrected for the marine reservoir effect using a marine reservoir age (ΔR) of 290 ± 35 radiocarbon years (Ingram and Southon, 1996). Shell fragments give a maximum age (earliest date) of deposition because they may have been reworked in the littoral system before deposition.

Table 3. Radiocarbon ages from Mandalay State Beach.

Sample	Lab ID	Sample Type	Depth (cm)	^{14}C Age (yr BP, 1σ error)	ΔR	Calibrated Age (AD, 2σ error)
MD16_03_59	D-AMS 033272	root	59	modern	N/A	modern
MD16_03_59	219848	shell fragment	59	1195 ± 15	289 ± 35	1435 ± 71
MD16_04_57	D-AMS 033275	shell fragment	57	1139 ± 25	290 ± 35	1472 ± 74
MD16_05b_23	D-AMS 033273	charcoal	23	251 ± 26	N/A	1653 ± 21
MD16_05b_34	D-AMS 033276	shell fragment	34	1543 ± 34	290 ± 35	1151 ± 106
MD16_06_91	D-AMS 033274	shell fragment	91	1297 ± 25	290 ± 35	1362 ± 68
MD16_06_92	D-AMS 033271	charcoal	92	723 ± 40	N/A	1276 ± 43

3.2.3.2 Optically Stimulated Luminesce Dating

Optically stimulated luminescence (OSL) dating is a dosimetric technique that measures the time elapsed since the burial of quartz and/or feldspar grains. The bottom ~30 cm of two cores, MD16_05b and MD16_02, were sent to the Geologic Survey of Illinois to undergo OSL dating. Vibracores were collected using 8 cm diameter aluminum tubes, preventing sunlight exposure for sediments within the tubes. A modern sediment sample was collected at the foreshore using an opaque 3 cm diameter tube to penetrate the upper ~20 cm of the subsurface.

All processing of the sediment took place under a subdued orange light environment. Ten centimeters of sediment was removed from both ends of the tube as these grains might have been partially exposed to light during sampling. Sediment from these external portions was used to measure the *in situ* water content and its radioactive content (uranium, thorium, and potassium), both for dose rate calculation. Equivalent doses (D_e) measurements were made on an automated Risø TL-DA-20 system, equipped with a set of blue (470 nm) and infrared (870 nm) LEDs, for light stimulation. Detection was made in the UV (Hoya U340 filter) for quartz.

OSL measurements were carried out using the single-aliquot regenerative (SAR) dose procedure (Appendix A, Table 1) (Murray and Wintle, 2000). Quartz aliquots were rejected because of feldspar contamination (10% threshold limit) or high recuperation (5% limit of the natural luminescence), a low fast-ratio (OSL decay shape) (Durcan and Duller, 2011), or because the luminescence intensity were in distinguishable from the instrumental background (no signal). Best age estimates were provided by the weighted mean age (central age model) and on the present-day dose rate (Appendix A, Figure 2).

3.2.4 Beach Progradation

The locations of past shorelines were used to determine an approximate rate of progradation of the coastal Oxnard Plain. The modern shoreline position was determined using the 2014 USACW NCMP Topobathy LIDAR data (coast.noaa.gov). Two historical T-sheets from 1855 of the Oxnard Plain were used to determine the 1855 AD average high water line shoreline position (Shalowitz, 1964). Finally, radiocarbon and OSL dated sediments from the sediment cores were used to determine approximate shoreline positions prior to 1855 AD.

Aerial photography from the Special Research Collections at the UCSB Library was used to estimate shoreline positions from 1927 AD to 2002 AD and Google Earth satellite imagery was used from 1994 to present (Table 4). Aerial photography was georeferenced in ArcGIS Pro with a minimum of 5 ground control points. The wet/dry line or debris line was observed in the photographs and satellite images to indicate an approximate average high-water line (Shalowitz, 1964). The shoreline position change was measured at one shore-normal transect at McGrath State Beach and a second one at Mandalay State Beach.

Table 4. Aerial Photographs and Satellite Images. N/A indicates the photograph did not exist for that location.

Date	Flight or Source	RMS error (m)	Total Uncertainty (m)	Shoreline Position at McGrath State Beach (m)	Shoreline Position at Mandalay State Beach (m)
11/19/2018	Google		23	212 ± 32	117 ± 32
8/12/2018	Google		23	192 ± 32	102 ± 32
1/12/2018	Google		23	208 ± 32	107 ± 32
1/9/2018	Google		23	213 ± 32	112 ± 32
12/12/2017	Google		23	218 ± 32	112 ± 32
12/11/2017	Google		23	217 ± 32	112 ± 32
12/10/2017	Google		23	217 ± 32	112 ± 32
12/6/2017	Google		23	207 ± 32	107 ± 32
12/4/2017	Google		23	199 ± 32	99 ± 32
4/1/2017	Google		23	208 ± 32	112 ± 32
10/2/2016	Google		23	230 ± 32	108 ± 32
8/28/2016	Google		23	235 ± 32	117 ± 32
7/2/2016	Google		23	226 ± 32	102 ± 32
2/8/2016	Google		23	230 ± 32	102 ± 32
5/1/2015	Google		23	244 ± 32	107 ± 32
8/8/2014	Google		23	248 ± 32	102 ± 32
1/22/2014	Google		23	261 ± 32	122 ± 32
12/9/2013	Google		23	270 ± 32	112 ± 32
8/26/2012	Google		23	290 ± 32	133 ± 32
4/26/2011	Google		23	301 ± 32	142 ± 32
5/24/2009	Google		23	308 ± 32	122 ± 32
9/30/2007	Google		23	318 ± 32	112 ± 32
7/7/2006	Google		23	364 ± 32	103 ± 32
12/31/2005	Google		23	378 ± 32	N/A
6/25/2005	Google		23	402 ± 32	109 ± 32
9/30/2004	Google		23	242 ± 33	109 ± 33
6/13/2002	NAPP-3C	1.36	24.36	258 ± 34	95 ± 34
11/30/1994	PW-VEN-11	0.85	23.85	200 ± 33	N/A
9/3/1994	NAPP-2C	1.22	24.22	206 ± 33	57 ± 33
4/14/1993	California Coastal Records Project	2.18	25.18	170 ± 32	57 ± 32

3/17/1987	California Coastal Records Project	1.39	24.39	208 ± 39	17 ± 39
3/14/1985	WAC-85CA	8.96	31.96	262 ± 40	26 ± 40
3/21/1982	NOS-82-BC	2.18	25.18	184 ± 38	30 ± 38
4/14/1980	LN8-RN1-8073	6.03	29.03	149 ± 38	22 ± 38
4/3/1979	79-028-02711	2.38	25.38	134 ± 37	15 ± 37
9/21/1978	USDA-40-06111	3.98	26.98	133 ± 42	5 ± 36
6/16/1978	PW-VEN-2	9.39	32.39	130 ± 40	N/A
2/14/1977	TG-7700	1.76	24.76	141 ± 34	15 ± 34
7/29/1975	TG-7500	1.07	24.07	125 ± 34	6 ± 38
5/26/1973	NASA-JSC-259-SITE-254-FLT-29-R-102	2.03	25.03	155 ± 39	N/A
12/10/1970	HB-RT	7.27	30.27	103 ± 39	22 ± 41
2/26/1969	HB-OM	2.11	25.11	94 ± 37	N/A
7/5/1966	HB-IA	4.81	27.81	98 ± 42	25 ± 42
6/9/1965	AXI-1965	9.24	32.24	110 ± 44	30 ± 44
2/12/1964	HA-WE	7.7	30.7	101 ± 46	23 ± 46
3/20/1963	HA-SH	11.63	34.63	138 ± 57	48 ± 57
1/7/1963	HA-RR	23.05	46.05	116 ± 69	46 ± 69
3/24/1962	HA-OH	28.41	51.41	104 ± 66	20 ± 61
4/10/1958	HA-CT	19.65	42.65	110 ± 53	N/A
12/13/1952	AXI-1952	9.62	32.62	133 ± 54	40 ± 54
8/5/1947	GS-EM	20.53	43.53	155 ± 62	62 ± 51
4/22/1941	C-7046	21.38	44.38	112 ± 52	N/A
1/26/1934	C-2902	5.35	28.35	104 ± 39	62 ± 39
6/1/1929	C-563	4.26	27.26	111 ± 40	56 ± 40
1927	C-104	6.68	29.68	134 ± 42	58 ± 42
1855	T-Sheet	8	31	0 ± 31	0 ± 31

3.2.4.1 Shoreline Position Uncertainty

The natural variability of the shoreline temporally and laterally, caused by changing tides, migrating bars, and seasonal beach recovery, introduces inherent uncertainty into shoreline position estimates (Ruggiero et al., 2003). One way to determine uncertainty is to calculate the range of extreme wave run-up during a season, as it serves as a useful proxy for the average high water line (Ruggiero et al., 2003). The 2% exceedance value of run-up (R_2) was calculated using the equation

$$R_2 = 1.1\left(0.35\beta_f(H_0L_0)^{1/2} + \frac{\left[H_0L_0\left(0.563\beta_f^2+0.004\right)\right]^{1/2}}{2}\right) \qquad (1)$$

where β_f is the slope of the foreshore as determined from GPS surveys, H_0 is offshore significant wave height and L_0 is offshore significant wave length as determined from the buoy at Anacapa Passage (ndbc.noaa.gov; last accessed April 29, 2019) (Stockdon et al., 2006). Uncertainty for shoreline positions from aerial photographs, satellite imagery, and T-sheets due to natural variability, x, was estimated using the equation

$$x = \frac{range(R_2)}{\tan\beta_f} \qquad (2).$$

Georeferencing also introduces error into aerial photographs positions, and the root mean square error for ground control points for each photo was added to the natural variability to determine total uncertainty for aerial photographs (Table 4).

Beach sediments from cores may have been deposited at any elevation within the tidal range of the beach. Therefore, the uncertainty for shoreline position taken from radiocarbon and OSL dated sediments is estimated as the great diurnal tide range divided by the tangent of the slope of the foreshore. This uncertainty was reduced by using the landward limit of GPR reflections to limit the possible landward range of the shoreline. Reduction on the seaward side was not possible due to the limited depth penetration of the GPR.

3.2.4.2 Progradation Rate

The progradation rate of the beaches was determined using a Monte Carlo simulation to account for the uncertainty in both ages and distances between shorelines. Progradation rate (r) was calculated using the equation

$$r = \frac{d}{t} \qquad (3),$$

where d is the distance between two shoreline positions, chosen as a uniform random number within the possible range of distances between the two shorelines due to shoreline position uncertainty, and t is the difference in time between the two shoreline positions, chosen from a Gaussian PDF when the date of the shoreline is from radiocarbon or OSL ages, or as the given age for the T-sheet shoreline at 1855, and the modern position in 2014.

3.4 Results

Overall, the coastal Oxnard Plain has experienced relatively constant depositional conditions over the last ~600 years, with the modern environment having similar characteristics to the GPR profiles and sediment cores. Progradation of the beach, on centennial timescales, remained relatively constant through time. However, variations in progradation were observed over decadal timescales.

3.4.1 Modern Beach Surveys

Modern beach slopes at McGrath State Beach range from ~7.3° to 9.5°, while slopes at Mandalay State Beach range from ~4.9° to 6.6° (Fig. 17). Shore parallel transects from Mandalay State Beach record the morphology of beach cusps (Figure 18). Theses beach cusps have a width of ~50 m and height of ~0.8 m, from the top of the cusp to the base of the middle of the cusp.

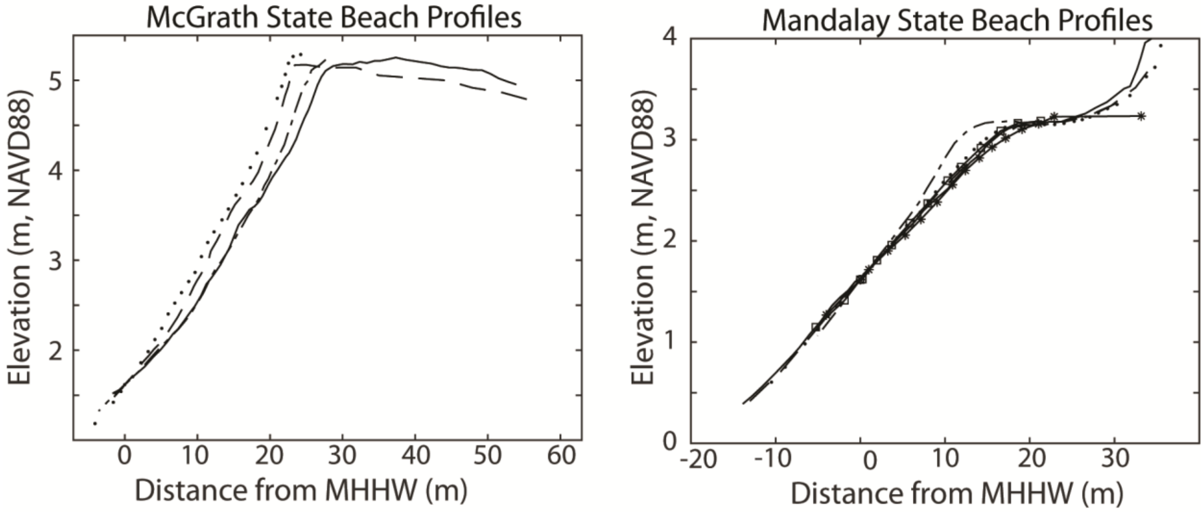

Figure 17. GPS shore-normal profiles from McGrath and Mandalay State Beaches. Location of profiles shown by corresponding line type (e.g. dashed, stippled) in Fig. 15.

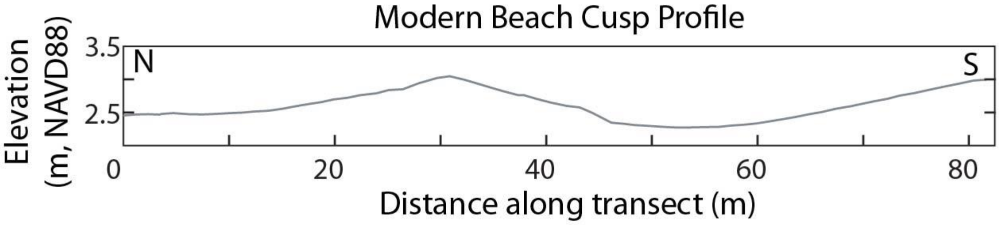

Figure 18. Profile of shore-parallel GPS beach transect t1, on Mandalay State Beach, showing morphology of a beach cusp. Vertical exaggeration is 6X. Location shown in Fig. 15.

3.4.2 Sediment Facies

The modern beach sediments sampled from the upper foreshore at Mandalay State Beach are moderately well-sorted, coarse skewed, medium sands, with a mean grain size of 1.27 φ. The modern aeolian sands are also moderately well-sorted, coarse-skewed, medium sands, with a mean grain size of 1.34 φ. The standard deviation of both sands indicates that the aeolian sediments are slightly better sorted than the modern beach sediments (0.58 versus 0.71 for the beach).

McGrath State Beach sediment cores all contained medium to coarse grained, moderately sorted sands (Fig. 19). Within the Mandalay State Beach sediment cores, three facies were based on similarity to modern grain sediments with similar characteristics as well as observations of grain color and vegetation content (Fig. 19). Two aeolian facies were defined, one with vegetation reworking and the other without. Both facies have moderately well-sorted, medium grained sands. The vegetated aeolian facies has a brown color and often contains roots. The non-vegetated aeolian facies is pale yellow in color and lacks the presence of roots. The third facies is the beach facies. This facies contains slightly less sorted (though still moderately well-sorted) sands than the aeolian facies, slightly larger grains, though still medium sands, and is also pale yellow in color. The beach sands also often contain heavy-mineral layers, which have previously been interpreted in beach sands as storm deposits (Buynevich and FitzGerald, 2001; Moore et al., 2004). The minor differences in the sediments from both the modern environment and the sediment cores make them useful guides of past depositional environments, but interpretations were mainly based on radar facies and surfaces.

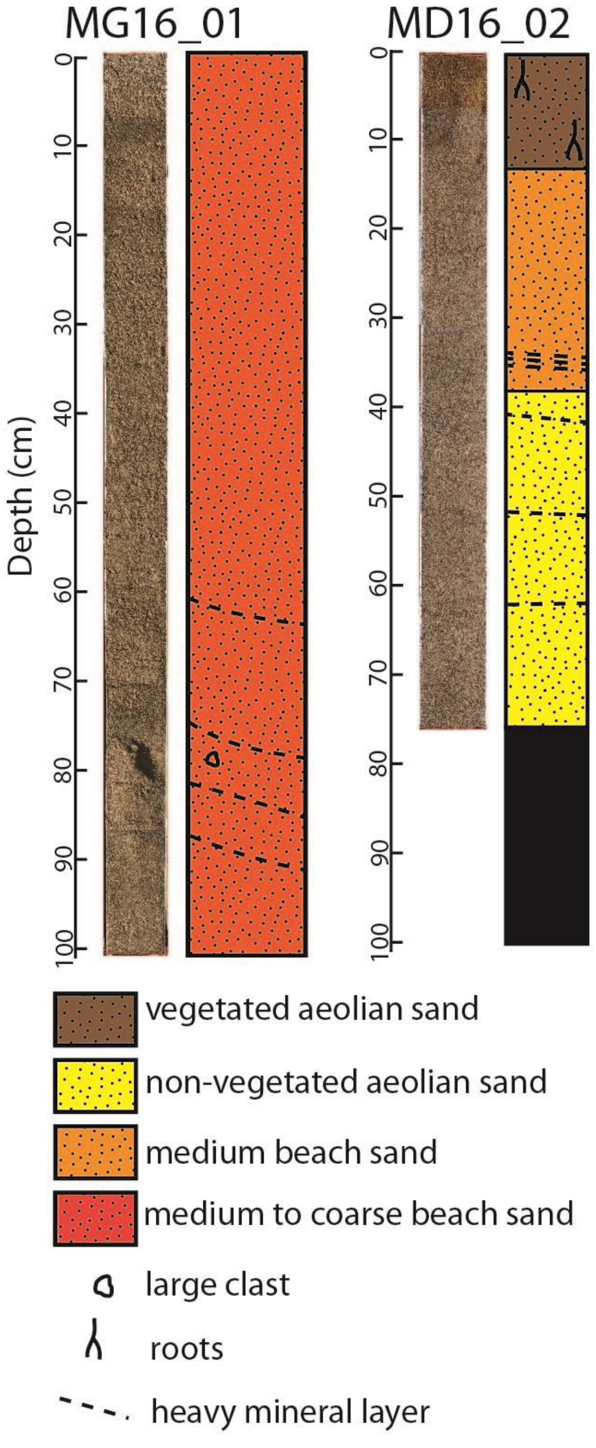

Figure 19. Sediment cores and core logs. Locations shown in Figure 15. Black filled box at bottom of MD16_02 was sediment removed for OSL dating.

3.4.3 Radar Facies and Surfaces

Three radar facies were identified within the GPR profiles from McGrath and Mandalay State Beaches based on reflection configuration, dip direction, and continuity (Neal, 2004). In shore-normal GPR profiles, radar facies f1 is characterized by planar, ~5 to 7° seaward-dipping, mostly parallel and continuous reflections (Figs 20 and 21). Within this radar facies, sediment cores contain beach sands and heavy mineral layers. The second radar facies, f2, is characterized by shallowly, 3°, seaward-dipping to flat, planar, parallel, continuous reflections (Fig. 20). In shore parallel GPR profiles, these two radar facies, f1 and f2, are indistinguishable based on GPR profile crossings, both having wavy, parallel to sub-parallel, continuous reflections (Fig. 22). The last facies, f3, has chaotic reflections as well as flatter, sinuous, discontinuous reflections (Figs 20 and 21). This facies appears most often within of modern dunes.

Two distinct radar surfaces were identified based on their upper and lower boundary reflection geometries in shore normal GPR profiles. Radar surface type A is a steeply dipping truncation surface that truncates older reflections of radar facies f1, and occasionally f2, that lie below and landward of the surface, and often overlying reflections onlap it (Figs 20 and 21). Radar surface type B is characterized by a shallowly seaward dipping to flat truncation surface that truncates reflections of radar facies f1 below it, and/or radar facies f1 and f2 reflections above it are concordant or onlap onto it (Figs 20 and 21). In shore-parallel profiles, radar surface B is a relatively horizontal surface that truncates deeper reflections and has concordant reflections overlying it (Fig. 22). Radar surface A correlates to two types of truncation surfaces in shore-parallel profiles: a horizontal surface similar to surface B, and a curved, concave up surface, that truncates reflections below it, with concordant or onlapping reflections above (Fig. 22).

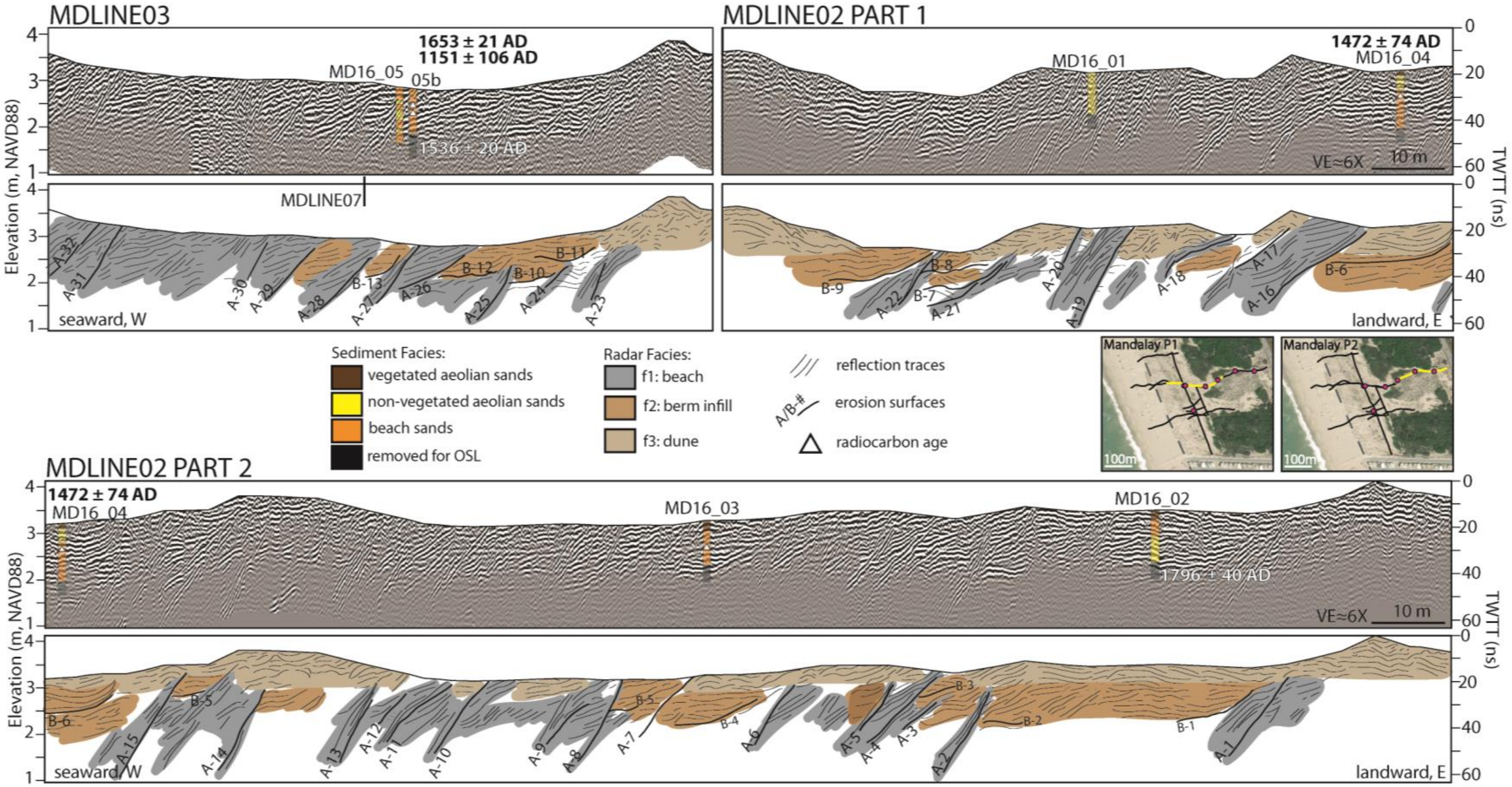

Figure 20. Shore-normal profile of 500 MHz GPR from Mandalay State Beach. Top panel shows the GPS reflections, and bottom panel shows traces of GPR reflections. Yellow line on inset map shows location of GPR along transect. VE=vertical exaggeration. TWTT=two-way travel time.

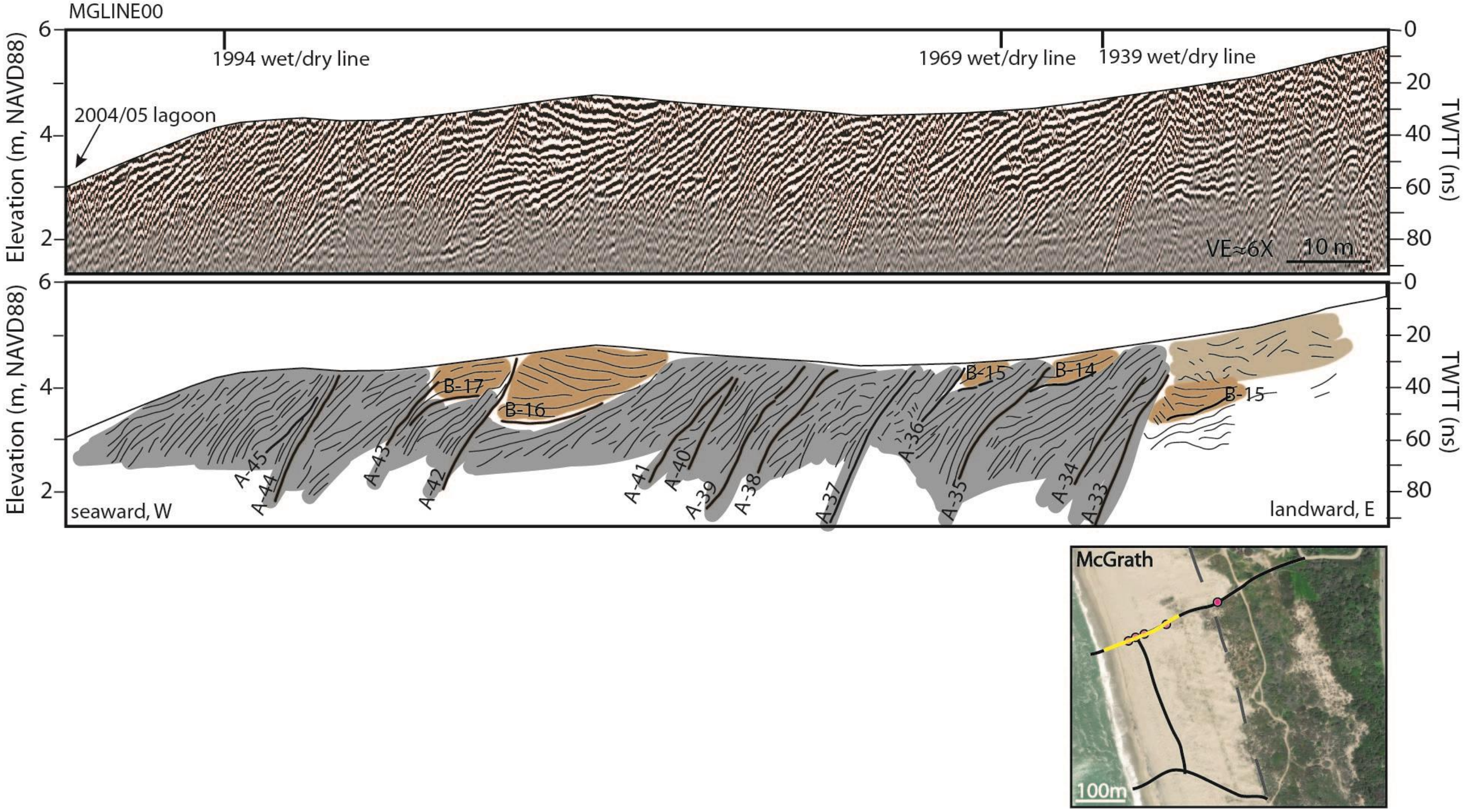

Figure 21. Shore-normal 500 MHz GPR profile from McGrath State Beach. Top panel shows the GPS reflections, and bottom panel shows traces of GPR reflections. Yellow line on inset map shows location of GPR along transect. VE=vertical exaggeration. TWTT=two-way travel time in nanoseconds. Dates and lines along the top panel indicate possible shoreline locations from aerial photographs. See Fig. 20 for interpretation key.

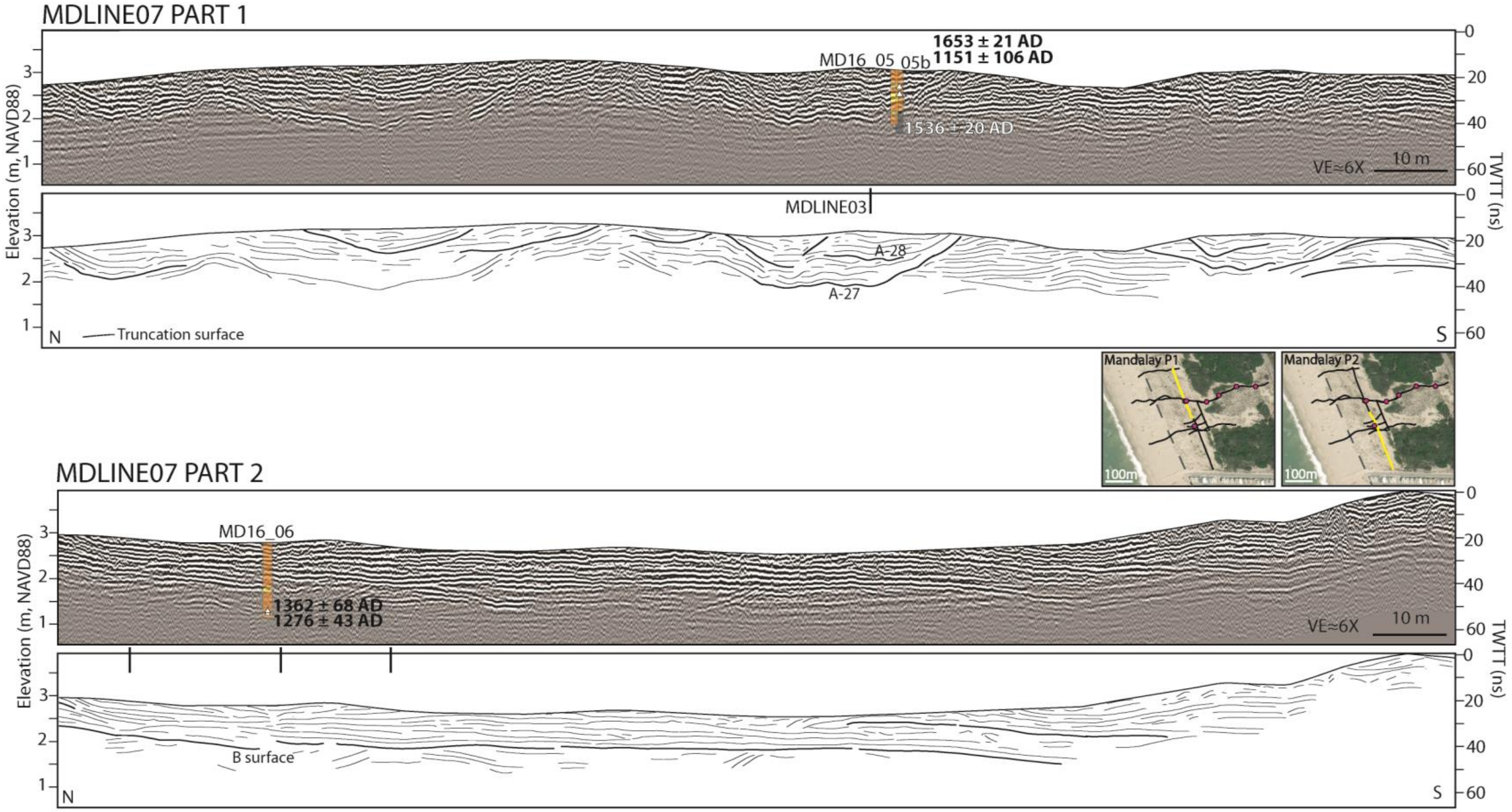

Figure 22. Shore-parallel 500 MHz GPR from Mandalay State Beach. Top panel shows the GPS reflections, and bottom panel shows traces of GPR reflections. Black lines along the top of the second panel indicate GPR line crossings. Yellow line on inset map shows location of GPR along transect. MD16_05 andMD16_05b are projected from 4 m landward onto MDLINE07. VE=vertical exaggeration. TWTT=two-way travel time in nanoseconds. See Fig. 20 for interpretation key.

3.4.3.1 Radar Facies and Surfaces Interpretation

Radar facies f1 is interpreted to represent deposits from a prograding beach, similar to seaward-dipping reflections in other coastal settings (Bristow and Pucillo, 2006; Buynevich and FitzGerald, 2001; Van Heteren et al., 1998). Cores sampling radar facies f2 contain a mix of non-vegetated aeolian and beach sediment facies. This radar facies is interpreted to represent the infilling behind a berm, which could be the result of over wash from the beach as suggested by Neal et al. (2002) for beaches on the coast of England, but likely also includes a component of aeolian infilling as suggested by the sediment cores. Radar facies f3 is interpreted to represent aeolian deposits.

Radar surface type A is interpreted to represent erosion due to high-energy storm waves (Buynevich et al., 2004; Buynevich et al., 2007; Neal et al., 2002). High energy storms can also plane off the tops of berms, and result in the formation of radar surface type B (Neal et al., 2002).

3.4.4 Shoreline Position Ages and Uncertainty

A radiocarbon age on a shell fragment from core MG16_03 of 1435 ± 17 AD suggest the shoreline at Mandalay State Beach has prograded ~450 m over the last ~580 years. A ^{14}C age from core MG16_04 returned an age of 1472 ± 74 AD. Two ages from MG16_05b returned a charcoal age of 1653 ± 21 AD and a shell fragment age of 1151 ± 106 AD. The shell fragment may have been reworked in the offshore system for years, therefore, the age of the charcoal is taken as the age of the shoreline position, and the shell is taken as a maximum limiting age. The deeper sediment from below a type A truncation surface in MD16_05b dates to 1536 ± 60 AD according to OSL dating (Appendix A, Figure 2). A shell fragment from MG16_06 has a date of 1362 ± 68 AD, and a charcoal sample has an age of 1276 ± 43

AD. While these dates are within error, they are both older than the ages of the same position from the modern shoreline. Therefore, they are interpreted as reworked by fluvial and/or offshore processes and thus represent limiting data - the earliest ages of possible deposition. Additionally, ^{14}C age from roots in core MD16_03 resulted in a modern age, and likely represent the subsurface penetration of modern roots into the sand. An OSL age indicates the sediment from MD16_02 dates to 1796 ± 40 AD (Appendix A, Figure 2).

The uncertainty of the 1855 shoreline position (eq. 2) was estimated to be ~23 m, based on an R_2 (eq. 1) of ~2 m. Aerial photographs likely have a similar uncertainty of ~23 m, but also include error due to georeferencing, given as the RMS error between ground control points. Uncertainty associated with assigning the shoreline position of the coast at the time of sand deposition within the sediment cores was estimated to be as large as ~20 m but was reduced to 7 m on the landward side of GPR reflections at the core location as described in the methods (Fig. 20).

3.4.5 Beach changes through time

The T-sheet, aerial photographs and satellite imagery from Google^{TM} show that the shoreline has experienced episodes of growth, erosion, and stability (Fig. 23; Table 4), with overall growth since the oldest mapped shoreline in 1855. At McGrath State Beach the shoreline has prograded 212 ± 32 m since 1855, and at Mandalay State Beach it has prograded 117 ± 32 m. The largest episode of growth at McGrath State Beach of 160 ± 32 m occurred between September 30, 2004 and June 25, 2005, but erosion removed 170 ± 32 m of beach from June 25, 2005 to December 4, 2017. Other large episodes of progradation occurred between March 21, 1982 to March 14, 1985 (78 ± 40 m), November 30, 1994 to

June 13, 2002 (58 ± 34 m), and December 10, 1970 to May 26, 1973 (52 ± 39 m). Smaller episodes of growth and erosion were recorded at Mandalay State Beach (Fig. 23).

To determine the long-term rate of shoreline change at Mandalay State Beach where radiocarbon and OSL ages date to 1435 AD, the data was divided into three ~150-200-year time bins: 1435 AD to 1653 AD, 1653 AD to 1855 AD, and 1855 AD to 2014 AD. The calculated rates of shoreline change are 0.7 – 1.4 m a^{-1}, 0.3 – 0.7 m a^{-1}, and 0.6 – 0.9 m a^{-1}, respectively, with ranges accounting for 95% of the possible progradation rate outcomes from the Monte Carlo simulation. These are within an order of magnitude of beach progradation rate estimates for the larger area surrounding the Santa Clara River (Barnard and Warrick, 2010; Hapke et al., 2006). The data was also divided into two smaller multi-decadal time bins: 1435 to 1472 AD and 1472 to 1536 AD. Progradation rates range from 0.6 – 21 m a^{-1}, and 0.8 to 17 m a^{-1}, respectively. These fall within the range of long-term progradation estimates, while the upper limit is similar to the rapid progradation observed at McGrath State Beach that occurred in the years following a high discharge event on the Santa Clara River (Barnard and Warrick, 2010).

Radar surfaces A and B, interpreted to be erosional surfaces from waves, were counted to understand changing wave climate conditions, or preservation through time (Figures 20 and 21, Table 5). Erosional surfaces were divided into time bins based on dates in all the cores: 1432-1472 AD, 1472 to 1535 AD, 1653 to 1855 AD, and 1855 to 2014 AD. Data from 1653 to 1855 AD is obscured beneath a dune deposits and therefore is a minimum estimate. Additionally, saltwater prevented imaging of the foreshore at Mandalay Beach, so erosion surfaces were counted at McGrath State Beach closer to the Santa Clara River for 1855 to 2014 AD. The maximum density of type A erosional surfaces preserved was recorded from 1435 to 1472 with a periodicity of 1 surface preserved every 3 years, and the maximum density of type B surfaces was recorded from 1472 to 1536 with 1 surface preserved every 9 years. The minimum density of erosional surfaces was recorded from 1653 to 1855 with 1 type A surface preserved every 34 years, and 1 type B preserved every 202 years. Aerial imagery estimates of the shoreline indicate that the area imaged at McGrath State Beach may only date from 1939 to 2004 (Fig. 21), which would equate to 1 type A surface preserved per 5 years and 1 type B surface preserved every 14 years.

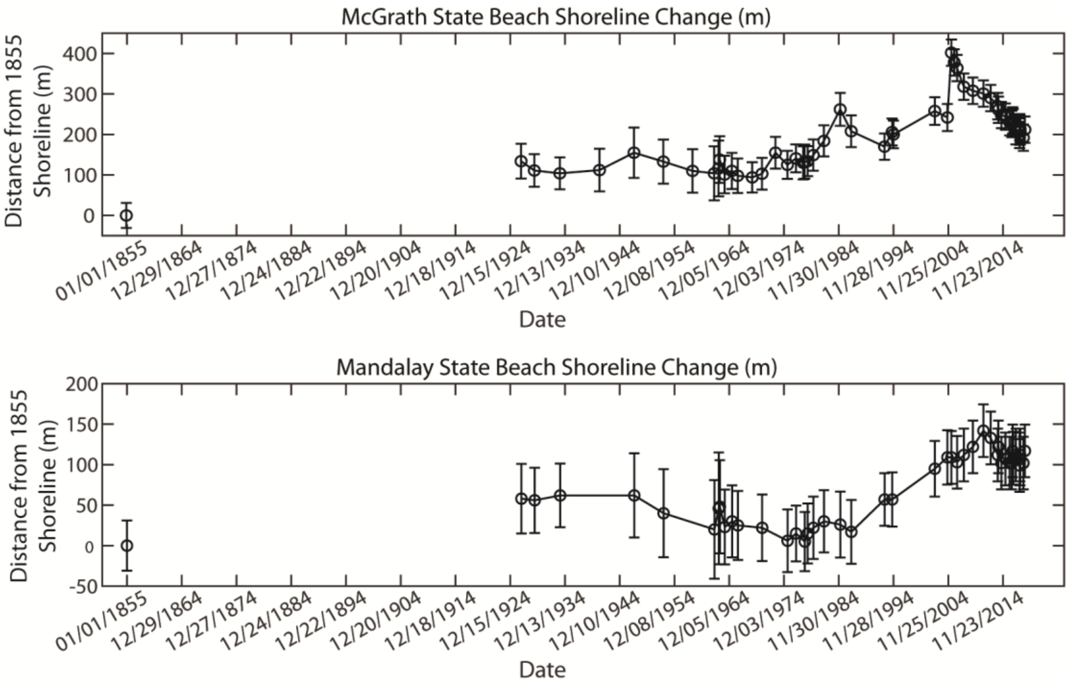
McGrath State Beach Shoreline Change (m)

Mandalay State Beach Shoreline Change (m)

Figure 23. Shoreline position change through time at McGrath and Mandalay State Beaches. Note that McGrath and Mandalay State Beaches have different y axis limits.

Table 5. Preservation through time.

Time Bin	Type A Surface	Type A Surface Periodicity (yrs per surface)	Type B Surfaces	Type B Surface Periodicity (yrs per surface)
Pre-1434	6	N/A	4	N/A
1434-1472	9	4	3	12
1472-1536	11	6	6	11
1653-1855	6	34	1	202
1934-2004	13	5	5	14

3.5 Discussion

The relatively constant progradation of the coastal Oxnard Plain on centennial timescales suggests that centennial-scale climate changes have had no significant influence on beach progradation over the last ~600 years, in agreement with its impact on other systems in southern California (Kirby et al., 2010; Du et al., 2018). The following section further discusses how the signature of beach progradation is preserved at McGrath and Mandalay State Beaches. Additionally, the relationship between erosion, tectonics, and progradation of the coastal Oxnard Plain through time is discussed.

3.5.1 GPR Interpretation

The GPR radar facies, f1 and f2, and surfaces A and B, form cut and fill structures that are typical of areas experiencing periods of beach accretion and erosion (Fig. 24) (Bristow and Pucillo, 2006; Tamura et al., 2008). At McGrath State Beach, radar facies f2 may represent an infilling of a trough due to over wash on top of a large sand bar, rather than a berm. Sand bars are known to form offshore of the Santa Clara River delta during large flood events (Barnard and Warrick, 2010).

The much younger OSL age of the landward sediments at MD16_02 is likely the result of trough infilling that occurred after the shoreline prograded. Based on the approximate median progradation rate as indicated by other data presented in this study of ~0.7 m a^{-1}, the approximate age of the shoreline at MD16_02, ~140 m landward of MD16_04, should be ~1227 AD. Relative sea-level during this time would be ~0.6 m lower than present day, based on a rate of RSL rise of 0.8 mm a^{-1} (Reynolds and Simms, 2015), therefore the upper 0.6 m of sediments may not be beach sediments, but could be aeolian. An aeolian sediment source is supported by the 1855 T-sheet, which displays dune deposits over the location of core

MD16_02. If the OSL age is accurate, this suggests that some troughs formed behind berms could persist for hundreds of years before infilling completely.

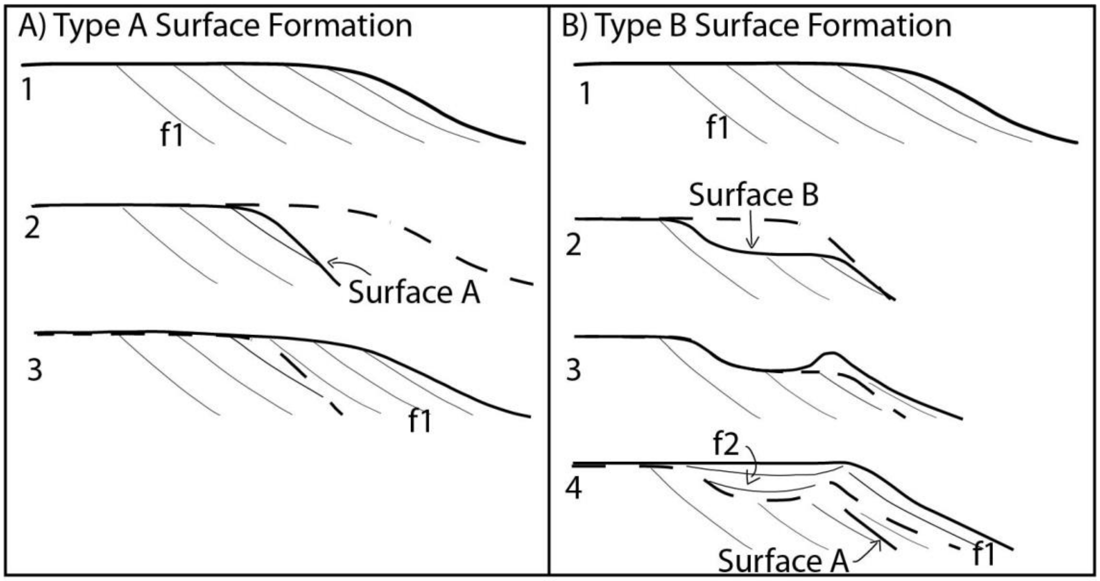

Figure 24. Coastal Oxnard Plain progradation characteristics. Bold line shows the shoreline in each step, dashed line shows the shoreline from the previous step. A) Formation of surface A, 1. normal beach progradation (radar facies f1), 2. High-energy waves cause erosion form surface A, 3. progradation continues. B) Formation of surface B, 1. normal beach progradation (radar facies f1), 2. High-energy waves cause erosion of the foreshore, and plane off the top of the backshore creating surface B, 3. Berm builds at the edge of the new foreshore, 4. Over wash and aeolian sediments fill in behind the berm depositing radar facies f2 and progradation continues.

3.5.1.1 Shore-parallel beach progradation

The progradation of beaches is often only observed in shore-normal profiles rather than shore parallel profiles. When imaged, beach progradation has left behind horizontal, parallel continuous reflections (Neal et al., 2002). Shore parallel GPR profiles from McGrath and Mandalay State Beaches show similar characteristics. However, the profile from Mandalay State Beach also includes concave-up truncation surfaces (Fig. 22). These surfaces look strikingly similar to small paleo-inlets and storm-scoured channels imaged on transgressive barriers (FitzGerald et al., 2001; Garrison et al., 2010). While the shore-normal profile MDLINE03, at its crossing with shore parallel profile MDLINE07, indicates that the truncation surfaces (A-27 and A-28) were formed by high-energy wave erosion, it does not support extensive erosion beyond a few 10s of meters from the foreshore as might be expected for a tidal inlet, and has been imaged for channel scour on North Padre Island, TX (Garrison et al., 2010). In addition, historic maps and aerial photographs do not support the presence of a lagoon at Mandalay State Beach. The modern beach in this area displays prominent beach cusps that have elevation differences on the order of 1 m from the crest of the cusp to the trough. Beach cusps typically form after storms (Holland, 1998). This matches the morphology of the concave-up surfaces within the GPR profiles, thus are thought to be the signature of beach cusps (Figs 19 and 22). Large flood events that occur on the Santa Clara River have the potential to bring enough sediment to deposit quickly and preserve the morphology of the beach cusps in the sedimentary record. Therefore, GPR profiles must be put into a 3-D context to accurately interpret depositional environments and processes.

3.5.2 Progradation and erosion through time

When beaches are supplied with enough sediment, progradation occurs as long as accommodation is available. If the sediment supply is reduced, or cannot keep pace with sea-level rise, erosion will occur (Bruun, 1962). Ongoing sea-level rise for southern California has been estimated to be ~0.8 mm a^{-1} (Reynolds and Simms, 2015), with a magnitude of rise of ~0.44 m over the last 550 years. However, the coast has continued to prograde through this time indicating that either sediment supply has outpaced relative sea-level rise, or the area has undergone uplift. Although the fault geometry in the area is still controversial, most models would suggest the Oxnard Plain would subside if faults from either side of the basin ruptured (Nicholson et al., 2015; Plesch et al., 2007). Therefore, it is more likely that sediment supply has outpaced the rise in sea-level.

On centennial timescales, progradation rates do not exhibit large changes, suggesting that centennial-scale shifts in climate (e.g. Little Ice Age, Medieval Warm Period) did not have a significant effect on beach progradation during the last 600 years. While the climate of SW California has been relatively wet over the last 500 years (Du et al., 2018), the region has experienced shorter decadal to multidecadal cycles of wet and dry years linked to ENSO and PDO (Downs et al., 2013; Meko et al., 2017). During wet years, the Santa Clara River has a much higher sediment yield and several studies have noted that sediment added to the Santa Barbara Basin is highly episodic (Barnard and Warrick, 2010; Inman and Jenkins, 1999). Modern studies of the Santa Clara River reflect these episodic high discharge events, and have related them to progradation at the river mouth (Barnard and Warrick, 2010; O'Hirok, 1985). Specifically, Barnard and Warrick (2010) found that after the 2004-05 floods, rates of progradation downdrift of the Santa Clara River increased to rates of as much as 19 m a^{-1} in the three years following the event. Satellite imagery captured the 04-05 progradation, and aerial photographs show similar periods of progradation of from 70-73, 82-85, and 94-2002 (Fig. 23), which all coincide with years of high sediment yields from the Santa Clara River (Warrick, 2002). Additionally, the progradation rates on multi-decadal timescales show the potential for high rates possibly caused by large floods on the Santa Clara River.

Long droughts can erode much of the sediment deposited on the beach in previous years. For example, Griggs et al. (2005) found that extended drought from 1948-1959 AD resulted in nearly 90 m (300 ft) of beach erosion along the northern coast of the Oxnard Plain. Aerial photograph-based estimates of erosion from August 5, 1947 to April 10, 1962 were similar with ~52 ± 64 m of erosion measured. This equates to ~120 years of progradation lost if beach growth was constant at 0.7 m a^{-1}, the median rate from 1855 to 2014; or only 5 years of progradation with beach progradation rates of 19 m a^{-1}. However, 90 m of erosion after 1948 AD would place the 1959 AD landward of the 1855 shoreline, which aerial photographs do not support (Fig. 25b). Therefore, progradation must also occur at higher rates on shorter time scales to account for later erosion.

Drier periods have the potential to remove several years of the record, such as erosion of ~57 m of the beach from 1934 AD to 1978 AD (Fig. 25). During the driest period (1569 to 1682 AD) in the precipitation reconstruction from nearby Ojai (Meko et al., 2017), sediment core MD16_05b records a ~117-year gap in the beach record from 1536 AD to 1653 AD, for sediment below and above the erosional surface A-26 (Fig. 20). Thus, although the beaches show relatively consistent progradation on centennial (*i.e.* 150- to 200-year) time scales, the sediments are likely only recording a series of short episodic progradation events. The GPR character imaged here is therefore reflective of longer erosive periods caused by prolonged droughts with short periods of progradation. This contrasts with studies in depositional environments that have constant sediment supply that interpret similar GPR character as long-term progradation punctuated by short-term erosion events (Buynevich and FitzGerald, 2001).

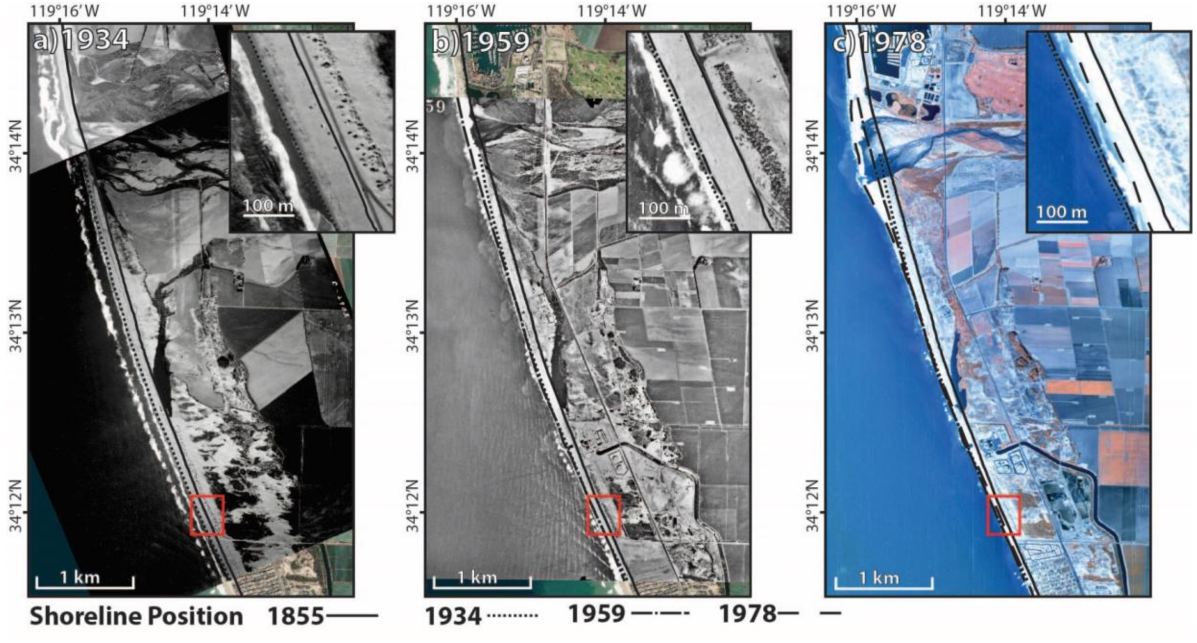

Figure 25. Aerial photographs from 1934, 1959, and 1978 with the current 2018 ArcGIS base map in the background. Red box is location of inset map.

The obscuration of the GPR data by large dunes, different locations along the Oxnard Plain, and limited resolution obtained by dating make it difficult to accurately compare erosion surface frequency between time intervals. However, where erosion surfaces were imaged well enough to be counted through a time period, they appear to reflect relatively constant frequency of erosion through time. This consistent frequency may reflect the relatively regular return of periods of El Niño and PDO oscillations. Nevertheless, the preservation of erosion surfaces is largely dependent on 1) how much erosion is caused during prolonged droughts, potentially removing the signal of earlier erosional surfaces and 2) whether erosion is followed quickly by progradation of the coast, as is more likely to occur closer to the Santa Clara River delta.

Without higher temporal resolution on the sediments, it is difficult to assess the recurrence interval of large storms, droughts and the exact periods of punctuated progradation. However, if the sediment yield of the Santa Clara River is reduced in the future due to prolonged droughts, while sea-level rise continues and/or accelerates, it is likely to result in large amounts of erosion to the coast.

3.5.2.1 Links to Human Activity

Several studies have shown that fine-grained sedimentation rate increased in the late 18th century due to land-use changes associated with European settlement of southern California (Anderson et al., 2015; Cole and Liu, 1994; Ejarque et al., 2015). However, no increase in progradation south of the Oxnard Plain is recorded from 1623 AD onward. The relatively uniform progradation rates may suggest that fine grains were preferentially mobilized during European settlement, which began with ranching and cattle grazing (Downs et al., 2013), or the signature of an increase in sand supply bypassed the littoral zone into the ultimate sand sinks of the California coast – the deep-water realm. In this case, fine grains would likely be suspended and deposited into the basin rather than preserved on the beaches that contain predominately medium sized sediment grains.

3.5.3 Tectonics recorded by sedimentation?

Erosional surfaces caused by tsunamis have an undulatory nature (MacInnes et al., 2009; Meilianda et al., 2010) and have been imaged in other prograding beach settings (Simms et al., 2017). However, although modeling studies suggest that a large tsunami could occur along the coastal Oxnard Plain (Ryan et al., 2015), no erosional surfaces on the scale of those imaged by Simms et al. (2017) or MacInnes et al. (2009), or with an undulatory nature, are preserved within the top 1.5 m of the coastal Oxnard Plain. Furthermore, the relatively constant rate of progradation suggests no substantial influence of tectonic activity to cause sudden growth or erosion of the shoreline. This suggests that no tsunami or neo-tectonic activity has had a significant impact on the coastal Oxnard Plain over the last 600 years. However, earlier events could be recorded either more landward in the Oxnard Plain or deeper within the sedimentary record, which were not imaged within the GPR data.

3.6 Conclusions

The coastal Oxnard Plain south of the Santa Clara River has prograded on centennial (150 to 200-year) timescales at rates of 0.3 to 1.4 m a^{-1} over the last 600 years. However, on decadal timescales progradation is episodic, experiencing large episodes of progradation predominately after wet years. Droughts and high-energy wave events on the coastal Oxnard Plain have the potential to erode up to 90 m of the shoreline, equivalent to 5 to 120 years of the sediment record. In the future, the coast may undergo increased erosion if more prolonged droughts occur.

The first imaging of beach cusps in the GPR record encourages the need to interpret GPR profiles in 3-D. Although the area is tectonically active, no record of large tsunamis is recorded within the last 600 years, nor episodes of sudden growth or erosion of the shoreline caused by tectonic uplift or subsidence.

CHAPTER 4

4. Late Holocene ice mass changes recorded in a relative sea-level record from Joinville Island, Antarctica

4.1 Introduction

In 2002, the Larsen B ice shelf on the eastern Antarctic Peninsula (AP) collapsed, initiating accelerated ice flow and glacial thinning in the glaciers it once buttressed (Rignot et al., 2004; Scambos et al., 2004). The subsequent terrestrial ice-mass loss from the glaciers that once fed the ice shelf resulted in a pronounced increase in uplift rates recorded in GPS data across the AP (Thomas et al., 2011). The amount of uplift exceeded that which could be explained by elastic deformation of the solid Earth alone and must have included a viscoelastic response (Nield et al., 2014). Most current continental-scale glacial isostatic adjustment (GIA) models (Lambeck et al., 1998; Peltier et al., 2015) for the behavior of the Earth in response to late Pleistocene through late Holocene ice-sheet changes fail to reflect rapid decadal to centennial Earth responses to ice-mass loss. This shortcoming is in part a reflection of the relatively limited resolution of the relative sea-level (RSL) data available within Antarctica. While geologic evidence shows that many smaller ice shelves and glaciers around the AP have exhibited re-advances and retreats throughout the Holocene (Brachfeld et al., 2003; Hall, 2009; Hjort et al., 1997; Pudsey and Evans, 2001; Pudsey et al., 2006), the resolution of the few RSL curves in Antarctica prevents a full understanding of the solid-Earth response to such events.

The AP lacks coastal marshes, microatolls, and other geological formations containing biological proxies often used for the generation of high-precision RSL curves. In their absence, most RSL reconstructions within Antarctica have turned to using radiocarbon dating of organic material preserved within morphologic features, such as beach ridges or isolation basins (Bentley et al., 2005; Fretwell et al., 2010; Hall, 2010; Hjort et al., 1997; Hodgson et al., 2013; Roberts et al., 2009; Roberts et al., 2011; Simkins et al., 2013; Simms et al., 2018; Watcham et al., 2011). Isolation basins capture the age and elevation of RSL as the basin transitions from salt to fresh water or vice versa. However, finding an adequate number of basins at varying elevations is difficult and has failed to produce any late Holocene RSL reconstructions with more than half a dozen sea-level index points.

Beach ridges, whose elevations and formation ages have been used to estimate RSL changes, provide their own set of challenges. Often the little organic material preserved within paleo-beach ridges, such as bones, shells, or seaweed, was reworked and may not reflect the age of beach formation. As a result, the age obtained often provides only limiting data, either a maximum age of the beach in the case of material being reworked into the beach, or as a minimum age of the beach in the case of the material being deposited on the beach after its formation (such as when a penguin dies while nesting on the paleo-beach). Recent efforts have utilized optically-simulated luminescence-dating of cobbles on beach ridges, which more-accurately reflects the age of beach formation, but such methods have thus far resulted in large errors up to 36% of the age (Simkins et al., 2016; Simkins et al., 2013). Additionally, beach ridge elevation is a function of not only mean sea level, but also wave energy, storm energy, tidal range, grain size and shape, and sediment availability (Lindhorst and Schutter, 2014; Scheffers et al., 2012).

In this study, I present a new RSL reconstruction based on radiocarbon dated seaweed preserved within bedding of beach-ridge deposits from Joinville Island along the northeastern Antarctica Peninsula (Fig. 26). This new sea-level reconstruction is used to determine if similar periods of punctuated uplift, as occurred following the demise of the Larsen B Ice Shelf in 2002, occurred at other time periods during the Holocene.

4.2 Methods

GPS and ground-penetrating radar (GPR) surveys were conducted across 31 beach ridges on the eastern side of Tay Head, a small (~2.5 x 2 km) peninsula on the southern side of Joinville Island (Fig. 26). Beaches on Tay Head Peninsula were numbered from 1 to 31, lowest to highest (i.e. youngest to oldest). Elevation data were obtained using a UNAVCO Trimble Net R9 GNSS Receiver, a local Trimble Net R9 Receiver base station, and the O'Higgins permanent GPS station (www.sonel.org), located ~115 km away, upon failure of the local base station. Beach-ridge elevations were obtained from kinematic mode GPS surveys across the crest of each beach ridge (Figs 26c and 27), except for beach ridges 2 and 3, which each have 3 static elevation points due to the presence of wildlife. GPS data have horizontal and vertical precisions of < 0.25 m. Elevations were converted to mean sea level using 2 days of data from a locally deployed tide gauge matched to the tide gauge at Bahia Esperanza ~50 km away.

The incorporation of seaweed into the modern beaches was observed during the field campaign (Fig. 28). Thirty cm deep pits in the crest of the lower 18 beach ridges, except for beach ridge 14, revealed stratified gravels with mats of seaweed (Fig. 28) that often incorporated limpet shells. Both mats and limpets were radiocarbon dated (Table 5). Thus, the *in situ* (cf. reworked) samples obtained on Joinville Island likely provide a better estimate of the timing of beach-ridge formation than minimum or maximum beach age constraints in many previous studies. Radiocarbon ages were first calibrated in CALIB v7.1 (Stuiver et al.,

2018) using the MARINE13 calibration curve (Reimer et al., 2013) with a reservoir correction of 791 ± 121 years (Hall et al., 2010).

The Bacon age-depth modeling program (Blaauw and Christen, 2011) was used to estimate a progradation rate through time, using distance from the start of GPR LINE05 at the shoreline instead of the traditionally used depth. The RSL reconstruction was made using the mean elevation of beach ridges from GPS surveys and the median age for each beach ridge as derived from the Bacon age-model. To calculate the rate of RSL change (dRSL) through time, a Monte Carlo simulation was run using the equation

$$dRSL = \frac{(z_{i+1} - z_i)}{(t_{i+1} - t_i)}, \quad (1)$$

where *z* is the elevation of the beach ridge as chosen randomly from a Gaussian PDF determined from beach-ridge GPS surveys, and *t* is the age of the beach ridge chosen from ages output from the Bacon age-model, which prohibits age reversals.

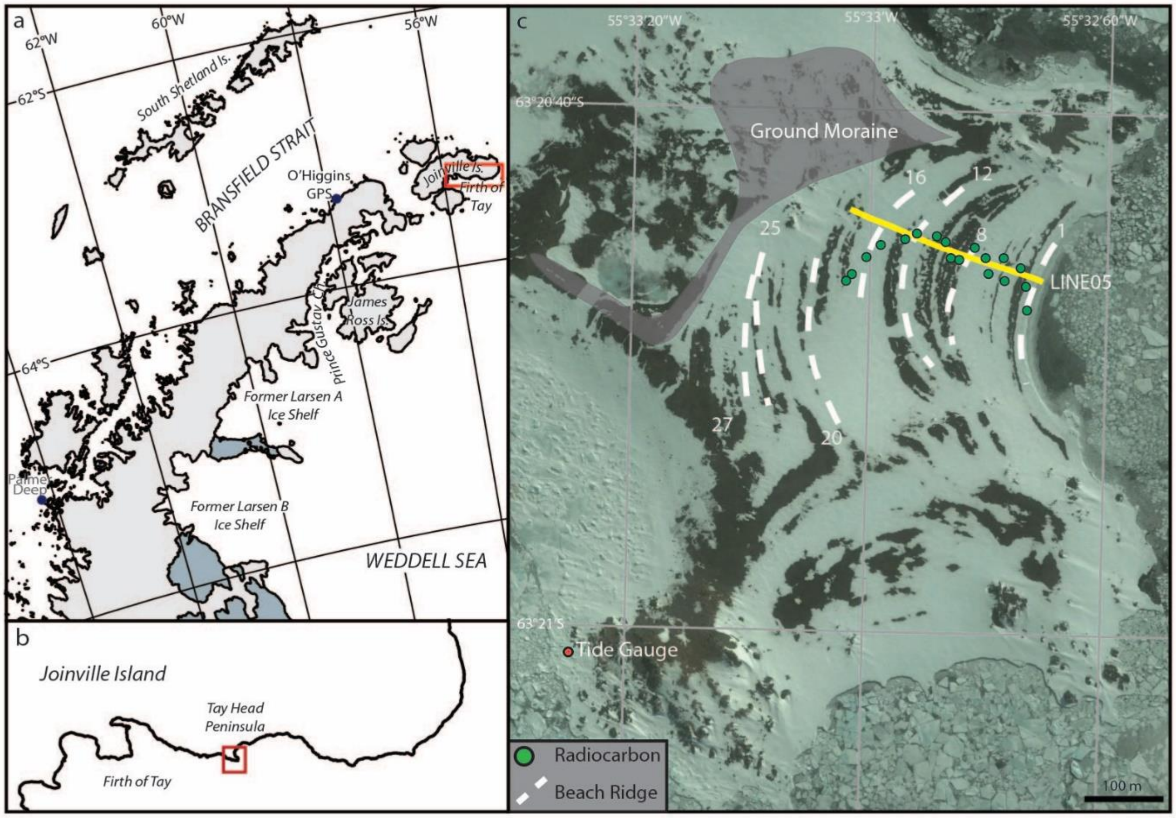

Figure 26. Location map of Joinville Island. a, Regional map of the Antarctic Peninsula. Joinville Island is located at the northeastern tip of the peninsula, red box indicates area shown in panel b. b, Tay Head Peninsula, on the southern edge of Joinville Island, sticks out into the Firth of Tay, red box indicates area shown in panel c. c, Selected beach ridges to show morphology, shown by dashed white lines, on Tay Head Peninsula, as well as radiocarbon collection sites in green circles, and GPR transect LINE05 in yellow.

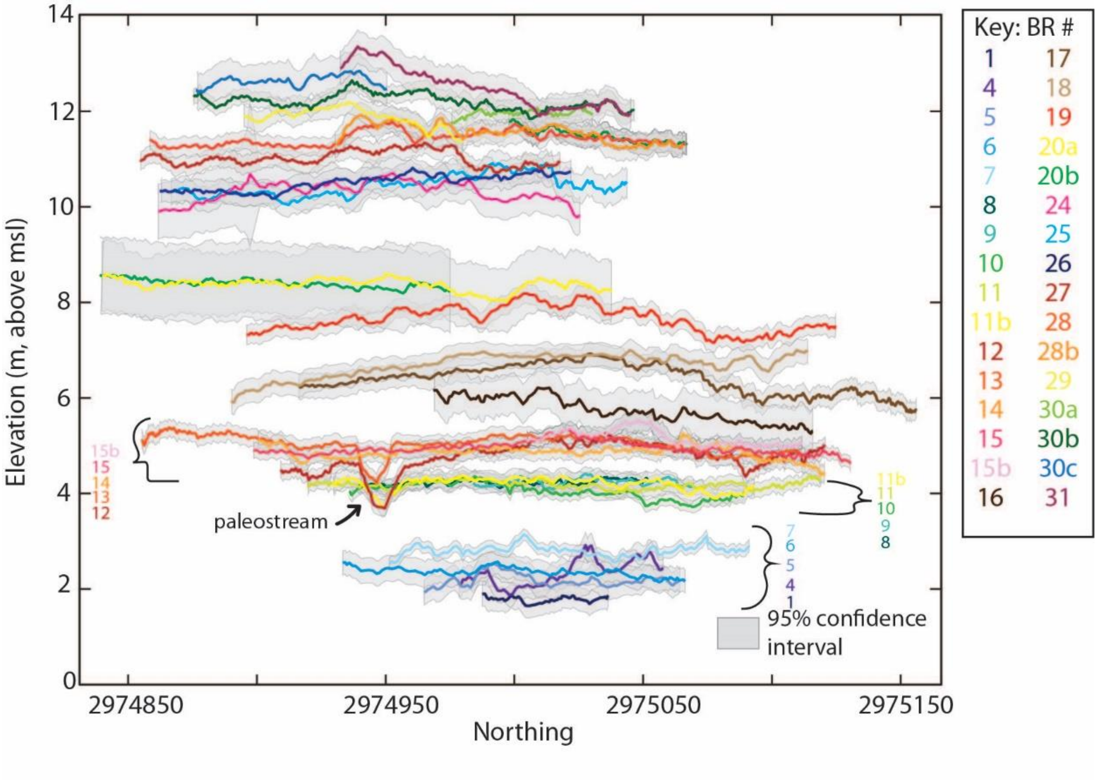

Figure 27. Transects of the beach ridge elevations, with 95% confidence interval shown by gray boxes. Beach ridges 2 and 3 were not surveyed in kinematic mode GPS, therefore are not included in the chart. Beach ridges 21 to 23 failed GPS processing due to large errors and are not included in the chart. Paleostream in beach ridges 11-13 was removed when calculating the mean beach ridge elevation.

Figure 28. Seaweed on and in the beach ridges. a, Picture showing wrack line of seaweed on the modern beach at Tay Head Peninsula. b, Layer of in situ seaweed, outlined in dashed white lines, from a pit dug into beach ridge 10.

Table 6. Radiocarbon dates on organic material found in beach ridges on Joinville Island.

Sample ID	Lab ID	Material	BR	Mean elevation (m)	14C age (BP)	CALIB calibrated ages in yr BP		Bacon calibrated ages in yr BP	
						Range	Median	Age	2σ
JVRC_01	208364	seaweed	1	1.28 ± 0.20	980 ± 15	< 448	< 448	105	160
JVRC_02	208209	shell	1	1.28 ± 0.20	1000 ± 20	< 448	< 448	105	160
JVRC_09	208210	shell	3	1.60 ± 0.72	2065 ± 20	610 – 1090	825	695	190
JVRC_11	208211	shell	4	1.86 ± 0.57	2185 ± 20	692 – 1194	945	950	145
JVRC_12	208365	seaweed	4	1.86 ± 0.57	2175 ± 20	680 – 1183	935	950	145
JVRC_15	208212	shell	5	1.68 ± 0.32	2305 ± 20	800 – 1294	1070	1045	135
JVRC_19-s	208366	seaweed	6	1.84 ± 0.25	2420 ± 15	916 – 1415	1180	1160	130
JVRC_19-l	208213	shell	6	1.84 ± 0.25	2410 ± 20	910 – 1407	1170	1160	130
JVRC_22.1	210312	seaweed	7b	2.42 ± 0.26	2595 ± 20	1091 – 1631	1364	1320	125
JVRC_22.2	210313	shell	7b	2.42 ± 0.26	2625 ± 20	1151 – 1682	1394	1320	125
JVRC_26-s	208637	seaweed	8	3.74 ± 0.15	2710 ± 20	1245 – 1770	1480	1540	125
JVRC_26-l	208214	shell	8	3.74 ± 0.15	2755 ± 20	1280 – 1807	1530	1540	125
JVRC_30	208368	seaweed	9	3.74 ± 0.18	2895 ± 20	1391 – 1968	1685	1630	130
JVRC_33	208369	seaweed	10	3.54 ± 0.33	2865 ± 15	1363 – 1927	1650	1710	135
JVRC_36	208370	seaweed	11	3.69 ± 0.19	2980 ± 15	1506 – 2094	1785	1800	145
JVRC_37	208371	seaweed	11b	3.70 ± 0.28	3075 ± 15	1588 – 2210	1890	1975	155
JVRC_39-s	208372	seaweed	12	4.30 ± 0.47	3275 ± 20	1828 – 2443	2140	2240	155
JVRC_39-l	208215	shell	12	4.30 ± 0.47	3300 ± 20	1854 – 2486	2170	2240	155
JVRC_40	208373	seaweed	13	4.56 ± 0.35	3345 ± 15	2589 – 2591	2220	2345	165
JVRC_42	208374	seaweed	15	4.43 ± 0.28	3725 ± 15	2347 – 2967	2690	2705	175
JVRC_44-s	208375	seaweed	16	5.24 ± 0.61	3880 ± 40	2575 – 3229	2890	2845	155
JVRC_44-l	208216	shell	16	5.24 ± 0.61	3935 ± 20	2694 – 3264	2950	2845	155
JVRC_45	208388	seaweed	17	5.82 ± 0.67	4060 ± 15	2787 – 3375	3095	2995	170
JVRC_49	208376	seaweed	18	6.18 ± 0.54	4180 ± 15	2925 – 3544	3240	3095	195
JVRC_50	208217	shell	2	1.74 ± 0.62	970 ± 20	< 448	< 448	235	175
JVRC_51	208377	seaweed	2	1.74 ± 0.62	950 ± 15	< 448	< 448	235	175

4.3 Results

Ground-penetrating radar (GPR) profiles collected perpendicular to the beach ridges display seaward-dipping reflections, at about 5-7°, typical of beach progradation (Lindhorst and Schutter, 2014) (Fig. 29). An erosional surface is imaged below the crest of beach ridges 1 and 2 and reflections within beach ridge 2 dip landward, onlapping the erosional surface (Fig. 29). Beaches 1-18 display no changes in grain characteristics within error, including sorting, rounding, or size (Fig. 30c).

RSL on Tay Head Peninsula shows an overall fall of 4.9 ± 0.58 m from the oldest dated beach ridge at 3095 ± 195 cal yr BP (calibrated years before present; present defined as 1950) to the modern (Fig. 30a). A discrete fall in RSL of 1.32 ± 0.15 m is observed between beach ridges 7b and 8. A trough (Fig. 29) and potential RSL fall is observed between beach ridges 12 and 11b (Fig. 30a), and a ~460-year hiatus occurs between beach ridges 3 and 2. Progradation of the beach ridges was relatively constant through time at a rate of ~9 cm/yr, until a significant decrease ~695 cal yr BP to present. An abrupt increase in the rate of RSL change occurs at 1540 ± 125 cal yr BP, increasing from -0.01 ± 3.95 mm/yr to 6.06 ± 4.72 mm/yr after the deposition of beach ridge 8 (Fig. 30b). This increase is followed by a 500-year gradual decrease in rates of RSL fall, with another possible increase in the last 200 years (Fig. 30b).

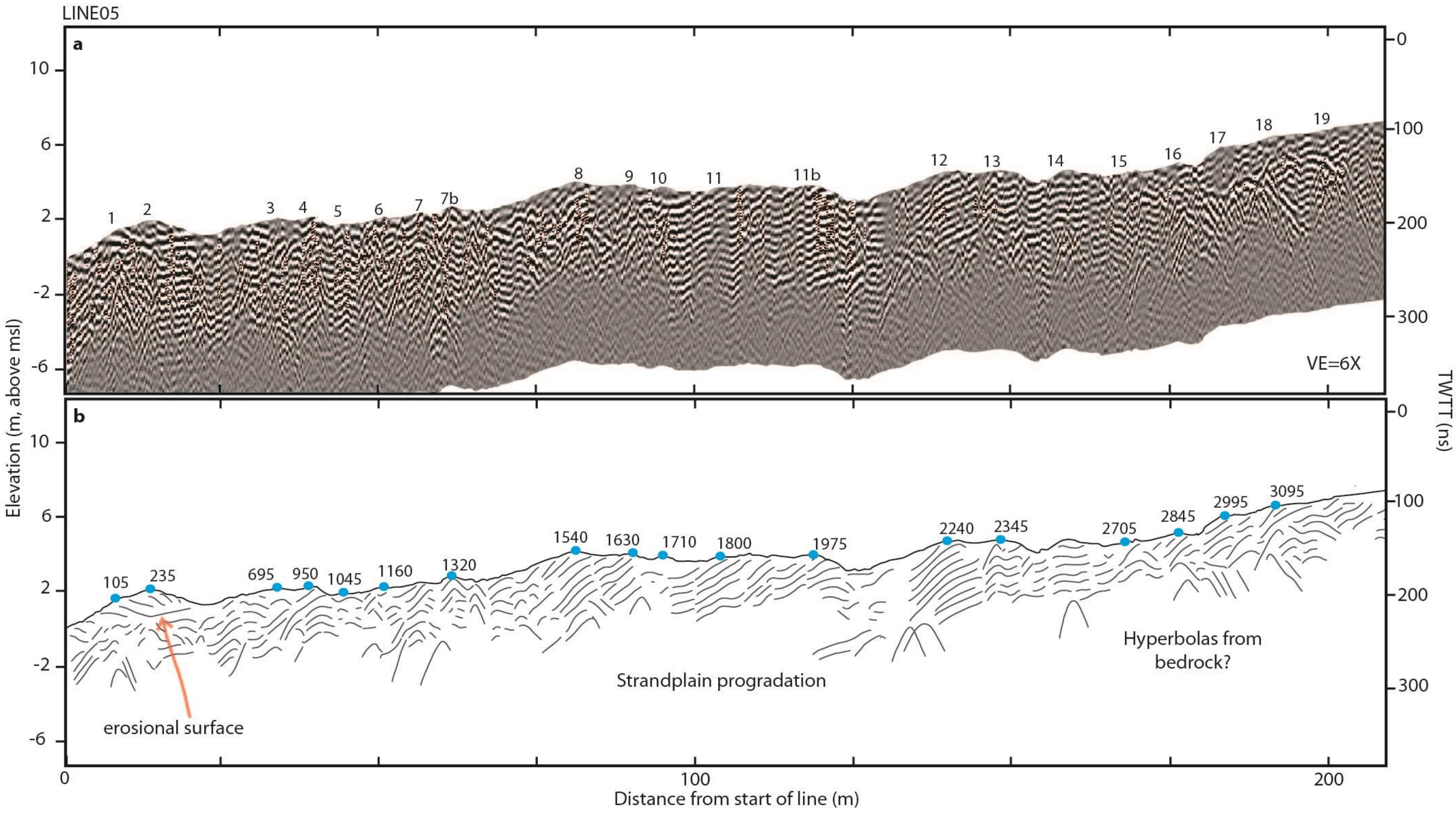

Figure 29. Beach ridge stratigraphy. a, 200 MHz GPR LINE05 labeled by beach ridge. TWTT is two-way travel time, VE is vertical exaggeration, msl is mean sea level. b, Traces of GPR reflections, labeled by beach ridge age.

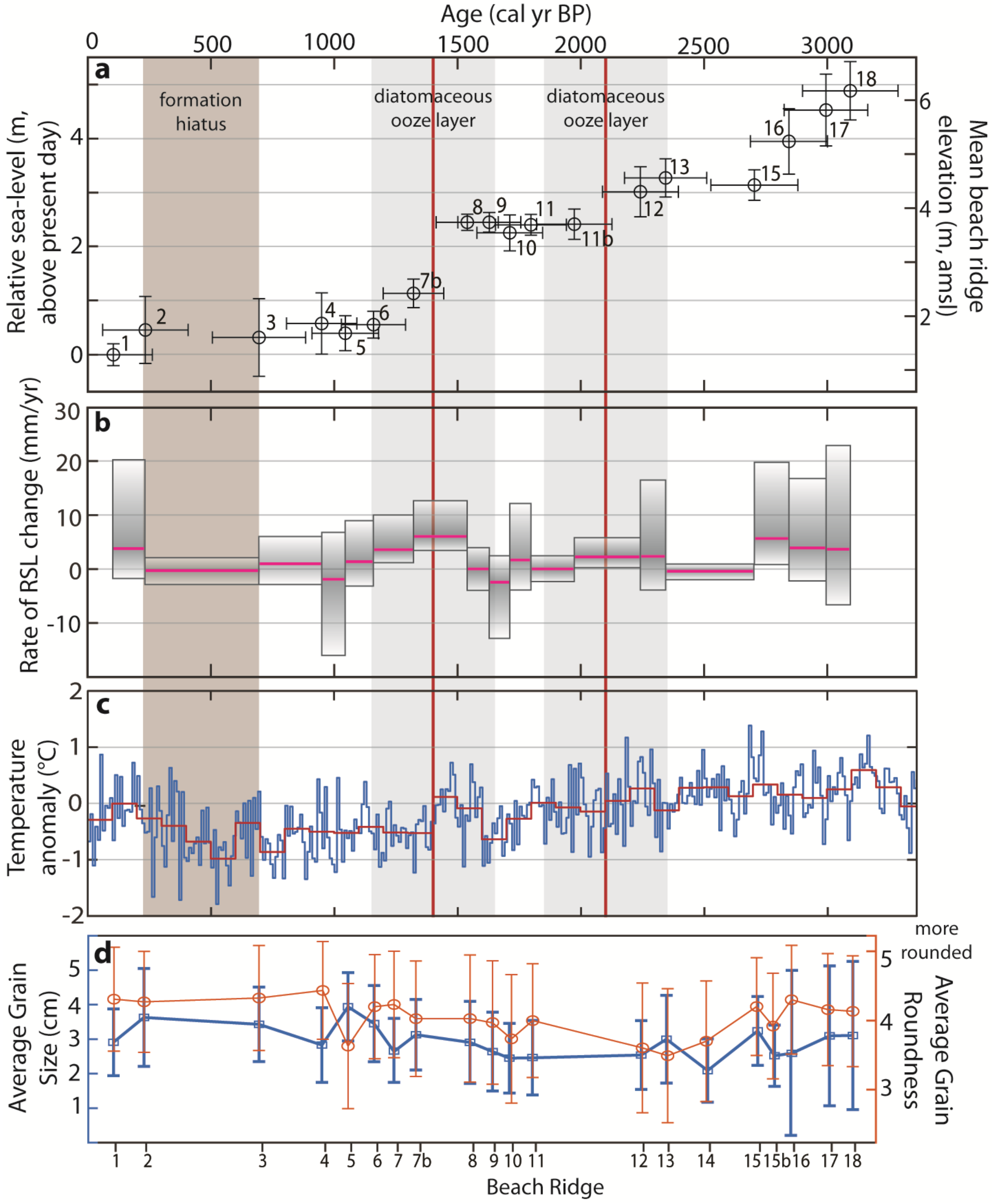

Figure 30. RSL reconstruction, temperature anomaly, and sediment changes on beach ridges through the Late Holocene. 2 red lines show ages of diatomaceous ooze layers from Brachfeld et al., 2003, with error in grey boxes. Hiatus in beach ridge formation shown by brown box. a, RSL reconstruction for the beach ridges on Joinville Island, errors are shown as 2σ. b, Rates of RSL change, positive is RSL fall, negative is RSL rise, pink link shows the median rate of RSL change and boxes show 95% confidence intervals. c, James Ross Island temperature reconstruction, blue line shows 10-year average, red line shows 100-year average (Mulvaney et al., 2012). d, Grain characteristics showing error as 1σ. Roundness is plotted using the Powers scales, 5 is well-rounded, 1 is angular.

4.3 Beach Ridges as RSL Indicators

A change in formation processes on beach ridges (e.g. waves, sea ice, etc.), could inhibit the use of their elevation as RSL indicators. However, a change in these processes would also change the grain size and shape, as well as stratigraphy recorded in the GPR of the beach ridges. Yet, none of these characteristics within the GPR or grain characteristics change, except for an erosional surface observed beneath beach ridges 1 and 2 (discussed below). Additionally, features typical of ice-push processes, such as melt pits or push ridges (Butler, 1999), are not observed within the lower 18 beach ridges. Furthermore, the lower beaches exhibit stratification, uncommon in ice-formed features. Together, this is taken to indicate that no significant changes in beach ridge formation mechanisms occurred over the last 3000 years.

Other mechanisms that could be responsible for sudden elevation changes include earthquakes or tidal changes. Although the continent of Antarctica is stable, the Antarctic Peninsula is known to be an area of active seismicity (Kaminuma, 1995). However, existing catalogs of seismicity across the AP suggest earthquakes are centered around the South Shetland Islands (Fig. 26a) and the South Scotia Ridge (farther to the northeast) – both tectonic arcs. Furthermore, estimates of tectonic uplift in the South Shetland Islands range from 0.4 to 0.48 mm/yr (Watcham et al., 2011), an order of magnitude less than the maximum rate of RSL change of 6.06 ± 4.72 mm/yr calculated for Joinville Island. Although no paleo-tide reconstructions are available for the Firth of Tay, the bathymetry of the fjord would not have changed greatly with 2-3 m of RSL change. Thus, following Fretwell et al. (2010), the changes in beach-ridge elevations from Joinville Island are considered to largely reflect changes in RSL.

4.4 Links to Ice-Mass Changes

Coincident with the RSL falls at ~1540 cal yr BP and possibly ~2240 cal yr BP are two distinct diatomaceous ooze layers deposited beneath the former Larsen A ice shelf, dated from sediment cores to be 1400 ± 250 cal yr BP and 2100 ± 250 cal yr BP (Brachfeld et al., 2003). The abundance of diatoms in these layers reflects higher surface water productivity, indicative of an ice free environment (Buffen et al., 2007). Additionally, low overall total organic carbon and elevated water content measured in the layers could indicate an increasing influence of meltwater (Brachfeld et al., 2003; Domack et al., 1993). Temperature anomaly records from an ice core at James Ross Island (Fig. 26a), located south of Joinville Island, indicate increased warmth before these two time periods (Mulvaney et al., 2012), and smaller ice shelves are known to respond faster to climatic changes, enhanced by surface-crevasse propagation due to increased surface meltwater (Scambos et al., 2000). Southern Prince Gustav Channel, which had an ice shelf until it's collapse in 1995, is thought to have had episodes of growth and decay during the Holocene, although the scarcity of carbonate material within cores from the channel preclude accurate age dating of these episodes (Nývlt et al., 2014; Pudsey et al., 2006).

Following the 2002 break-up of Larsen B, the uplift rates recorded in GPS at Palmer Station increased from 0.08 ± 1.87 mm/yr to 8.75 ± 0.64 mm/yr (Thomas et al., 2011). The increased rate of RSL fall ~1540 cal yr BP observed at Joinville Island, ~100 km away from Prince Gustav Channel and ~200 km away from Larsen A, is similar in magnitude to the uplift rates observed at Palmer Station, ~100 km away from the former Larsen B ice shelf. Changes in the sea surface height, including gravitational attraction between the ice and water, for the AP are estimated to be ~0.2-0.3 mm/yr for the time period between 1500 cal yr BP and the present (Simms et al., 2018) indicating they alone cannot account for the high rate of RSL fall observed at Joinville Island. As ice shelves retreat, the glaciers that were once buttressed by them accelerate flow into marine waters, indicating that accelerated glacial mass loss following a potential collapse of the Larsen A or Prince Gustav Channel ice shelves may have been responsible for the increased rate of RSL fall. However, without more records of RSL from across the AP, the precise size or location of the ice mass loss resulting in the increase in the rate of RSL fall on Joinville Island cannot be determined.

The hiatus in beach ridge formation and slowdown in progradation rate after 695 ± 190 cal yr BP may suggest a reduction in sediment supply and/or erosion of the beach. The erosional surface imaged beneath beach ridges 1 and 2 precedes 235 ± 175 cal yr BP and postdates the deposition of beach ridge 3 at 695 ± 190 cal yr BP. Possible causes of the erosional surface include increased wave or storm activity, or a minor sea-level transgression. No changes in grain size or roundness were found between beach ridges 2 and 3, as would be expected if the erosion was the result of greater wave action or storm activity (Fig. 30c). The hiatus in deposition and erosional surface correspond to cooler temperatures in the AP from 370 to 70 cal yr BP with minor glacial advances documented in West Antarctica (Consortium et al., 2013; Domack et al., 1995). Furthermore, temperature records from the nearby James Ross Island ice core show a cooling trend during this time interval (Mulvaney et al., 2012), causing an advance of local glaciers on the island (Davies et al., 2014). The erosional surface therefore may have formed as a result of RSL rise on Tay Head Peninsula driven by the GIA response to a local or regional glacial advance. Following the retreat of previously advancing glaciers, the land would once again rebound, causing an RSL fall, and the preservation of beach ridges 2 and 1.

Overall, the RSL reconstruction of Joinville Island follows an exponential fall in sea-level through time, also reflected in the closest RSL curve ~100 km away at Beak Island (Roberts et al., 2011). However, the limited resolution (3 RSL points) of the Beak Island data prevents comparison of decadal to centennial changes. The centennial timescale variability of RSL rates presented in the RSL reconstruction, suggests that even small episodes of growth and decay of ice sheets over time can induce a recordable solid Earth response. Such a response is only possible with lower upper mantle viscosities than currently assumed in most global-scale GIA models (e.g. ICE-5G; Simms et al., 2018). Thus, not only are such low upper mantle viscosities necessary for explaining ongoing rapid changes recorded in GPS studies (e.g. (Nield et al., 2014) but also at time scales relevant for the Holocene. As the resolution and number of RSL records increase, future GIA models should incorporate these smaller oscillations in ice sheets to investigate the impact on RSL rates through time. Current low resolution GIA models could be masking the behavior of the ice sheets during the early Holocene and Late Pleistocene, and that may have an impact on ice sheet reconstructions and sea-level predictions.

CHAPTER 5

5. Conclusions

At the Elwha River delta, swash bars form at the leading edge of the delta after the deposition of mouth bars following moderate increases in discharge along the river. However, most swash bars are eroded by the migration of the river mouth channel, as only ten of thirty-seven swash bars that formed remained on the delta as of July 2016. The swash bars that did remain, either welded to the shore or to previously deposited swash bars, forming a large barrier at the delta front. This barrier is similar in scale to a vegetated ridge downdrift on the delta plain, indicating that the beach ridges that form in small mountainous river deltas may be more indicative of a large sediment pulse to the fluvial system rather than a single flood.

The coastal Oxnard Plain episodically prograded since at least ~600 years ago. The rates of progradation have remained relatively constant at centennial timescales (150-200 years) through time, within the range of 0.3 to 1.4 m a^{-1}. Periods of extended drought can cause severe erosion, removing up 90 m of the beach, equivalent to 5 to 120 years of the sediment record. Although the coast exhibited progradation since before 1435, as the intensity of droughts is expected to increase in the future, the coast may be subject to more erosion in the future.

The reconstructed relative sea-level history from beach ridges at Joinville Island on the northeastern Antarctic Peninsula show that sea-level fell 4.9 ± 0.58 m over the last 3100 years. However, the faster rates of RSL fall from 1540 ± 125 cal yr BP to 1320 ± 125 cal yr BP, may be linked to local ice-mass changes, possibly induced by the loss of the buttressing effects from the collapse of ice shelves. The rapid Earth response to ice mass loss on centennial time scales further supports recent work showing the Antarctic Peninsula has a lower upper mantle viscosity than is currently used in global GIA models. Future GIA models should incorporate theses smaller ice mass fluctuations to accurately reconstruct past ice-sheets and model the future response to ice mass loss.

REFERENCES

Ainsworth, R. B., Vakarelov, B. K., MacEachern, J. A., Nanson, R. A., Lane, T. I., Rarity, F., and Dashtgard, S. E., 2016, Process-Driven Architectural Variability In Mouth-Bar Deposits: A Case Study From A Mixed-Process Mouth-Bar Complex, Drumheller, Alberta, Canada: Journal of Sedimentary Research, v. 86, no. 5, p. 512-541.

Ainsworth, R. B., Vakarelov, B. K., and Nanson, R. A., 2011, Dynamic spatial and temporal prediction of changes in depositional processes on clastic shorelines: Toward improved subsurface uncertainty reduction and management: AAPG bulletin, v. 95, no. 2, p. 267-297.

Anderson, S. R., Ejarque, A., Rice, J., Smith, S. J., and Lebow, C. G., 2015, Historic and Holocene Environmental Change in the San Antonio Creek Basin, Mid-coastal California: Quaternary Research, v. 83, no. 2, p. 273-286.

Andrews, E. D., Antweiler, R. C., Neiman, P. J., and Ralph, F. M., 2004, Influence of ENSO on Flood Frequency along the California Coast: Journal of Climate, v. 17, no. 2, p. 337-348.

Anthony, E. J., 2015, Wave influence in the construction, shaping and destruction of river deltas: A review: Marine Geology, v. 361, p. 53-78.

Barnard, P., and Warrick, J., 2010, Dramatic beach and nearshore morphological changes due to extreme flooding at a wave-dominated river mouth: Marine Geology, v. 271, no. 1-2, p. 131-148.

Barnard, P. L., Revell, D. L., Hoover, D., Warrick, J., Brocatus, J., Draut, A. E., Dartnell, P., Elias, E., Mustain, N., and Hart, P. E., 2009, Coastal processes study of Santa Barbara and Ventura counties, California: Citeseer.

Bentley, M., Hodgson, D., Smith, J., and Cox, N., 2005, Relative sea level curves for the South Shetland Islands and Marguerite Bay, Antarctic Peninsula: Quaternary Science Reviews, v. 24, no. 10-11, p. 1203-1216.

Bhattacharya, J., and Giosan, L., 2003, Wave-influenced deltas: geomorphological implications for facies reconstruction: Sedimentology, v. 50, no. 1, p. 187-210.

Blaauw, M., and Christen, J. A., 2011, Flexible paleoclimate age-depth models using an autoregressive gamma process: Bayesian analysis, v. 6, no. 3, p. 457-474.

Brachfeld, S., Domack, E., Kissel, C., Laj, C., Leventer, A., Ishman, S., Gilbert, R., Camerlenghi, A., and Eglinton, L. B., 2003, Holocene history of the Larsen-A Ice Shelf constrained by geomagnetic paleointensity dating: Geology, v. 31, no. 9, p. 749-752.

Bristow, C., Chroston, P., and Bailey, S., 2000, The structure and development of foredunes on a locally prograding coast: insights from ground-penetrating radar surveys, Norfolk, UK: Sedimentology, v. 47, no. 5, p. 923-944.

Bristow, C. S., and Pucillo, K., 2006, Quantifying rates of coastal progradation from sediment volume using GPR and OSL: the Holocene fill of Guichen Bay, south-east South Australia: Sedimentology, v. 53, no. 4, p. 769-788.

Brownlie, W. R., and Taylor, B. D., 1981, Sediment management for southern California mountains, coastal plains and shoreline. Part C: Coastal sediment delivery by major rivers in southern California.

Bruun, P., 1962, Sea-level rise as a cause of shore erosion: Journal of the Waterways and Harbors division, v. 88, no. 1, p. 117-132.

Buffen, A., Leventer, A., Rubin, A., and Hutchins, T., 2007, Diatom assemblages in surface sediments of the northwestern Weddell Sea, Antarctic Peninsula: Marine Micropaleontology, v. 62, no. 1, p. 7-30.

Butler, E. R., 1999, Process environments on modern and raised beaches in McMurdo Sound, Antarctica: Marine Geology, v. 162, no. 1, p. 105-120.

Buynevich, I., FitzGerald, D., and van Heteren, S., 2004, Sedimentary records of intense storms in Holocene barrier sequences, Maine, USA: Marine Geology, v. 210, no. 1-4, p. 135-148.

Buynevich, I., and FitzGerald, D. M., 2001, Styles of Coastal Progradation Revealed in Subsurface Records of Paraglacial Barriers: Duxbury, Massachusetts, USA: Journal of Coastal Research, p. 194-208.

Buynevich, I. V., FitzGerald, D. M., and Goble, R. J., 2007, A 1500 yr record of North Atlantic storm activity based on optically dated relict beach scarps: Geology, v. 35, no. 6, p. 543-546.

Carter, R., 1986, The morphodynamics of beach-ridge formation: Magilligan, Northern Ireland: Marine Geology, v. 73, no. 3, p. 191-214.

Cayan, D. R., Das, T., Pierce, D. W., Barnett, T. P., Tyree, M., and Gershunov, A., 2010, Future dryness in the southwest US and the hydrology of the early 21st century drought: Proceedings of the National Academy of Sciences, v. 107, no. 50, p. 21271-21276.

Cole, K. L., and Liu, G.-W., 1994, Holocene Paleoecology of an Estuary on Santa Rosa Island, California: Quaternary Research, v. 41, no. 3, p. 326-335.

Consortium, P. k., Ahmed, M., Anchukaitis, K. J., Asrat, A., Borgaonkar, H. P., Braida, M., Buckley, B. M., Büntgen, U., Chase, B. M., Christie, D. A., Cook, E. R., Curran, M. A. J., Diaz, H. F., Esper, J., Fan, Z.-X., Gaire, N. P., Ge, Q., Gergis, J., González-Rouco, J. F., Goosse, H., Grab, S. W., Graham, N., Graham, R., Grosjean, M., Hanhijärvi, S. T., Kaufman, D. S., Kiefer, T., Kimura, K., Korhola, A. A., Krusic, P. J., Lara, A., Lézine, A.-M., Ljungqvist, F. C., Lorrey, A. M., Luterbacher, J., Masson-Delmotte, V., McCarroll, D., McConnell, J. R., McKay, N. P., Morales, M. S., Moy, A. D., Mulvaney, R., Mundo, I. A., Nakatsuka, T., Nash, D. J., Neukom, R., Nicholson, S. E., Oerter, H., Palmer, J. G., Phipps, S. J., Prieto, M. R., Rivera, A., Sano, M., Severi, M., Shanahan, T. M., Shao, X., Shi, F., Sigl, M., Smerdon, J. E., Solomina, O. N., Steig, E. J., Stenni, B., Thamban, M., Trouet, V., Turney, C. S. M., Umer, M., van Ommen, T., Verschuren, D., Viau, A. E., Villalba, R., Vinther, B. M., von Gunten, L., Wagner, S., Wahl, E. R., Wanner, H., Werner, J. P., White, J. W. C., Yasue, K., and Zorita, E., 2013, Continental-scale temperature variability during the past two millennia: Nature Geoscience, v. 6, p. 339.

Cook, E. R., Woodhouse, C. A., Eakin, C. M., Meko, D. M., and Stahle, D. W., 2004, Long-Term Aridity Changes in the Western United States: Science, v. 306, no. 5698, p. 1015-1018.

Costas, S., Ferreira, Ó., Plomaritis, T. A., and Leorri, E., 2016, Coastal barrier stratigraphy for Holocene high-resolution sea-level reconstruction: Scientific reports, v. 6, p. 38726.

Davies, B. J., Golledge, N. R., Glasser, N. F., Carrivick, J. L., Ligtenberg, S. R., Barrand, N. E., Van Den Broeke, M. R., Hambrey, M. J., and Smellie, J. L., 2014, Modelled glacier response to centennial temperature and precipitation trends on the Antarctic Peninsula: Nature Climate Change, v. 4, no. 11, p. 993.

Domack, E. W., Ishman, S. E., Stein, A. B., McClennen, C. E., and Jull, A. T., 1995, Late Holocene advance of the Müller Ice Shelf, Antarctic Peninsula: sedimentological, geochemical and palaeontological evidence: Antarctic Science, v. 7, no. 2, p. 159-170.

Domack, E. W., Mashiotta, T. A., Burkley, L. A., and Ishman, S. E., 1993, 300-year cyclicity in organic matter preservation in Antarctic fjord sediments: The Antarctic Paleoenvironment: A Perspective on Global Change: Part Two, p. 265-272.

Dominguez, J., 1996, The Sao Francisco strandplain: a paradigm for wave-dominated deltas?: Geological Society, London, Special Publications, v. 117, no. 1, p. 217-231.

Downing, J., 1983, The coast of Puget Sound: Its processes and development, University of Washington Press.

Downs, P. W., Dusterhoff, S. R., and Sears, W. A., 2013, Reach-scale channel sensitivity to multiple human activities and natural events: Lower Santa Clara River, California, USA: Geomorphology, v. 189, p. 121-134.

Du, X., Hendy, I., and Schimmelmann, A., 2018, A 9000-year flood history for Southern California: A revised stratigraphy of varved sediments in Santa Barbara Basin: Marine Geology, v. 397, p. 29-42.

Duda, J. J., Warrick, J. A., and Magirl, C. S., 2011, Coastal and lower Elwha River, Washington, prior to dam removal—history, status, and defining characteristics: Coastal Habitats of the Elwha River, Washington—Biological and Physical Patterns and Processes Prior to Dam Removal. US Geological Survey Scientific Investigations Report, v. 5120, p. 1-26.

Durcan, J. A., and Duller, G. A. T., 2011, The fast ratio: A rapid measure for testing the dominance of the fast component in the initial OSL signal from quartz: Radiation Measurements, v. 46, no. 10, p. 1065-1072.

East, A. E., Pess, G. R., Bountry, J. A., Magirl, C. S., Ritchie, A. C., Logan, J. B., Randle, T. J., Mastin, M. C., Minear, J. T., Duda, J. J., Liermann, M. C., McHenry, M. L., Beechie, T. J., and Shafroth, P. B., 2015, Large-scale dam removal on the Elwha River, Washington, USA: River channel and floodplain geomorphic change: Geomorphology, v. 228, p. 765-786.

Edmonds, D., and Slingerland, R., 2007, Mechanics of river mouth bar formation: Implications for the morphodynamics of delta distributary networks: Journal of Geophysical Research: Earth Surface, v. 112, no. F2.

Eidam, E., Ogston, A., Nittrouer, C., and Warrick, J., 2016, Tidally dominated sediment dispersal offshore of a small mountainous river: Elwha River, Washington State: Continental Shelf Research, v. 116, p. 136-148.

Ejarque, A., Anderson, R. S., Simms, A. R., and Gentry, B. J., 2015, Prehistoric fires and the shaping of colonial transported landscapes in southern California: A paleoenvironmental study at Dune Pond, Santa Barbara County: Quaternary Science Reviews, v. 112, p. 181-196.

Engstrom, W. N., 1994, Nineteenth-Century Coastal Gales of Southern California: Geographical Review, v. 84, no. 3, p. 306-315.

Engstrom, W.N., 1996, The California Storm of January 1862: Quaternary Research, v. 46, no. 2, p. 141-148.

Ferreira, J. C. T., and Warrick, J., 2017, Oceanographic measurements obtained offshore of the Elwha River delta in coordination with the Elwha River Restoration Project, Washington, USA, 2010-2014: U.S. Geological Survey data release, https://doi.org/10.5066/F7CR5RW8.

Fielding, C. R., Trueman, J. D., and Alexander, J., 2005, Sharp-based, flood-dominated mouth bar sands from the Burdekin River Delta of northeastern Australia: extending the spectrum of mouth-bar facies, geometry, and stacking patterns: Journal of Sedimentary Research, v. 75, no. 1, p. 55-66.

FitzGerald, D. M., Buynevich, I. V., and Rosen, P. S., 2001, Geological evidence of former tidal inlets along a retrograding barrier: Duxbury Beach, Massachusetts, USA: Journal of Coastal Research, p. 437-448.

Foley, M. M., Duda, J. J., Beirne, M. M., Paradis, R., Ritchie, A., and Warrick, J. A., 2015, Rapid water quality change in the Elwha River estuary complex during dam removal: Limnology and Oceanography, v. 60, no. 5, p. 1719-1732.

Foley, M. M., and Warrick, J. A., 2017, Ephemeral seafloor sedimentation during dam removal: Elwha River, Washington: Continental Shelf Research, v. 150, p. 36-47.

Folk, R. L., and Ward, W. C., 1957, Brazos River bar: a study in the significance of grain size parameters: Journal of Sedimentary Research, v. 27, no. 1.

Fraticelli, C. M., 2006, Climate forcing in a wave-dominated delta: the effects of drought–flood cycles on delta progradation: Journal of Sedimentary Research, v. 76, no. 9, p. 1067-1076.

Fretwell, P. T., Hodgson, D., Watcham, E., Bentley, M., and Roberts, S. J., 2010, Holocene isostatic uplift of the South Shetland Islands, Antarctic Peninsula, modelled from raised beaches: Quaternary Science Reviews, v. 29, no. 15-16, p. 1880-1893.

Garrison, J. R., Jr., Williams, J., Potter Miller, S., Weber, E. T., II, McMechan, G., and Zeng, X., 2010, Ground-Penetrating Radar Study of North Padre Island: Implications for Barrier Island Internal Architecture, Model for Growth of Progradational Microtidal Barrier Islands, and Gulf of Mexico Sea-Level Cyclicity: Journal of Sedimentary Research, v. 80, no. 4, p. 303-319.

Gelfenbaum, G., Stevens, A. W., Miller, I., Warrick, J. A., Ogston, A. S., and Eidam, E., 2015, Large-scale dam removal on the Elwha River, Washington, USA: Coastal geomorphic change: Geomorphology, v. 246, p. 649-668.

Giosan, L., Morphodynamic feedbacks on deltaic coasts: lessons from the wave-dominated Danube delta, *in* Proceedings Proceedings of coastal sediments2007, p. 828-841.

Glover, H., 2018, Wave, temperature, salinity, turbidity data collected on a benthic tripod near the mouth of the Elwha River, WA in 2015-2017.: Department of Oceanography Faculty Papers and Research.

Griggs, G. B., Patsch, K., and Savoy, L. E., 2005, Living with the changing California coast, Univ of California Press.

Grossinger, R., Stein, E. D., Cayce, K., Askevold, R., Dark, S., and Whipple, A., 2011, Historical Wetlands of the Southern California Coast: An Atlas of US Coast Survey T-sheets, 1851-1889, San Francisco Estuary Institute Oakland.

Hall, B., 2010, Holocene relative sea-level changes and ice fluctuations in the South Shetland Islands: Global and Planetary Change, v. 74, no. 1, p. 15-26.

Hall, B. L., 2009, Holocene glacial history of Antarctica and the sub-Antarctic islands: Quaternary Science Reviews, v. 28, no. 21-22, p. 2213-2230.

Hall, B. L., Henderson, G. M., Baroni, C., and Kellogg, T. B., 2010, Constant Holocene Southern-Ocean 14C reservoir ages and ice-shelf flow rates: Earth and Planetary Science Letters, v. 296, no. 1-2, p. 115-123.

Hapke, C. J., Reid, D., Richmond, B. M., Ruggiero, P., and List, J., 2006, National assessment of shoreline change Part 3: Historical shoreline change and associated coastal land loss along sandy shorelines of the California Coast: US Geological Survey Open File Report, v. 1219, p. 79.

Hayes, M. O., and Boothroyd, J. C., 1969, Storms as modifying agents in the coastal environment: Coastal Environments. NE Massachusetts, Department of Geology, University of Massachusetts, Amherst, p. 290-315.

Hein, C. J., FitzGerald, D. M., de Menezes, J. T., Cleary, W. J., Klein, A. H., and Albernaz, M. B., 2014, Coastal response to late-stage transgression and sea-level highstand: Geological Society of America Bulletin, v. 126, no. 3-4, p. 459-480.

Hendy, I. L., Dunn, L., Schimmelmann, A., and Pak, D., 2013, Resolving varve and radiocarbon chronology differences during the last 2000 years in the Santa Barbara Basin sedimentary record, California: Quaternary International, v. 310, p. 155-168.

Hine, A. C., 1979, Mechanisms of berm development and resulting beach growth along a barrier spit complex: Sedimentology, v. 26, no. 3, p. 333-351.

Hjort, C., Ingólfsson, Ó., Möller, P., and Lirio, J. M., 1997, Holocene glacial history and sea-level changes on James Ross Island, Antarctic Peninsula: Journal of Quaternary Science, v. 12, no. 4, p. 259-273.

Hodgson, D. A., Roberts, S. J., Smith, J. A., Verleyen, E., Sterken, M., Labarque, M., Sabbe, K., Vyverman, W., Allen, C. S., and Leng, M. J., 2013, Late Quaternary environmental changes in Marguerite Bay, Antarctic Peninsula, inferred from lake sediments and raised beaches: Quaternary Science Reviews, v. 68, p. 216-236.

Holland, K. T., 1998, Beach cusp formation and spacings at Duck, USA: Continental Shelf Research, v. 18, no. 10, p. 1081-1098.

Honke, J., Pigati, J., Wilson, J., Bright, J., Goldstein, H., Skipp, G., Reheis, M., and Havens, J., 2019, Late Quaternary paleohydrology of desert wetlands and pluvial lakes in the Soda Lake basin, central Mojave Desert, California (USA): Quaternary Science Reviews, v. 216, p. 89-106.

Hubbard, J., Shaw, J. H., Dolan, J., Pratt, T. L., McAuliffe, L., and Rockwell, T. K., 2014, Structure and seismic hazard of the Ventura Avenue anticline and Ventura fault, California: Prospect for large, multisegment ruptures in the western Transverse Ranges: Bulletin of the Seismological Society of America.

Ingram, B. L., and Southon, J. R., 1996, Reservoir ages in eastern Pacific coastal and estuarine waters: Radiocarbon, v. 38, no. 3, p. 573-582.

Inman, D. L., and Jenkins, S. A., 1999, Climate change and the episodicity of sediment flux of small California rivers: The Journal of geology, v. 107, no. 3, p. 251-270.

Jackson, J. A., 1997, swash bars, Glossary of Geology: Alexandria, Virginia, American Geological Institute, p. 643.

Jerolmack, D. J., and Swenson, J. B., 2007, Scaling relationships and evolution of distributary networks on wave-influenced deltas: Geophysical Research Letters, v. 34, no. 23.

Kaminuma, K., 1995, Seismicity around the Antarctic Peninsula: Proceedings of the NIPR Symposium on Antarctic Sciences, no. 8, p. 35-42.

Kirby, M., Lund, S., Patterson, W., Anderson, M., Bird, B., Ivanovici, L., Monarrez, P., and Nielsen, S., 2010, A Holocene record of Pacific decadal oscillation (PDO)-related hydrologic variability in southern California (Lake Elsinore, CA): Journal of Paleolimnology, v. 44, no. 3, p. 819-839.

Lambeck, K., Smither, C., and Johnston, P., 1998, Sea-level change, glacial rebound and mantle viscosity for northern Europe: Geophysical Journal International, v. 134, no. 1, p. 102-144.

Lindhorst, S., Betzler, C., and Hass, H. C., 2008, The sedimentary architecture of a Holocene barrier spit (Sylt, German Bight): Swash-bar accretion and storm erosion: Sedimentary Geology, v. 206, no. 1, p. 1-16.

Lindhorst, S., and Schutter, I., 2014, Polar gravel beach-ridge systems: Sedimentary architecture, genesis, and implications for climate reconstructions (South Shetland Islands/Western Antarctic Peninsula): Geomorphology, v. 221, p. 187-203.

Luyendyk, B. P., 1991, A model for Neogene crustal rotations, transtension, and transpression in southern California: Geological Society of America Bulletin, v. 103, no. 11, p. 1528-1536.

MacInnes, B. T., Bourgeois, J., Pinegina, T. K., and Kravchunovskaya, E. A., 2009, Tsunami geomorphology: Erosion and deposition from the 15 November 2006 Kuril Island tsunami: Geology, v. 37, no. 11, p. 995-998.

Magirl, C. S., Hilldale, R. C., Curran, C. A., Duda, J. J., Straub, T. D., Domanski, M., and Foreman, J. R., 2015, Large-scale dam removal on the Elwha River, Washington, USA: Fluvial sediment load: Geomorphology, v. 246, p. 669-686.

McAuliffe, L. J., Dolan, J. F., Rhodes, E. J., Hubbard, J., Shaw, J. H., and Pratt, T. L., 2015, Paleoseismologic evidence for large-magnitude (Mw 7.5–8.0) earthquakes on the Ventura blind thrust fault: Implications for multifault ruptures in the Transverse Ranges of southern California: Geosphere, v. 11, no. 5, p. 1629-1650.

Meilianda, E., Dohmen-Janssen, C. M., Maathuis, B. H. P., Hulscher, S. J. M. H., and Mulder, J. P. M., 2010, Short-term morphological responses and developments of Banda Aceh coast, Sumatra Island, Indonesia after the tsunami on 26 December 2004: Marine Geology, v. 275, no. 1, p. 96-109.

Meko, D. M., Woodhouse, C. A., and Bigio, E. R., 2017, University of Arizona Southern California Tree-Ring Study.

Montgomery, D. R., and Brandon, M. T., 2002, Topographic controls on erosion rates in tectonically active mountain ranges: Earth and Planetary Science Letters, v. 201, no. 3–4, p. 481-489.

Moore, L., Jol, H. M., Kruse, S., Vanderburgh, S., and Kaminsky, G., 2004, Annual layers revealed by GPR in the subsurface of a prograding coastal barrier, southwest Washington, USA: Journal of Sedimentary Research, v. 74, no. 5, p. 690-696.

Mosher, D. C., and Hewitt, A. T., 2004, Late Quaternary deglaciation and sea-level history of eastern Juan de Fuca Strait, Cascadia: Quaternary International, v. 121, no. 1, p. 23-39.

Mulvaney, R., Abram, N. J., Hindmarsh, R. C., Arrowsmith, C., Fleet, L., Triest, J., Sime, L. C., Alemany, O., and Foord, S., 2012, Recent Antarctic Peninsula warming relative to Holocene climate and ice-shelf history: Nature, v. 489, no. 7414, p. 141.

Murray, A. S., and Wintle, A. G., 2000, Luminescence dating of quartz using an improved single-aliquot regenerative-dose protocol: Radiation measurements, v. 32, no. 1, p. 57-73.

Nardin, W., and Fagherazzi, S., 2012, The effect of wind waves on the development of river mouth bars: Geophysical Research Letters, v. 39, no. 12.

Neal, A., 2004, Ground-penetrating radar and its use in sedimentology: principles, problems and progress: Earth-science reviews, v. 66, no. 3, p. 261-330.

Neal, A., Pontee, N. I., Pye, K., and Richards, J., 2002, Internal structure of mixed-sand-and-gravel beach deposits revealed using ground-penetrating radar: Sedimentology, v. 49, no. 4, p. 789-804.

Nicholson, C., Plesch, A., Sorlien, C. C., Shaw, J. H., and Hauksson, E., The SCEC Community Fault Model Version 5.0: An Updated And Expanded 3D Fault Set For Southern California, *in* Proceedings Pacific Section AAPG Convention2015.

Nield, G. A., Barletta, V. R., Bordoni, A., King, M. A., Whitehouse, P. L., Clarke, P. J., Domack, E., Scambos, T. A., and Berthier, E., 2014, Rapid bedrock uplift in the Antarctic Peninsula explained by viscoelastic response to recent ice unloading: Earth and Planetary Science Letters, v. 397, p. 32-41.

Nooren, K., Hoek, W. Z., Winkels, T., Huizinga, A., Van der Plicht, H., Van Dam, R. L., Van Heteren, S., Van Bergen, M. J., Prins, M. A., and Reimann, T., 2017, The Usumacinta–Grijalva beach-ridge plain in southern Mexico: a high-resolution archive of river discharge and precipitation: Earth Surface Dynamics, v. 5, no. 3, p. 529.

Nývlt, D., Braucher, R., Engel, Z., Mlčoch, B., and team, A., 2014, Timing of the Northern Prince Gustav Ice Stream retreat and the deglaciation of northern James Ross Island, Antarctic Peninsula during the last glacial–interglacial transition: Quaternary Research, v. 82, no. 2, p. 441-449.

O'Hirok, L. S., 1985, Barrier beach formation and breaching, Santa Clara River mouth, California: UCLA, Geography.

Oliver, T. S. N., Tamura, T., Hudson, J. P., and Woodroffe, C. D., 2017, Integrating millennial and interdecadal shoreline changes: Morpho-sedimentary investigation of two prograded barriers in southeastern Australia: Geomorphology, v. 288, p. 129-147.

Otvos, E. G., 2000, Beach ridges—definitions and significance: Geomorphology, v. 32, no. 1-2, p. 83-108.

Pedersen, J. B. T., Kroon, A., and Jakobsen, B. H., 2011, Holocene sea-level reconstruction in the Young Sound region, Northeast Greenland: Journal of Quaternary Science, v. 26, no. 2, p. 219-226.

Peltier, W., Argus, D., and Drummond, R., 2015, Space geodesy constrains ice age terminal deglaciation: The global ICE-6G_C (VM5a) model: Journal of Geophysical Research: Solid Earth, v. 120, no. 1, p. 450-487.

Plesch, A., Shaw, J. H., Benson, C., Bryant, W. A., Carena, S., Cooke, M., Dolan, J., Fuis, G., Gath, E., and Grant, L., 2007, Community fault model (CFM) for southern California: Bulletin of the Seismological Society of America, v. 97, no. 6, p. 1793-1802.

Preoteasa, L., Vespremeanu-Stroe, A., Tătui, F., Zăinescu, F., Timar-Gabor, A., and Cîrdan, I., 2016, The evolution of an asymmetric deltaic lobe (Sf. Gheorghe, Danube) in association with cyclic development of the river-mouth bar: Long-term pattern and present adaptations to human-induced sediment depletion: Geomorphology, v. 253, p. 59-73.

Psuty, N. P., 1965, Beach-ridge development in Tabasco, Mexico 1: Annals of the Association of American Geographers, v. 55, no. 1, p. 112-124.

Pudsey, C. J., and Evans, J., 2001, First survey of Antarctic sub–ice shelf sediments reveals mid-Holocene ice shelf retreat: Geology, v. 29, no. 9, p. 787-790.

Pudsey, C. J., Murray, J. W., Appleby, P., and Evans, J., 2006, Ice shelf history from petrographic and foraminiferal evidence, Northeast Antarctic Peninsula: Quaternary Science Reviews, v. 25, no. 17-18, p. 2357-2379.

Randle, T. J., Bountry, J. A., Ritchie, A., and Wille, K., 2015, Large-scale dam removal on the Elwha River, Washington, USA: Erosion of reservoir sediment: Geomorphology, v. 246, p. 709-728.

Reading, H. G., 2009, Sedimentary environments: processes, facies and stratigraphy, John Wiley & Sons.

Reimer, P. J., Bard, E., Bayliss, A., Beck, J. W., Blackwell, P. G., Ramsey, C. B., Buck, C. E., Cheng, H., Edwards, R. L., and Friedrich, M., 2013, IntCal13 and Marine13 radiocarbon age calibration curves 0–50,000 years cal BP: Radiocarbon, v. 55, no. 4, p. 1869-1887.

Reynolds, L. C., and Simms, A. R., 2015, Late Quaternary relative sea level in southern California and Monterey Bay: Quaternary Science Reviews, v. 126, p. 57-66.

Reynolds, L. C., Simms, A. R., Ejarque, A., King, B., Anderson, R. S., Carlin, J. A., Bentz, J. M., Rockwell, T. K., and Peters, R., 2018, Coastal flooding and the 1861-2 California storm season: Marine Geology, v. 400, p. 49-59.

Rignot, E., Casassa, G., Gogineni, P., Krabill, W., Rivera, A., and Thomas, R., 2004, Accelerated ice discharge from the Antarctic Peninsula following the collapse of Larsen B ice shelf: Geophysical Research Letters, v. 31, no. 18.

Ritchie, A., 2014, The Elwha PlaneCam: A novel and affordable aerial survey method tracking river and shoreline evolution in high spatiotemporal resolution during the largest dam removal in history, Salish Sea Ecosystem Conference.

Ritchie, A. C., Warrick, J. A., East, A. E., Magirl, C. S., Stevens, A. W., Bountry, J. A., Randle, T. J., Curran, C. A., Hilldale, R. C., and Duda, J. J., 2018, Morphodynamic evolution following sediment release from the world’s largest dam removal: Scientific reports, v. 8.

Roberts, S., Hodgson, D., Bentley, M., Sanderson, D., Milne, G., Smith, J., Verleyen, E., and Balbo, A., 2009, Holocene relative sea-level change and deglaciation on Alexander Island, Antarctic Peninsula, from elevated lake deltas: Geomorphology, v. 112, no. 1-2, p. 122-134.

Roberts, S. J., Hodgson, D. A., Sterken, M., Whitehouse, P. L., Verleyen, E., Vyverman, W., Sabbe, K., Balbo, A., Bentley, M. J., and Moreton, S. G., 2011, Geological constraints on glacio-isostatic adjustment models of relative sea-level change during deglaciation of Prince Gustav Channel, Antarctic Peninsula: Quaternary Science Reviews, v. 30, no. 25-26, p. 3603-3617.

Rockwell, T., Keller, E., and Dembroff, G., 1988, Quaternary rate of folding of the Ventura Avenue anticline, western Transverse Ranges, southern California: Geological Society of America Bulletin, v. 100, no. 6, p. 850-858.

Rockwell, T. K., Clark, K., Gamble, L., Oskin, M. E., Haaker, E. C., and Kennedy, G. L., 2016, Large Transverse Range earthquakes cause coastal upheaval near Ventura, southern California: Bulletin of the Seismological Society of America, v. 106, no. 6, p. 2706-2720.

Rodriguez, A., Hamilton, M., and Anderson, J., 2000, Facies and evolution of the modern Brazos Delta, Texas: wave versus flood influence: Journal of Sedimentary Research, v. 70, no. 2, p. 283-295.

Rodriguez, A. B., and Meyer, C. T., 2006, Sea-level variation during the Holocene deduced from the morphologic and stratigraphic evolution of Morgan Peninsula, Alabama, USA: Journal of Sedimentary Research, v. 76, no. 2, p. 257-269.

Ruggiero, P., Kaminsky, G. M., and Gelfenbaum, G., 2003, Linking proxy-based and datum-based shorelines on a high-energy coastline: implications for shoreline change analyses: Journal of Coastal Research, p. 57-82.

Ryan, K. J., Geist, E. L., Barall, M., and Oglesby, D. D., 2015, Dynamic models of an earthquake and tsunami offshore Ventura, California: Geophysical Research Letters.

Scambos, T. A., Bohlander, J., Shuman, C. u., and Skvarca, P., 2004, Glacier acceleration and thinning after ice shelf collapse in the Larsen B embayment, Antarctica: Geophysical Research Letters, v. 31, no. 18.

Scambos, T. A., Hulbe, C., Fahnestock, M., and Bohlander, J., 2000, The link between climate warming and break-up of ice shelves in the Antarctic Peninsula: Journal of Glaciology, v. 46, no. 154, p. 516-530.

Scheffers, A., Engel, M., Scheffers, S., Squire, P., and Kelletat, D., 2012, Beach ridge systems–archives for Holocene coastal events?: Progress in Physical Geography, v. 36, no. 1, p. 5-37.

Shalowitz, A. L., 1964, Shore and sea boundaries: with special reference to the interpretation and use of Coast and Geodetic Survey data, US Government Printing Office.

Simkins, L. M., Simms, A. R., and DeWitt, R., 2013, Relative sea-level history of Marguerite Bay, Antarctic Peninsula derived from optically stimulated luminescence-dated beach cobbles: Quaternary Science Reviews, v. 77, p. 141-155.

Simms, A. R., DeWitt, R., Zurbuchen, J., and Vaughan, P., 2017, Coastal erosion and recovery from a Cascadia subduction zone earthquake and tsunami: Marine Geology, v. 392, p. 30-40.

Simms, A. R., Ivins, E. R., DeWitt, R., Kouremenos, P., and Simkins, L. M., 2012, Timing of the most recent Neoglacial advance and retreat in the South Shetland Islands, Antarctic Peninsula: insights from raised beaches and Holocene uplift rates: Quaternary Science Reviews, v. 47, p. 41-55.

Simms, A. R., Whitehouse, P. L., Simkins, L. M., Nield, G., DeWitt, R., and Bentley, M. J., 2018, Late Holocene relative sea levels near Palmer Station, northern Antarctic Peninsula, strongly controlled by late Holocene ice-mass changes: Quaternary Science Reviews, v. 199, p. 49-59.

Sperazza, M., Moore, J. N., and Hendrix, M. S., 2004, High-resolution particle size analysis of naturally occurring very fine-grained sediment through laser diffractometry: Journal of Sedimentary Research, v. 74, no. 5, p. 736-743.

Stevens, A., Gelfenbaum, G. R., Warrick, J., Miller, I. M., and Weiner, H. M., 2016, Bathymetry, topography, and sediment grain-size data from the Elwha River delta, Washington, July 2016, U.S. Geological Survey data release: http://dx.doi.org/10.5066/F7GQ6VXX.

Stockdon, H. F., Holman, R. A., Howd, P. A., and Sallenger Jr, A. H., 2006, Empirical parameterization of setup, swash, and runup: Coastal engineering, v. 53, no. 7, p. 573-588.

Stuiver, M., Reimer, P. J., and Reimer, R. W., 2018, CALIB 7.1.

Switzer, A., Bristow, C., and Jones, B., 2006, Investigation of large-scale washover of a small barrier system on the southeast Australian coast using ground penetrating radar: Sedimentary Geology, v. 183, no. 1-2, p. 145-156.

Tamura, T., 2012, Beach ridges and prograded beach deposits as palaeoenvironment records: Earth-Science Reviews, v. 114, no. 3, p. 279-297.

Tamura, T., Murakami, F., Nanayama, F., Watanabe, K., and Saito, Y., 2008, Ground-penetrating radar profiles of Holocene raised-beach deposits in the Kujukuri strand plain, Pacific coast of eastern Japan: Marine Geology, v. 248, no. 1-2, p. 11-27.

Thomas, I. D., King, M. A., Bentley, M. J., Whitehouse, P. L., Penna, N. T., Williams, S. D., Riva, R. E., Lavallee, D. A., Clarke, P. J., and King, E. C., 2011, Widespread low rates of Antarctic glacial isostatic adjustment revealed by GPS observations: Geophysical Research Letters, v. 38, no. 22.

Trenberth, K. E., Dai, A., van der Schrier, G., Jones, P. D., Barichivich, J., Briffa, K. R., and Sheffield, J., 2013, Global warming and changes in drought: Nature Climate Change, v. 4, p. 17.

Van Heteren, S., Fitzgerald, D., McKinlay, P., and Buynevich, I., 1998, Radar facies of paraglacial barrier systems: coastal New England, USA: Sedimentology, v. 45, no. 1, p. 181-200.

van Heteren, S., Huntley, D. J., van de Plassche, O., and Lubberts, R. K., 2000, Optical dating of dune sand for the study of sea-level change: Geology, v. 28, no. 5, p. 411-414.

Vespremeanu-Stroe, A., Preoteasa, L., Zăinescu, F., Rotaru, S., Croitoru, L., and Timar-Gabor, A., 2016, Formation of Danube delta beach ridge plains and signatures in morphology: Quaternary International.

Wang, P., and Horwitz, M. H., 2007, Erosional and depositional characteristics of regional overwash deposits caused by multiple hurricanes: Sedimentology, v. 54, no. 3, p. 545-564.

Warrick, J., 2002, Short-term (1997–2000) and long-term (1928–2000) observations of river water and sediment discharge to the Santa Barbara Channel: California [Ph. D. thesis]: Santa Barbara, University of California.

Warrick, J. A., Bountry, J. A., East, A. E., Magirl, C. S., Randle, T. J., Gelfenbaum, G., Ritchie, A. C., Pess, G. R., Leung, V., and Duda, J. J., 2015, Large-scale dam removal on the Elwha River, Washington, USA: source-to-sink sediment budget and synthesis: Geomorphology, v. 246, p. 729-750.

Warrick, J. A., George, D. A., Gelfenbaum, G., Ruggiero, P., Kaminsky, G. M., and Beirne, M., 2009, Beach morphology and change along the mixed grain-size delta of the dammed Elwha River, Washington: Geomorphology, v. 111, no. 3, p. 136-148.

Warrick, J. A., and Mertes, L. A., 2009, Sediment yield from the tectonically active semiarid Western Transverse Ranges of California: Geological Society of America Bulletin, v. 121, no. 7-8, p. 1054-1070.

Warrick, J. A., and Milliman, J. D., 2003, Hyperpycnal sediment discharge from semiarid southern California rivers: Implications for coastal sediment budgets: Geology, v. 31, no. 9, p. 781-784.

Warrick, J. A., and Stevens, A. W., 2011, A buoyant plume adjacent to a headland—Observations of the Elwha River plume: Continental Shelf Research, v. 31, no. 2, p. 85-97.

Watcham, E., Bentley, M., Hodgson, D., Roberts, S. J., Fretwell, P., Lloyd, J., Larter, R., Whitehouse, P., Leng, M., and Monien, P., 2011, A new Holocene relative sea level curve for the South Shetland Islands, Antarctica: Quaternary Science Reviews, v. 30, no. 21, p. 3152-3170.

Webster, K. L., 2014, Sediment dispersal and accumulation in an insular sea: deltas of Puget Sound.

Winterer, E. L., and Durham, D. L., 1962, Geology of southeastern Ventura Basin, Los Angeles County, California, 2330-7102.

Wright, L., 1977, Sediment transport and deposition at river mouths: a synthesis: Geological Society of America Bulletin, v. 88, no. 6, p. 857-868.

Yeats, R. S., 1977, High rates of vertical crustal movement near Ventura, California: Science, v. 196, no. 4287, p. 295-298.

Appendix A. Supplementary Files

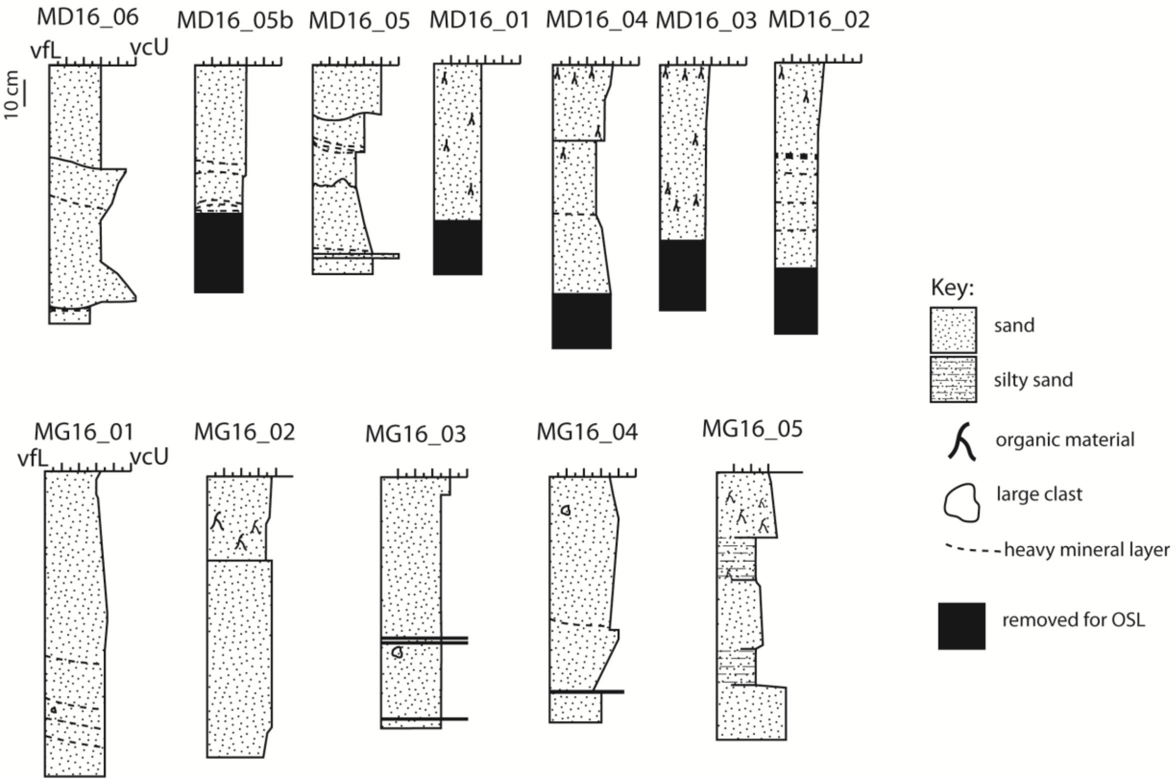

Figure 1. Core logs from Mandalay and McGrath State Beaches. Location shown in Figure 15.

Table 1. Measurement steps for the single-aliquot regenerative protocol.

Step	Procedure (quartz)
1	Regeneration[1]/natural dose
2	Preheat (160 °C), hold for 10 seconds
3	OSL stimulation with blue LEDs at 100 °C for 40 seconds (L_x)
4	Test dose beta irradiation (1.4 Gy)
5	Cut heat (160 °C) for 0 seconds
6	OSL stimulation with blue LEDs at 100 °C for 40 seconds (T_x)
7	Repeat Steps 1–6 with further regeneration doses

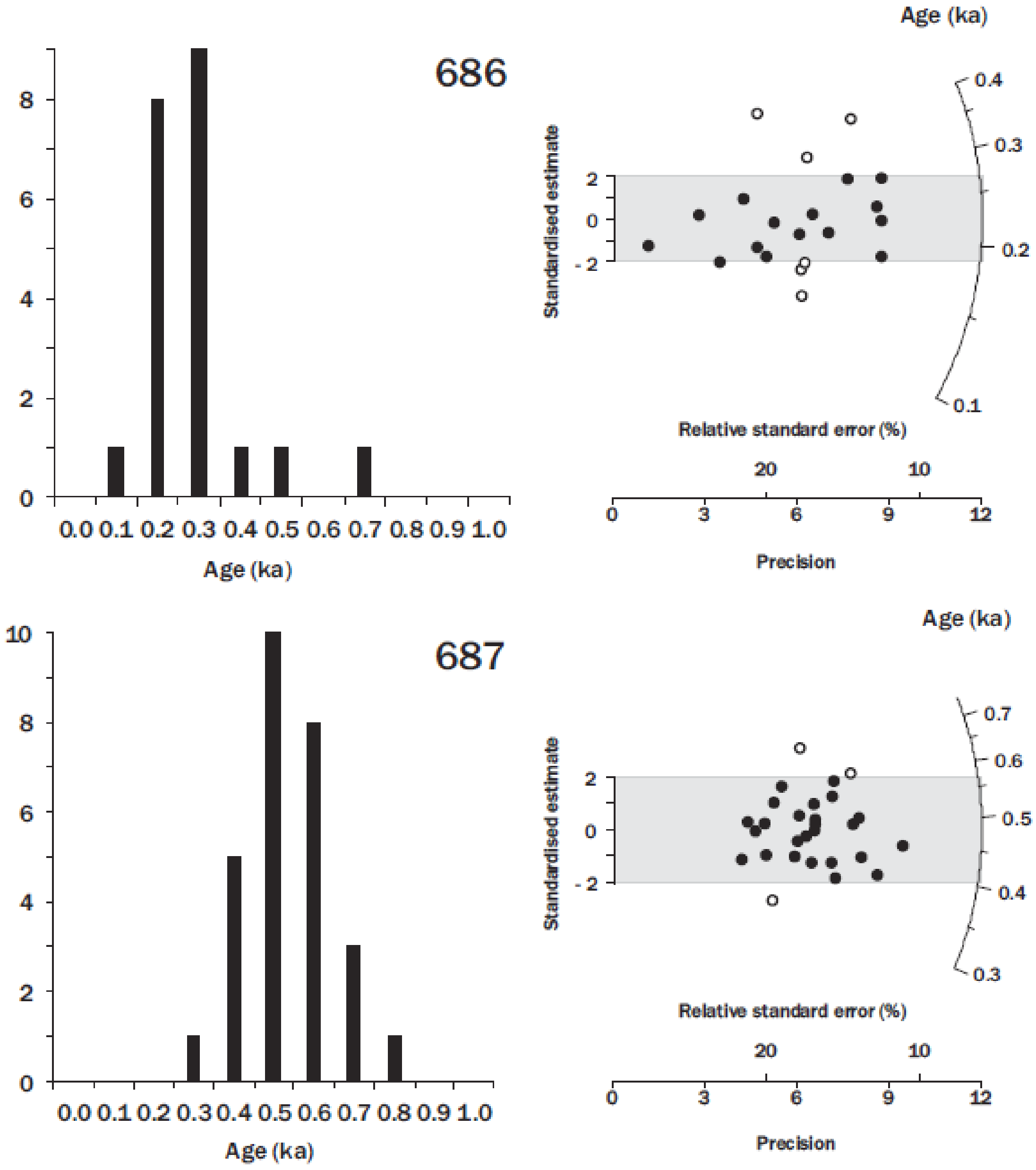

Figure 2. Age distributions, as a histogram and a radial plot, for all samples 686 is MD16_02, and 687 is MD16_05b. Each circle on the radial plot represents the age and uncertainty, for a single aliquot. The age is read on the arc axis, by drawing a straight line from (0,0), passing through a circle and intersecting the radial axis (log scale). The (0,0) coordinate corresponds to a 0 standardized estimate (y-axis) and 0 precision (x-axis). The uncertainty is read on the horizontal axis, by drawing a perpendicular line reaching a circle. Hence, two aliquots, having the same age, but with different uncertainty, will lay on the same straight line (from (0,0) to the radial axis). The aliquot with the smaller uncertainty (higher precision) will be closer to the arc. Values (filled circles) within the light grey shaded band are consistent (at 2_) with the weighted mean (Central Age Model). A cluster of aliquots within this shaded band expresses confidence that we have a population of grains consistent with a single age.